

Magnetic interactions between transition
metal impurities and clusters mediated
by low-dimensional metallic hosts:
A first principles theoretical investigation

VON

Lucila Maitreya Juárez Reyes

Dissertation

zur Erlangung des akademischen Grades eines
Doktors der Naturwissenschaften
(*Dr. rer. nat.*)

vorgelegt dem
Fachbereich Mathematik und Naturwissenschaften der
Universität Kassel



Betreuer:

Prof. Dr. Gustavo M. Pastor

Verteidigt am 5. Februar 2015

Magnetic interactions between transition
metal impurities and clusters mediated
by low-dimensional metallic hosts:
A first principles theoretical investigation

by

Lucila Maitreya Juárez Reyes

Dissertation

for the attainment of the academic grade

Doktor der Naturwissenschaften

(Dr. rer. nat.)

submitted to

Department of Mathematics and Natural Sciences

Kassel University



Supervisor:

Prof. Dr. Gustavo M. Pastor

Defended on 5. Februar 2015

*“A craftsman pulled a reed from the reedbed,
cut holes in it, and called it a human being.
Since then, it’s been wailing a tender agony of parting,
never mentioning the skill that gave it life as a flute”*

Rumi

Erklärung

Hiermit versichere ich, dass ich die vorliegende Dissertation selbstständig, ohne unerlaubte Hilfe Dritter angefertigt und andere als die in der Dissertation angegebenen Hilfsmittel nicht benutzt habe. Alle Stellen, die wörtlich oder sinngemäß aus veröffentlichten oder unveröffentlichten Schriften entnommen sind, habe ich als solche kenntlich gemacht. Dritte waren an der inhaltlich-materiellen Erstellung der Dissertation nicht beteiligt; insbesondere habe ich hierfür nicht die Hilfe eines Promotionsberaters in Anspruch genommen. Kein Teil dieser Arbeit ist in einem anderen Promotions- oder Habilitationsverfahren verwendet worden.

Kassel, Februar 2015

Lucila Juárez

Acknowledgements

I would like to acknowledge Prof. Dr. Gustavo Pastor for guiding, supervising and correcting this work.

I sincerely thank Prof. Dr. Valeri Stepanyuk for his meaningful advices and contribution to this research. For their unconditional and friendly support I thank to my colleagues in Kassel and Halle: M. Saubenère, P. Ruíz, L. Díaz and O. Brovko.

I acknowledge the ITS center and the *Max Planck Institut für Nanostruktur Physik* for the computational resources and the Deutsche Akademische Austausch Dienst (DAAD) for financial support.

Finally, I would like to express my personal thanks to my friends Tanveer, Martin, Liset, Christian and Joseph. My deepest gratefulness to my family, and above all, to my parents, for whom I can not find words grand enough to say thanks.

Kassel, September 2014.

Abstract

The magnetic properties and interactions between transition metal (TM) impurities and clusters in low-dimensional metallic hosts are studied using a first principles theoretical method. In the first part of this work, the effect of magnetic order in $3d$ - $5d$ systems is addressed from the perspective of its influence on the enhancement magnetic anisotropy energy (MAE). In the second part, the possibility of using external electric fields (EFs) to control the magnetic properties and interactions between nanoparticles deposited at noble metal surfaces is investigated.

The influence of $3d$ composition and magnetic order on the spin polarization of the substrate and its consequences on the MAE are analyzed for the case of $3d$ impurities in one- and two-dimensional polarizable hosts. It is shown that the MAE and easy-axis of monoatomic free standing $3d$ -Pt wires is mainly determined by the atomic spin-orbit (SO) coupling contributions. The largest MAEs are thus obtained when the Pt and $3d$ contributions favor the same easy-axis, which generally corresponds to the direction yielding to the largest local spin and orbital moments of Pt. In FePt wires, an antiferromagnetic alignment between the Fe moments in which the Pt atoms adopt a non magnetic state is energetically favored. The competition between ferromagnetic (FM) and antiferromagnetic (AF) order in FePt $_n$ wires is studied in detail for $n = 1 - 4$ as a function of the relative position and magnetic coupling between Fe atoms. For FePt $_n$ wires $n \geq 2$, our results show an oscillatory behavior of the magnetic polarization of Pt atoms as a function of their distance from the magnetic impurities, which can be correlated to a long-ranged magnetic coupling of the Fe atoms. Exceptionally large variations of the induced spin and orbital moments at the Pt atoms are found as a function of concentration and magnetic order. Along with a violation of the third Hund's rule at the Fe sites, these variations result in a non trivial behavior of the MAE.

In the case of TM impurities and dimers at the Cu(111), the effects of surface charging and applied EFs on the magnetic properties and substrate-mediated magnetic interactions have been investigated. The modifications of the surface electronic structure, impurity local moments and magnetic exchange coupling as a result of the EF-induced metallic screening and charge rearrangements are analyzed. In a first study, the properties of surface substitutional Co and Fe impurities are investigated as a function of the external charge per surface atom q . At inter-impurity distances $r > 10 \text{ \AA}$ the effective magnetic exchange coupling ΔE between impurities shows RKKY-like oscillations as a function of the distance which are not significantly affected by the considered values of q . For distances $r < 10 \text{ \AA}$, important modifications in the magnitude of ΔE ,

involving changes from FM to AF coupling, are found depending non-monotonously on the value and polarity of q . The interaction energies are analyzed from a local perspective.

In a second study, the interplay between external EF effects, internal magnetic order and substrate-mediated magnetic coupling has been investigated for Mn dimers on Cu(111). Our calculations show that a fairly strong EF ($\sim 1\text{eV}/\text{\AA}$) can induce a switching from AF to FM ground-state magnetic order within single Mn dimers. The relative coupling between a pair of dimers also shows RKKY-like oscillations as a function of the inter-dimer distance. Their effective magnetic exchange interaction is found to depend significantly on the magnetic order within the Mn dimers and on their relative orientation on the surface. The dependence of the substrate-mediated interaction on the magnetic state of the dimers is qualitatively explained in terms of the differences in the scattering of surface electrons. Moreover, an outgoing (incoming) orientation of the applied EF with respect to the surface favors the parallel (antiparallel) coupling between dimers. At short inter-dimer distances ($r < 10 \text{ \AA}$), the ground-state configuration is determined by an interplay between exchange interactions and EF effects. These results demonstrate that external surface charging and applied EFs offer remarkable possibilities of manipulating the sign and strength of the magnetic coupling of surface supported nanoparticles.

Deutsche Übersetzung

Titel:

Magnetische Wechselwirkungen zwischen
Übergangsmetall-Verunreinigungen und -Clusters vermittelt durch
niedrig-dimensionale metallische Substrate: Eine theoretische
first-principles Untersuchung

Zusammenfassung

Die magnetischen Eigenschaften und Wechselwirkungen zwischen Übergangsmetall-(TM) Verunreinigungen und Clustern werden in niedrigdimensionalen Wirtsmetallen theoretisch unter Verwendung einer 'first principles' Methode erforscht. Der erste Teil dieser Doktorarbeit befasst sich mit der Frage nach dem temperaturinduzierten superparamagnetischen Verhalten aus der Perspektive einer erhöhten magnetischen Anisotropieenergie (MAE). Der zweite Teil widmet sich dem Einfluss durch externe elektrische Felder (EFer) und der Kontrolle der magnetischen Eigenschaften und Wechselwirkungen zwischen Nanoteilchen deponiert auf Edelmetalloberflächen. Analysiert wird der Einfluss von verschiedenen 3d-TM und der magnetischen Ordnung auf die Spinpolarisierung des Substrats und die einhergehenden Konsequenzen für die MAE für den Fall von 3d-Verunreinigungen in besonders stark polarisierbaren Wirtsmetallen. Nachweislich wird die MAE und die leichte Achse von monoatomaren, freistehenden 3d-Pt Ketten hauptsächlich bestimmt durch die atomaren Spin-Bahn (SB) Kopplungsbeiträge. Die höchsten MAEs können erreicht werden, wenn sowohl die Pt- als auch die 3d- Beiträge dieselbe leichte Achse bevorzugen. Im allgemeinen entspricht diese der Richtung, die zu den stärksten lokalen Spin- und Bahnmomenten der Pt-Atome führt. In FePt-Ketten wird eine antiferromagnetische Anordnung zwischen den Fe-Momenten begünstigt, während die Pt-Atome einen nichtmagnetischen Zustand annehmen. Sorgfältig untersucht werden die miteinander konkurrierende ferromagnetische (FM) und antiferromagnetische (AF) Kopplung in FePt_n für $n = 1 - 4$ als Funktion der relativen Position und der magnetischen Kopplung zwischen den Fe-Atomen. Für FePt_n-Ketten mit $n \geq 2$ zeigen unsere Berechnungen ein oszillatorisches Verhalten der magnetischen Polarisierung der Pt-Atome als Funktion ihres Abstands zu den magnetischen Verunreinigungen und kann mit einer langreichweitigen magnetischen Kopplung zwischen den Fe-Atomen korreliert werden. Aussergewöhnlich hohe Schwankungen der induzierten Spin- und Bahnmomente an den Pt-Atomen

konnten als Funktion der Konzentration und der magnetischen Ordnung gefunden werden. Einhergehend mit einer Verletzung der 3. Hundtschen Regel am Ort der Fe-Verunreinigung resultieren diese Schwankungen in einem nichttrivialen Verhalten der MAE.

Im Fall der TM-Verunreinigungen und Dimere auf Cu(111) wurde die Wirkung der Oberflächenladung und angelegter EFer auf die magnetischen Eigenschaften und substratvermittelten magnetischen Wechselwirkungen hin untersucht. Analysiert wurden die Modifikationen der elektronischen Struktur an Oberflächen, lokalen Verunreinigungsmomente und die magnetische Austauschkopplung als Folge der EF-induzierten metallischen Abschirmung und Ladungs-Umverteilung. In einer ersten Studie werden die Eigenschaften von Co- und Fe-Verunreinigungen als Funktion der externen Ladung q pro Oberflächenatom untersucht. Bei einem interatomaren Abstand $r > 10\text{\AA}$ zwischen zwei Verunreinigungen zeigt die effektive magnetische Austauschkopplung ΔE zwischen den Verunreinigungen eine RKKY-ähnliche Oszillation als Funktion des Abstands, der nur gering beeinflusst wird von den betrachteten Werten von q . Für Abstände $r < 10\text{\AA}$ wurden bedeutende Modifikationen in der Grösse von ΔE beobachtet. Diese führen zu einer Änderung der FM- hin zur AF-Kopplung in nichtmonotoner Abhängigkeit von dem Wert und der Polarität von q . Die Wechselwirkungsenergien werden aus einer lokalen Perspektive analysiert.

In einer weiteren Studie werden das Wechselspiel zwischen äusseren EF-Effekten, der internen magnetischen Ordnung und substratvermittelten magnetischen Kopplung für Mn-Dimere auf Cu(111) untersucht. Unsere Berechnungen zeigen, dass ausreichend starke EF ($\sim 1\text{eV}/\text{\AA}$) ein Umklappen der magnetischen Ordnung im Grundzustand von AF nach FM innerhalb einzelner Mn-Dimere induzieren können. Die jeweilige Kopplung zwischen einem Paar von Dimeren zeigt ebenfalls RKKY-ähnliche Oszillationen als Funktion des inter-dimeren Abstands. Es konnte festgestellt werden, dass die effektive magnetische Austauschwechselwirkung signifikant von der magnetischen Ordnung innerhalb der Mn-Dimere und von ihrer relativen Orientierung auf der Oberfläche abhängt. Die Abhängigkeit von den substratvermittelten Wechselwirkungen von dem magnetischen Zustand des Dimers wird qualitativ erklärt mit der unterschiedlichen Streuung von Oberflächenelektronen. Darüberhinaus führt eine unterschiedliche Orientierung des angelegten EFs, senkrecht zur Oberfläche, zu einer parallelen oder antiparallelen Kopplung zwischen den Dimeren. Bei kurzen interdimeren Abständen ($r < 10\text{\AA}$) wird die Grundzustandskonfiguration bestimmt von dem Wechselspiel zwischen der Austauschwechselwirkung und EF-Effekten. Diese Studie beweist, dass externe Oberflächenladungen und angelegte EFer bemerkenswerte

Möglichkeiten der Manipulation des Vorzeichens und der Stärke der magnetischen Kopplung von Nanopartikeln besitzen, die auf Oberflächen angelagert sind.

Contents

	Page
1 Introduction	1
2 Theoretical background	11
2.1 The quantum many-particle problem	12
2.1.1 The Born-Oppenheimer approximation	13
2.1.2 Hartree-Fock approximation	14
2.2 Density functional theory	15
2.2.1 The Hohenberg-Kohn theorems	15
2.2.2 The Kohn-Sham equations	18
2.2.3 Exchange-correlation functionals	21
2.3 Bloch's theorem and plane waves	23
2.4 Coupling between localized magnetic moments	25
2.4.1 The RKKY interaction	25

2.4.2	Noncollinear formulation	27
2.5	The spin-orbit coupling	28
2.6	The Hellmann-Feynman theorem	29
3	Computational methods	31
3.1	The Vienna ab-initio simulation package	31
3.1.1	Projector augmented waves	33
3.2	Green's function Korringa-Kohn-Rostoker method	34
3.2.1	Green's function formulation	35
3.2.2	The Dyson equation and the Lloyd's formula	36
4	TM impurities in highly polarizable hosts	41
4.1	Magnetic order and anisotropy of $3d$ -Pt _{<i>n</i>} wires	42
4.1.1	Computational details	44
4.1.2	Magnetic order and MAE of $3d$ -Pt wires	45
4.1.3	Magnetic order and anisotropy of FePt _{<i>n</i>} wires	48
4.2	Co adatoms on Pt(111)	62
4.2.1	Computational details	63
4.2.2	Local properties	65
5	Tuning substrate-mediated exchange interactions by surface charging	69
5.1	Computational details	72
5.2	Results	73
5.2.1	Clean surface	73
5.2.2	Single impurity	75
5.2.3	Magnetic exchange interactions	78

5.3	Conclusions	88
6	EF-modulated exchange coupling of magnetic clusters	91
6.1	Computational details	93
6.2	Results	95
6.2.1	The clean Cu(111) surface	95
6.2.2	Isolated Mn ₂ on Cu(111)	96
6.2.3	Magnetic state and coupling between dimers at short distances .	99
6.2.4	Long range substrate-mediated magnetic interactions	103
6.2.5	Structural relaxation effects	105
6.3	Conclusions	108
7	Summary and outlook	111
	List of Figures	115
	List of Tables	118

CHAPTER 1

Introduction

Magnetic interactions are responsible for the coupling between localized magnetic moments and the emergence of collective magnetic ordered states such as ferromagnetic (FM) and antiferromagnetic (AF) phases, or even complex non-collinear arrangements. These interactions can have different origins and ranges. For example, the classical electromagnetic interaction between dipoles dominates the coupling among particles displaying large moments μ , typically $\mu \gtrsim 10^3 \mu_B$. At the microscopic level, magnetic exchange interactions are the source of coupling between spin magnetic moments. Typical examples of such interactions are:

- The direct exchange interaction between atomic moments, caused by the overlapping of the atomic orbitals. Having strengths in the order of tens of eVs, direct exchange interactions dominate the magnetic coupling at very short interatomic distances, as for example, between nearest neighbor (NN) atoms in a crystal lattice.
- The super-exchange and double-exchange interactions between second NN atomic moments, mediated by an intermediate non-magnetic atom. Potentially competing with the direct exchange mechanism, these interactions usually promote the antiparallel spin alignment between two next-NN transition metal (TM)

atoms as a result of electron transfer via the orbital bonding with the common nonmagnetic adjacent atom.

- The Ruderman-Kittel-Kasuya-Yosida (RKKY) exchange interaction between localized magnetic moments in a non-magnetic metallic host. With interaction energies in the range of a few meVs, RKKY drives an oscillatory magnetic coupling mediated by the conduction electrons of the metal up to relatively large distances (i.e. $r > 10\text{\AA}$).

Exchange interactions take their name from their close relation with the exchange symmetry of indistinguishable particles, which precludes two electrons from being found in the same quantum state. Within an atom, the resulting *Pauli* exclusion principle prevents the atomic orbitals to be occupied by electrons having parallel spins. This restriction is, in fact, the origin of the formation of atomic spin moments.

In bulk materials, magnetism is strongly dependent on the electronic band-structure. In a mean-field approximation, the emergence of ferromagnetism in bulk transition metals (TMs) is given by the Stoner criterion

$$I \cdot D(\varepsilon_F) > 1,$$

where I is the so-called intra-atomic exchange integral and $D(\varepsilon_F)$ is the electronic density of states (DOS) at the Fermi energy (ε_F) [1], with the later scaling inversely proportional to the electronic bandwidth. For nanoscaled systems, where rather than forming bands the electronic levels are roughly discrete, the Stoner criterion can be applied using the local instead of the total DOS [2]. In this case, the (local) DOS scales approximately as $1/\sqrt{Z}$ with Z being the number of nearest neighbors. Consequently, a high incidence of spontaneous magnetic order is observed in low-coordinated atomic environments such as surfaces, nanoparticles, molecules and clusters. In fact, ferromagnetic behavior is often found in dimensionally reduced systems of paramagnetic materials which almost satisfy the Stoner criterion in the bulk phase (e.g., Pd, Pt and Rh). Magnetism at the nanoscale is, nevertheless, subtly dependent on the precise local environment.

The intricate behavior of magnetism at low dimensions offers a great variety of possibilities for technological application in nanoscaled devices. One in particular is the development of miniaturized magnetic recording media, where transition metal nanostructures can find application as data storage units. The largely enhanced magnetization values found in a wide diversity of pure as well as alloyed TM clusters has placed them as most promising candidates for recording purposes which deserve

special attention [2–7]. During the last decades, the fabrication and characterization of TM nanoparticles and clusters has been subject of intensive research. Still, the realistic realization of memory devices based on magnetic nanostructures faces important difficulties [3, 8]. A major problematic arises, for instance, in the frame of a supporting medium for the eventual assemble of ordered arrays of magnetic units (e.g., atoms, molecules, clusters or nanostructures) [3]. In this context, surface supported nanostructures, either disposed on top or embedded in the topmost surface atomic layer of nonmagnetic substrates, are systems of special interest.

Moreover, modern experimental techniques have recently made possible the fabrication and manipulation of surface nanostructures with atomic-scaled precision [9–12]. By means of a spin-resolved scanning tunneling microscope (STM) it is now possible to measure and control the spin direction of single atoms on metallic surfaces allowing the engineering and tailoring of nanomagnets [11, 13–16]. In fact, the possibility of representing and performing basic logic operations based on atomic spins has been recently demonstrated experimentally [17].

The physics of supported nanostructures can be, however, considerably influenced by their interaction with the substrate. For nanoparticles at surfaces, the local changes resulting from the binding with the substrate and the associated structural relaxations dominate the modification of their isolated-particle properties [3, 18]. Indeed, the contact with the substrate affects the local symmetry of the deposited particles (adparticles). In this sense, surface deposition can give rise to strongly anisotropic behavior even in single adsorbed atoms, or non-collinear magnetic order in larger nanostructures [3, 19–23].

In a similar way, the presence of adparticles has an effect on the supporting substrate. Adsorbates break the translational symmetry of a surface and its interaction with it can drive a diversity of phenomena. The interplay between adparticles and surface can give rise, for example, to surface alloying, Kondo effect, or substrate-mediated adparticles self-assembly [8, 12, 24–28]. Among the effects involving the surface, substrate-mediated interactions deserve special attention, not only for their potential applications in nano-scaled technologies but also from a fundamental perspective. Nowadays, it is well known that electronic surface states are responsible of mediating the Ruderman-Kittel-Kasuya-Yosida (RKKY) interaction [29–31] among deposited particles at metallic surfaces [27, 32–34]. Indirect RKKY interactions have been reported between adsorbed atoms (adatoms) and small adparticles at relatively large distances ($r > 10 \text{ \AA}$) on a variety of surfaces. In particular, the surface-state

electrons at the closed-packed surfaces of noble metals (e.g., Cu, Ag, Au) behave as a nearly-free two-dimensional (2D) electron gas [35]. In the presence of a surface defect (e.g., an adparticle) these electrons are scattered giving rise to Friedel oscillations of electronic density around the impurity [36]. As a result, an oscillating attractive-repulsive potential is induced, which favors particular spacings among neighboring defects. Diffusing atoms can, in this sense, experience the potential landscape created by neighboring adatoms and tend to occupy positions where their interaction energy is minimal. At low temperatures, this oscillatory interaction can drive the self-assembly of surface adparticles and eventually lead to the formation of periodic assemblies (superlattices), low-dimensional structures or simply affect the growth process of supported nanostructures on metal surfaces [26, 27, 37–40].

Substrate mediated interactions gained a lot of attention after the discovery of the giant magnetoresistance (GMR) effect in TM layers separated by nonmagnetic metallic spacers to which they are closely related. Namely, both effects share the underlying mechanism causing the oscillatory exchange coupling between magnetic layers, which is distinctive of GMR [41, 42]. This coupling originates from the spin-dependence on the scattering of (non-polarized) conduction electrons within the metal spacer as a consequence of the magnetic polarization of the TM layers. More specifically, the spin-polarized potential causes a difference in the scattering of electrons of majority- and minority- spin character which affects the relative distribution of their respective electronic densities between the two magnetic layers. As a result, the coupling between the TM layers is determined by the distance between them. Thus, control over the magnetic configuration can be achieved by adjusting the thickness of the metallic spacer. Such exchange mechanism should be expected to hold among other TM nanostructures inasmuch as they are coupled through a conduction electron band [42]. Indeed, the RKKY exchange interaction is known to cause the spatially oscillating magnetic coupling among localized spin moments in dilute alloys. These can be, for instance, TM impurities in a nonmagnetic host or magnetic defects deposited on metallic surfaces. Similarly to the case of GMR, this process can be interpreted in terms of the scattering of conduction electrons, regarded as incoming plane-waves, between two localized impurity potentials that spin-polarize the outgoing partial waves [43]. More precisely, the indirect magnetic coupling arises from the perturbative exchange between the localized d electrons of the magnetic defect and the delocalized s -band of the metallic host.

An estimate of the RKKY interaction energy can be evaluated from the one-electron contributions to the second-order of perturbation expansion of the impurity

potential. For large adsorbate separations (i.e. the asymptotic region $r > \pi/k_F$) the exchange energy between a pair of localized spin moments coupled through the 2D surface band of a metallic surface has the general form

$$J_{ij}(r_{ij}) \propto \frac{\cos(2k_F r_{ij}) + \delta}{(2k_F r_{ij})^2},$$

where the proportionality constant is specific to the impurity-substrate system, r_{ij} is the distance between impurities and k_F the Fermi wavevector of the host [29, 44]. Thus, the RKKY exchange interaction is characterized by an oscillatory magnetic coupling of period $\lambda_F/2$ with λ_F being the Fermi wavelength of the substrate. This long-ranged coupling is particularly relevant between adatoms and small clusters. It is expected to be largely cancelled out at relatively small particle sizes [45, 46] and to vanish for particles larger than the oscillation period ($\lambda_F/2$).

The standing waves of electronic density caused by the quantum interference of surface electrons traveling towards a defect and those which are back-scattered from it can be directly observed using STM [33, 36]. Furthermore, using spin-resolved STM, recent experiments have demonstrated the possibility of measuring exchange interactions on single TM adatoms [47, 48].

As well as self-assemble, indirect exchange interactions can influence the collective magnetic behavior of ensembles of supported TM nanoparticles. Frustration and randomness of competing microscopic interactions (e.g., dipolar, RKKY) can give rise to complex magnetic phases, besides the paramagnetic (disordered) state, such as low-temperature spontaneous magnetization and spin-glass behavior in disordered ensembles of magnetic nanoparticles [46, 49, 50]. Substrate-mediated indirect interactions have the potential to induce collective magnetic ordered states as, for example, the stabilization of finite temperature ferromagnetism predicted theoretically for ensembles of Fe nanoclusters on Cu(111) [46]. In this sense, the possibility of tailoring indirect exchange interactions would represent an important step towards the realization of nano-scaled technologies based on supported magnetic nanostructures. In particular, control over these interactions would be useful for both, preventing paramagnetic relaxation and inducing collective ordered magnetic states in supported nanoparticle arrays.

Another major concern regarding the possible use of magnetic nanoparticles as the constituent magnetic units of memory devices arises from their reduced size. In pure TM nanostructures, the total magnetization decreases monotonously with the

size of the particle. The choice of components developing large magnetization-volume ratios is, however, limited by a thermal aspect. At finite temperatures, the thermal energy can be sufficient to induce a reversal of the magnetic orientation of the adparticles, which would eventually lead to paramagnetic behavior in supported nanoparticle assemblies. At a given temperature T below the Curie temperature, the timescale of paramagnetic relaxation of a particle of volume V follows the proportionality relation

$$\tau \propto \exp\left(\frac{KV}{k_B T}\right)$$

where k_B is the Boltzmann constant and K is the magnetic anisotropy constant [51–53]. Hence, the element specific anisotropy constant K plays a key role in the magnetic order and orientation of the ensemble.

Nanostructures consisting of pure $3d$ -TMs are known to develop significant magnetization values as a result of exceptionally large spin and orbital magnetic moments [3, 54, 55]. However, due to their weak anisotropy constant, the stability of the magnetic orientation of these particles against external fields and temperature induced fluctuations is rather low. Thus, their application for most technological purposes is limited.

The differences in the properties of a system which depend on the orientation of its magnetization respect to the underlying crystal structure are called magnetic anisotropy (MA). MA has its origin in relativistic effects. The essential quantity concerning the orientation and stability of the magnetization is the magnetic anisotropy energy (MAE), which accounts for the energy required to rotate the magnetization of the system between two nonequivalent directions: a low-energy axis (easy axis) and a high-energy axis (hard axis). To a large extent, the MAE is the result of of the intra-atomic spin-orbit coupling (SOC). The SOC causes the spin moment to align along a particular direction respect to the crystal structure. The interaction energy is reasonably well described by the expression

$$H_{SO} = \lambda \mathbf{L} \cdot \mathbf{S}$$

where \mathbf{S} and \mathbf{L} stand for the spin and orbital moment operators, and λ is an element dependent coupling constant. In a semiclassical picture, the magnitude of the spin moments can be regarded as independent of its orientation and the MAE is, consequently, dominated by the anisotropy of the orbital moments.

For $3d$ transition metals the spin-orbit coupling constant is rather small. This relativistic effect becomes significant for heavier TM atoms (e.g., $4d$, $5d$). However, these

elements are generally non-magnetic in the bulk phase or display considerably small spin magnetic moments. Nevertheless, in the presence of spin polarization, the larger SO interaction energy promotes the development of important orbital moments and magnetic anisotropy energies. In fact, a substantial magnetic polarization is induced in several $4d$ and $5d$ elements due to the neighborhood of strongly ferromagnetic atoms as Fe or Co yielding to considerably enhanced values of the magnetization. Thereupon, $3d$ - $4d$ and $3d$ - $5d$ alloying has been proposed several times as a promising way to enhance the stability of the magnetic orientation of pure $3d$ -TM systems [3, 56, 57]. In this context, CoPt and FePt alloys are well known representative compounds developing remarkably large MAEs [4, 28, 56, 58].

Furthermore, the potential advantages of alloying can be achieved in supported nanoparticles by taking advantage of the depositon substrate. For example, $3d$ ferromagnetic elements as Fe and Co on Pt or Pd surfaces are known to induce the spin polarization of a large amount of neighboring substrate atoms. This effect has a strong influence on the magnetic properties and anisotropy of these systems [19, 20, 28, 59–61]. In fact, giant moments and anisotropies have been calculated and experimentally measured on individual Fe and Co atoms and small clusters at Pt and Pd surfaces [20, 61]. For instance, a single Co atom on Pt(111) has been found to develop a MAE of about 9.3 meV [20]. In larger $3d$ structures, however, the competition between FM and AF exchange couplings can cause the formation of complex magnetic phases with drastic consequences on the behavior of the MAE as a function of the surface coverage [62].

In general, low-dimensional systems display enhanced and complex magnetic anisotropic behavior [2, 3, 5, 7, 21, 62, 68, 69]. In this context, orbital moments can have an important contribution to the total magnetization [3, 19, 62]. These local orbital moments decrease by increasing atomic coordination and are rapidly quenched for an increasing size of the particles.

Moreover, small differences in the local environment can cause large variations of the magnetic response [5, 63]. Particularly in the case of nanostructures, symmetry and dimensionality are determinant for the magnetic properties [64]. For instance, in the case of one-dimensional TM structures, the interaction with the substrate, modifications in the lattice constant, chemical order or composition can be sufficient to change the overall magnetic state [65–69]. From this perspective, it is of great interest to analyze the influence of the magnetic coupling between $3d$ elements on the easy axis of magnetization and MAE of $3d$ - $5d$ systems.

As noticed from this overview, magnetic coupling, and hence, magnetic exchange interactions, are central to the problem of magnetism. Their interplay with other physical properties is an interesting problem of fundamental perspective with a great scope for technological applications. In particular, nanosystems composed by exchange-coupled magnetic units have an enormous potential of applicability in spintronics [16, 17]. A crucial step towards the realization of nano-scaled magneto-electronic technologies would be the ability of manipulate and control relevant intrinsic magnetic properties such as magnetization, magnetic anisotropy energy and, in particular, short and long ranged magnetic order. Exchange interactions certainly play a fundamental role in this problem.

An insight on the details of microscopic exchange mechanisms and its relation with other properties of interest is necessary for further understanding and for the development of methods to achieve its manipulation. In the context of supported nanostructure arrays, a major concern regards to the question: Can the collective properties and magnetic behavior of nanoparticle ensembles, and in particular the long-ranged magnetic order, be tailored by varying the composition, inter-particle distance, surface coverage, particle distribution, orientation or size? Can this behavior be modified and controlled by other external means?

It is the purpose of this research work to address these interrelated problems and shed light on some of the open questions on this area which are of great importance from a fundamental point of view. The present work aims to serve as a starting point for the assessment of magnetic exchange mechanisms on supported nanostructures in terms of experimentally accessible macroscopic variables as the composition, surface coverage and external means such as applied EFs.

The first part of this work deals with the indirect magnetic coupling of $3d$ elements in $5d$ substrates. The important questions to be addressed here are: Which factors are responsible for the magnetic alignment between $3d$ components and which implications does this coupling have? How does the spin-polarization of the host depend on and affect the distance between $3d$ elements and vice-versa? What are the consequences of the coupling-dependent host polarization on the magnetization and MAE of the $3d$ - $5d$ alloyed systems? Having this in mind, Chapter 4 investigates the magnetic exchange among $3d$ -impurities in a highly polarizable non-magnetic substrate. One and two-dimensional hosts have been considered where the coupling between Fe and Co dopants is studied as a function of $3d/5d$ concentration. Emphasis is given to the interplay between the local and collective magnetic properties.

The second part of this work focuses on the possibility of controlling the magnetic order in surface nanostructures by means of the external manipulation of exchange interactions. Chapters 5 and 6 investigate the effects of external electric fields (EFs) on the substrate-mediated exchange interactions between surface impurities at noble metal surfaces. Applied EFs are aimed to control the enhancement and modification of the RKKY interference patterns by inducing changes in the adsorption energies and diffusion energy barriers. This process can affect, for instance, the mechanisms and rates of single-atom surface diffusion and thereby modify the self-organization, growth modes and surface alloying processes at low temperatures [70, 71]. Understanding and controlling the RKKY exchange interactions among impurities can be useful in order to tailor the magnetism of larger nanostructures [45]. Chapter 5 is dedicated to investigate the modifications driven by external surface charging on the long-ranged magnetic exchange interaction between Co and Fe substitutional impurities in a Cu(111) surface. Chapter 6 focuses on the effects of an applied EF on the magnetic coupling within and between Mn dimers deposited on Cu(111). This study also explores the dependence of the RKKY interaction on the magnetic state and relative orientation of the particles.

Each of the above described studies has been performed within an accurate quantum *ab-initio* formulation. The fundamentals of this theoretical approach is presented in Chapter 2. Intrinsic differences on the two major parts of this dissertation, where the magnetic behavior is dominated either by the local or by the scattering properties, require the use of particular theoretical techniques in order to provide a most accurate description. These computational methods are introduced in Chapter 3. In addition, a short review on the state-of-the-art research topics is provided as an introduction in Chapters 4, 5 and 6.

CHAPTER 2

Theoretical background

Within the non-relativistic limit of quantum mechanics, the properties of any solid-state system can be described, in theory, avoiding the use of approximations or external parameters. In particular, all the non-dynamical properties can be derived from the solution of the time-independent Schrödinger equation describing the system. In the practice, however, the computation of an exact solution is technically unfeasible even for small sized systems. As a result of the mutual interactions among all electrons and nuclei, the solution of the quantum many-body problem corresponds to a wave-function which depends on the spatial coordinates of all the particles composing the system and the additional electronic spin degrees of freedom. In this sense, already in the case of a simple molecule, the problem lacks of analytical solution and the use of numerical methods soon becomes exceedingly demanding from a computational point of view. In order to cope with these difficulties, different techniques to approximate the exact solution have been developed during the last decades. Among them, the most prominent approaches are based on the density functional theory (DFT). This theory provides an alternative framework to access the ground-state electronic properties of a system. Based on a first-principles or *ab-initio* formulation, DFT allows to transform the many-body problem into an equivalent “single-particle” problem treating the spin-dependent electronic density as the fundamental variable. In this

way, the number of parameters required to describe most static many-body electronic properties can be reduced to the calculation of a real function n_σ of only three spatial coordinates per spin direction. During the last decades, DFT has proven to be a most valuable tool for electronic structure calculations and has become the standard approach for the study of non-dynamical ground-state properties.

The present chapter summarizes the fundamental concepts of density functional theory and introduces some important concepts. Following this theoretical background, Chapter 3 presents the generalities of the two DFT implementations used along this research work.

2.1 The quantum many-particle problem

The properties of any material are driven by the mutual interactions between all the electrons and nuclei which compose it and the influence of any associated external potential. The non-dynamical behavior of this many-body problem is governed by the time-independent Schrödinger equation

$$\hat{H} \Psi_n(\mathbf{x}_1, \mathbf{x}_2, \dots, \mathbf{x}_N, \mathbf{R}_1, \mathbf{R}_2, \dots, \mathbf{R}_M) = E_n \Psi_n(\mathbf{x}_1, \mathbf{x}_2, \dots, \mathbf{x}_N, \mathbf{R}_1, \mathbf{R}_2, \dots, \mathbf{R}_M), \quad (2.1)$$

where the Hamiltonian operator \hat{H} describes all the energy contributions to the many-particle system and E_n represents the eigen-energy of the state Ψ_n . For any external potential \hat{V}_{ext} , \hat{H} can be expressed as the sum $\hat{H} = \hat{T}_e + \hat{T}_N + \hat{V}_{ee} + \hat{V}_{eN} + \hat{V}_{eN} + \hat{V}_{\text{ext}}$, given in terms of the kinetic operators of the electrons and nuclei \hat{T}_e and \hat{T}_N , and the Coulomb operators describing the electron-electron, electron-nucleus and nucleus-nucleus interactions: \hat{V}_{ee} , \hat{V}_{eN} and \hat{V}_{NN} respectively. In a non-relativistic description, the Hamiltonian \hat{H} of a system consisting of N electrons and M nuclei, given in atomic units, takes the form

$$\begin{aligned} \hat{H} = & - \sum_i^N \frac{1}{2} \nabla_i^2 - \sum_j^M \frac{1}{2m_j} \nabla_j^2 + \frac{1}{2} \sum_i^N \sum_{i' \neq i}^N \frac{1}{|\mathbf{r}_i - \mathbf{r}_{i'}|} \\ & + \frac{1}{2} \sum_j^M \sum_{j' \neq j}^M \frac{Z_j Z_{j'}}{|\mathbf{R}_j - \mathbf{R}_{j'}|} - \sum_j^M \sum_i^N \frac{Z_j}{|\mathbf{R}_j - \mathbf{r}_i|}, \quad (2.2) \end{aligned}$$

where Z_j and m_j are the atomic number and mass of the nucleus j . The solutions Ψ_n

of Eq. (2.1) are functions of the set of spatial coordinates of all nuclei $\{\mathbf{R}_j\}$ and the set of spatial and spin coordinates \mathbf{x}_i of all the electrons [$\mathbf{x}_i \equiv (\mathbf{r}_i, \sigma_i)$].

2.1.1 The Born-Oppenheimer approximation

The Born-Oppenheimer or adiabatic approximation offers a first major simplification of the many-particle problem allowing the decoupling of the electronic and nuclear degrees of freedom. The adiabatic approximation is based on the fact that the effective Coulomb forces acting on electrons and nuclei are of the same order of magnitude. Yet, the mass of the nucleus is thousands of times larger than that of the electrons. In consequence, the electrons are expected to follow the nuclear motion much faster than the time-scale of motion of the nuclei. Namely, the electrons can be regarded as particles that follow the nuclear motion adiabatically [72]. One can, therefore, assume that the nuclei are stationary and focus on the electronic motion for a fixed configuration of nuclear positions. Splitting off the terms of the Hamiltonian which concern the motion of the nuclei (i.e., \hat{T}_N and \hat{V}_{NN}), the problem is reduced to the determination of the electronic eigenstates of a Hamiltonian with a fixed set of nuclear coordinates. The equation determining the electronic states is then given by

$$\hat{H}_e \psi_i(\mathbf{x}_1, \mathbf{x}_2, \dots, \mathbf{x}_N) = E_i \psi_i(\mathbf{x}_1, \mathbf{x}_2, \dots, \mathbf{x}_N) \quad (2.3)$$

where the electronic Hamilton operator

$$\hat{H}_e = -\frac{1}{2} \sum_i^N \nabla_i^2 + \frac{1}{2} \sum_i^N \sum_{i' \neq i}^N \frac{1}{|\mathbf{r}_i - \mathbf{r}_{i'}|} - \sum_j^M \sum_i^N \frac{Z_j}{|\mathbf{R}_j - \mathbf{r}_i|} \equiv \hat{T}_e + \hat{V}_{ee} + \hat{V}_{eN}(\{\mathbf{R}_j\}). \quad (2.4)$$

Eq. (2.3) is the time-independent Schrödinger equation for electrons under the potential of classical and static nuclei. However, notice that the resulting eigenvalues E_i depend on the atomic structure. Consequently, the electronic wavefunctions ψ_i depend parametrically on the positions of the nuclei $\{\mathbf{R}_j\}$. Even though the adiabatic approximation reduces the problem to a purely electronic one, the description of a system of N interacting electrons still depends on $4N$ degrees of freedom. This complicated many-particle equation is not separable into simpler single-particle equations because of the interaction term \hat{V}_{ee} . Further approximations are therefore needed, some of which will be briefly discussed below.

2.1.2 Hartree-Fock approximation

A basic approach to approximate the many-body wavefunction is given by the Hartree-Fock method [72–74]. For an N -electron system the wavefunction is approximated by a fully antisymmetric product of N single-particle orbitals. Such many-particle wavefunction fulfills the Pauli exclusion principle and can be represented by a single Slater determinant

$$\psi_{\text{HF}}(\mathbf{x}_1, \mathbf{x}_2, \dots, \mathbf{x}_N) = \frac{1}{\sqrt{N!}} \begin{vmatrix} \psi_1(\mathbf{x}_1) & \psi_2(\mathbf{x}_1) & \dots & \psi_N(\mathbf{x}_1) \\ \psi_1(\mathbf{x}_2) & \psi_2(\mathbf{x}_2) & \dots & \psi_N(\mathbf{x}_2) \\ \vdots & \vdots & \ddots & \vdots \\ \psi_1(\mathbf{x}_N) & \psi_2(\mathbf{x}_N) & \dots & \psi_N(\mathbf{x}_N) \end{vmatrix}, \quad (2.5)$$

where the $\psi_i(\mathbf{x}_i)$ are single-particle wavefunctions. For simplicity, the ψ_i are assumed to be orthonormal. The functions $\psi_i(\mathbf{x}_i)$ are generally written as a product of a space and a spin dependent function (spinor) with the form $\psi_i(\mathbf{x}_i) = \phi_i(\mathbf{r}_i)\chi_i(\boldsymbol{\sigma}_i)$. In terms of the single-particle wavefunctions, the expectation value of the energy in a Slater determinant state $|\psi_{\text{HF}}\rangle$ is given by

$$\begin{aligned} E_{\text{HF}} = \langle \psi_{\text{HF}} | \hat{H} | \psi_{\text{HF}} \rangle &= \sum_i^N \int \frac{1}{2} |\nabla \psi_i(\mathbf{r})|^2 d^3 \mathbf{r} - \sum_i^N \sum_j^M \int \frac{Z_j}{|\mathbf{R}_j - \mathbf{r}_i|} |\psi_i(\mathbf{r})|^2 d^3 \mathbf{r} \\ &+ \frac{1}{2} \sum_i^N \sum_{i' \neq i}^N \int \int |\psi_i(\mathbf{r})|^2 \frac{1}{|\mathbf{r} - \mathbf{r}'|} |\psi_{i'}(\mathbf{r}')|^2 d^3 \mathbf{r} d^3 \mathbf{r}' \\ &- \frac{1}{2} \sum_i^N \sum_{i' \neq i}^N \delta_{\sigma\sigma'} \int \int \psi_i^*(\mathbf{r}) \psi_{i'}^*(\mathbf{r}') \frac{1}{|\mathbf{r} - \mathbf{r}'|} \psi_{i'}(\mathbf{r}) \psi_i(\mathbf{r}') d^3 \mathbf{r} d^3 \mathbf{r}'. \end{aligned} \quad (2.6)$$

The first three terms of Eq. (2.6) correspond, respectively, to the kinetic energy, electron-ion attraction and the classical direct Coulomb repulsion (Hartree energy). The last term is the exchange energy, which arises as a consequence of the antisymmetry of the electronic wavefunction with respect to coordinate exchange.

In the Hartree-Fock approach, the ground-state many-body wavefunction is approximated by the single Slater determinant which minimizes the energy (Eq. 2.6). The minimization of the total energy is taken with respect to all degrees of freedom in the wavefunctions ψ_i , provided that their orthonormality is preserved. This procedure leads to a set of non-linear coupled equations for the single-particle orbitals which

must be solved self-consistently. The self-consistent Hartree-Fock equations can be interpreted as if each particle is subjected to the mean field created by all other particles. The difference between the exact and the Hartree-Fock energies is known as correlation energy. The results obtained by HF and other methods ignoring electronic correlations can significantly deviate from the experimental behavior.

2.2 Density functional theory

The fundamental statement of DFT asserts that all the stationary properties of a many-particle system can be regarded as functionals of the ground-state electronic density n_0 or the spin-resolved density $n_{0\sigma}$ in the presence of an external magnetic field $\mathbf{B}(\mathbf{r})$. This means, n_0 comprises all the information of the ground-state and excited-states contained in the many-particle wavefunctions, solutions of the time-independent Schrödinger equation [75]. A transformation of the many-particle problem is formally possible by considering the electronic density as the fundamental quantity. In this sense, once the properties of the system are regarded as functionals of the electronic density, the many-body properties can be described by a real function of only three spatial coordinates, eventually including the spin variables. The exact transformation, as well as the existence of such functionals, relies on the two well known theorems proposed and demonstrated by Hohenberg and Kohn (HK) in 1964 [76]. However, the explicit shape of the functionals for real many-electron systems is not known, and HK's work does not provide any clue for its construction. The actual breakthrough for the application of the theory was later provided by Kohn and Sham [77]. Their approach allows to transform the remaining interacting-particle problem into an equivalent problem of non-interacting electrons moving under the influence of an *effective* external potential. The following sections review the main concepts concerning these two essential works.

2.2.1 The Hohenberg-Kohn theorems

The approach of Hohenberg and Kohn was the formulation of DFT as an exact theory of quantum many-particle systems. Essentially, the two fundamental theorems state the possibility of an exact representation of the electronic properties of a many-particle system in terms of the ground-state density alone. The original version of these theorems relied on a number of restrictions such as the assumption of a non-degenerate

ground-state. In the meantime, the rigorous foundation of DFT has been extended to all cases of interest (e.g., degenerate ground-states, spin-polarized systems, relativistic systems) [72, 74, 75].

The theorems apply to any system of interacting particles in an external potential $V_{ext}(\mathbf{r})$ described by a Hamiltonian of the form

$$\hat{H} = - \sum_i \frac{1}{2m} \nabla_i^2 + \sum_i V_{ext}(\mathbf{r}_i) + \frac{1}{2} \sum_i \sum_{i' \neq i} \frac{1}{|\mathbf{r}_i - \mathbf{r}_{i'}|}. \quad (2.7)$$

For simplicity, we assume that no external magnetic field is present. The first theorem demonstrates that the external potential, and hence the total energy of the system, are unique functionals of the ground-state electronic density. For a non-degenerate ground-state, the theorem states: “For any system of interacting electrons under an external potential $V_{ext}(\mathbf{r})$, the potential $V_{ext}(\mathbf{r})$ is uniquely determined, except for a constant term, by the ground-state electronic density $n_0(\mathbf{r})$ ”. In other words, any other external potential $V'_{ext}(\mathbf{r})$ giving rise to the same ground-state electronic density $n'_0(\mathbf{r}) = n_0(\mathbf{r})$, differs from $V_{ext}(\mathbf{r})$ by at most a constant shift. Furthermore, since the potential $V_{ext}(\mathbf{r})$ entirely determines the Hamiltonian except for a trivial additive constant, one concludes that all many-body eigenfunctions of \hat{H} , and therefore all the ground-state and excited-states properties, are completely determined given the ground-state electronic density $n_0(\mathbf{r})$ [75, 76]. This means, the knowledge of $n_0(\mathbf{r})$ should in principle allow to infer the external potential, wavefunctions, and hence, all other observables.

In the non-degenerate case, the solution of the Schrödinger equation corresponding to the Hamiltonian (2.7) can be regarded as a map between the set of external potentials $\{V_{ext}(\mathbf{r})\}$ which differ by more than a constant term, and the set of resulting ground-state wavefunctions $\{|\psi_0\rangle\}$. A second map can be defined between the set $\{|\psi_0\rangle\}$ and the set of associated ground state densities $\{n_0\}$ connected to the elements of $\{|\psi_0\rangle\}$ by $n_0 = \langle \psi_0 | \hat{n}(\mathbf{r}) | \psi_0 \rangle$ [72]. Mathematically, one may write

$$V_{ext} \implies \psi_0(\mathbf{r}_1, \mathbf{r}_2, \dots, \mathbf{r}_N) \implies \langle \psi_0 | \hat{n}(\mathbf{r}) | \psi_0 \rangle = n_0(\mathbf{r}).$$

The validity of the first HK theorem relies on the demonstration that both maps are injective and, therefore, can be inverted:

$$n_0(\mathbf{r}) \implies V_{ext} \implies \psi_0(\mathbf{r}_1, \mathbf{r}_2, \dots, \mathbf{r}_N)$$

In this way, one obtains a one-to-one correspondence between the external potential $V_{ext}(\mathbf{r})$, the ground-state wavefunction $|\psi_0\rangle$ and the associated electronic density n_0 .

The existence of the functional $|\psi[n]\rangle$, for which $|\psi_0\rangle = |\psi[n_0]\rangle$ holds, leads, in the absence of degeneracies, to the possibility of expressing any ground-state observable quantity in terms of n_0 . In particular, the total energy can be regarded as a functional of the density defined as $E[n] = \langle \psi[n] | \hat{H} | \psi[n] \rangle$ (still in the case of a degenerate ground state) [72]. In addition, a minimum principle exists for the total energy functional $E[n]$ such that, for n_0 the ground-state density, $E[n_0] < E[n'_0]$ for all $n'_0 \neq n_0$.

Following the previous ideas, the second theorem, which completes the basic framework of the DFT, states: “For an N -electron system in an external potential $V_{ext}(\mathbf{r})$, a universal (system-independent) functional for the energy $E[n]$ can be defined in terms of the electron density $n(\mathbf{r})$. For any particular $V_{ext}(\mathbf{r})$, the exact ground-state energy corresponds to the global minimum of this functional $\min \{E[n]\} = E[n_0] \equiv E_0$, where the density n_0 , which minimizes $E[n]$, is the exact ground-state electronic density with energy E_0 ”. The energy functional is expressed as

$$E[n] = F[n] + \int d\mathbf{r} V_{ext}(\mathbf{r})n(\mathbf{r}), \quad (2.8)$$

where $F[n] = T_e[n] + V_{ee}[n]$ is a universal functional of the density. In consequence, if the functional $F[n]$ would be known, the exact ground-state energy and density may, in principle, be found by the minimization of the total energy functional in (2.8) with respect to possible variations of the electronic density function $n(\mathbf{r})$ following the variational equation

$$\frac{\delta}{\delta n(\mathbf{r})} \left(E[n] - \mu \left[\int d^3\mathbf{r} n(\mathbf{r}) - N \right] \right) = 0. \quad (2.9)$$

In Eq. (2.9), the Lagrange multiplier μ ensures that the many-particle density $n(\mathbf{r})$ corresponds to a given number of particles. Yet, an exact analytical expression for the kinetic energy $T_e[n]$ and the electronic interaction $V_{ee}[n]$ as functionals of the density is missing and, thus, the straightforward computation of $n_0(\mathbf{r})$ following Eq. (2.9) is impossible. Furthermore, the question arises whether such minimized function actually describes a physical density (i.e., a density resulting from an antisymmetric wavefunction and corresponding ground-state solution of the Schrödinger equation for some external potential V_{ext}) [72, 74, 75, 78]. Finally, notice that the minimization of (2.8) leads, in principle, to the exact ground-state density and energy. However, the functional does not provide any information concerning excited states [75].

Constrained search formulation

An important improvement on the definition of the energy functional given by Hohenberg and Kohn was introduced later by Levy and Lieb (LL) [79]. Their proposal defines a two-step procedure for the minimization of the total energy. From the general expression for the energy in terms of the many-particle wavefunction

$$E \equiv \langle \hat{H} \rangle = \langle \psi | \hat{T}_e | \psi \rangle + \langle \psi | \hat{V}_{ee} | \psi \rangle + \int d^3\mathbf{r} V_{ext}(\mathbf{r})n(\mathbf{r}), \quad (2.10)$$

the ground-state is found by the minimization of (2.10) with respect to all the variables in ψ . This minimization can be carried out by considering first only the subset of many-particle wavefunctions which yield to the same electronic density $n(\mathbf{r})$. In this way, one can define a unique lowest energy corresponding to that particular density. The ground-state is then found by the minimization of

$$E[n] = \min_{\psi \rightarrow n(\mathbf{r})} \left[\langle \psi | \hat{T}_e | \psi \rangle + \langle \psi | \hat{V}_{ee} | \psi \rangle \right] + \int d^3\mathbf{r} V_{ext}(\mathbf{r})n(\mathbf{r}) \equiv F_{LL}[n] + \int d^3\mathbf{r} V_{ext}(\mathbf{r})n(\mathbf{r}), \quad (2.11)$$

with respect to $n(\mathbf{r})$ where the Levy-Lieb functional $F_{LL}[n]$ is an expressed functional of the density. In fact, the functional $F_{LL}[n]$ corresponds to the minimum of the sum of the kinetic and interaction energies from all possible wavefunctions giving rise to the given density $n(\mathbf{r})$. In contrast to the original Hohenberg-Kohn functional, which is defined only for densities generated from the ground-state of an external potential V_{ext} whose conditions are generally unknown, the LL formulation has the advantage of being defined for any density $n(\mathbf{r})$ resulting from an N -electrons wavefunction. The existence of such wavefunction (so-called “N-representability”) is known for any finite non-negative differentiable function $n(\mathbf{r})$ [72, 74, 75, 80].

2.2.2 The Kohn-Sham equations

The fundamental theorems of DFT show that the ground-state electronic properties of a many-electron system are uniquely determined by the ground-state electronic density. Any observable quantity can be, then, regarded as a functional of the density. However, the theorems do not provide any guide on how to compute them. In this section we review the approach proposed by Kohn and Sham which allows to compute a convenient approximation of the ground-state density [77]. The Kohn-Sham construction relies upon the assumption that the exact ground-state density of the

interacting electron system can be represented by the ground-state density of a *fictitious* system of *non-interacting particles*. Although no rigorous proof of the validity of this assumption for real systems exists, this formulation is unquestionably the most successful and widespread method in which DFT has been applied.

The Kohn-Sham formalism introduces an auxiliary system of non-interacting electrons moving under an *effective* single-particle potential $v_{eff}(\mathbf{r})$, which yields the same ground-state electronic density as the real interacting system. The exact connection between the real and *fictitious* systems is obtained by rewriting Eq. (2.8) as

$$E[n] = T_e[n] + \frac{1}{2} \int d\mathbf{r} \int d\mathbf{r}' \frac{n(\mathbf{r})n(\mathbf{r}')}{|\mathbf{r} - \mathbf{r}'|} + \int d\mathbf{r} V_{ext}(\mathbf{r})n(\mathbf{r}) + E_{xc}[n] \equiv \\ \equiv T + E_H + E_{ext} + E_{xc}. \quad (2.12)$$

The so-called exchange-correlation energy $E_{xc}[n]$ accounts for the difference between the exact total interacting energy and the sum of the non-interacting kinetic energy and the Hartree energy.

For a non-interacting electron system, Eq. (2.3) becomes separable and the many-body wavefunction is given by a Slater determinant of occupied single-particle states (see Sec. 2.1.2) [72, 74, 75]. Moreover, the kinetic energy T_e can be expressed as the sum of the expectation values of the kinetic operator for each of the one-electron wavefunctions ψ_i . The single-particle wavefunctions are connected to the electronic density via

$$n(\mathbf{r}) = \sum_{i=1}^N |\psi_i(\mathbf{r})|^2, \quad (2.13)$$

where the sum runs over all occupied states.

Recalling the Hohenberg-Kohn theorems, the ground-state energy and density are found by minimizing the energy functional of Eq. (2.12) [see (2.9)]. The variation (2.9) can be taken in terms of the single-particle orbitals ψ_i . At the minimum, it holds

$$\frac{\delta E}{\delta \psi_i^*(\mathbf{r})} = \frac{\delta T_e}{\delta \psi_i^*(\mathbf{r})} + \left[\frac{\delta E_H}{\delta n(\mathbf{r})} + \frac{\delta E_{ext}}{\delta n(\mathbf{r})} + \frac{\delta E_{xc}}{\delta n(\mathbf{r})} \right] \frac{\delta n(\mathbf{r})}{\delta \psi_i^*(\mathbf{r})} = 0 \quad (2.14)$$

where the minimization is to be taken under orthonormalization conditions for the single-particle wavefunctions ψ_i . A set of self-consistent single-particle equations, known as Kohn-Sham equations, is obtained from the minimization:

$$\left\{ -\frac{1}{2}\nabla^2 + v_{\text{eff}}(\mathbf{r}) \right\} \psi_i(\mathbf{r}) = \varepsilon_i \psi_i(\mathbf{r}). \quad (2.15)$$

The set of Schrödinger-like equations (2.15) corresponds to that of a system of non-interacting particles moving under the influence of the effective potential

$$v_{\text{eff}}[\mathbf{r}, n(\mathbf{r})] = V_{\text{ext}}(\mathbf{r}) + \int d\mathbf{r}' \frac{n(\mathbf{r}')}{|\mathbf{r} - \mathbf{r}'|} + \frac{\delta E_{xc}[n(\mathbf{r})]}{\delta n(\mathbf{r})}. \quad (2.16)$$

where $V_{\text{ext}}(\mathbf{r})$ is the external (e.g., ionic) potential, the second term corresponds to the Hartree potential and the last term is defined as the exchange-correlation potential. Furthermore, the electronic density is computed as given in (2.13) with the single-particle states ψ_i solutions of Eqs. (2.15). Notice that, in Eqs. (2.15), the effective potential v_{eff} depends likewise on the electronic density and, therefore, a self-consistent solution is required. In practice, the problem is usually solved by using an iterative procedure [72, 74, 75].

Spin-polarized systems

The Kohn-Sham formulation can be extended to systems under the effect of an external magnetic field \mathbf{B}_{ext} by generalizing the arguments of Sec. 2.2.1 to take into account, besides the electronic density $n(\mathbf{r}) = n(\mathbf{r}, \sigma = \uparrow) + n(\mathbf{r}, \sigma = \downarrow)$, the spin density $m(\mathbf{r}) = n(\mathbf{r}, \sigma = \uparrow) - n(\mathbf{r}, \sigma = \downarrow)$ [72, 75]. One assumes the existence of a non interacting system, with total energy

$$E[n, \mathbf{m}] = T[n, \mathbf{m}] + E_H[n] + \int d\mathbf{r} \{V_{\text{ext}}n + \mathbf{B}_{\text{ext}} \cdot \mathbf{m}\} + E_{xc}[n, \mathbf{m}] \quad (2.17)$$

and the same ground-state electronic density

$$n(\mathbf{r}) = \sum_{\sigma} \sum_i |\psi_i(\mathbf{r}, \sigma)|^2 \quad (2.18)$$

and magnetization density

$$\mathbf{m}(\mathbf{r}) = \mu_B \sum_{\sigma, \sigma'} \sum_i \psi_i^*(\mathbf{r}, \sigma) \boldsymbol{\sigma}_{\sigma\sigma'} \psi_i(\mathbf{r}, \sigma) \quad (2.19)$$

as the interacting system. In Eq. (2.19), $\boldsymbol{\sigma}_{\sigma,\sigma'}$ stands for the vector of Pauli matrices (see also Sec. 2.4.2). Minimization of $E[n, \mathbf{m}]$ yields the spin-dependent Kohn-Sham equations

$$\left\{ -\frac{1}{2}\nabla^2 + v_s^\sigma[n_\uparrow, n_\downarrow](\mathbf{r}) \right\} \psi_{i\sigma}(\mathbf{r}) = \varepsilon_{i\sigma} \psi_{i\sigma}(\mathbf{r}), \quad (2.20)$$

where, besides the external magnetic field \mathbf{B}_{ext} , the exchange-correlation term involves an additional contribution to the spin dependence of the potential. For simplicity, we have assumed here that \mathbf{B}_{ext} and $\mathbf{m}(\mathbf{r})$ are collinear for all \mathbf{r} . Notice that the Kohn-Sham spin-dependent scheme is essential even in the absence of external magnetic fields whenever the number of electrons of the system is odd or the ground-state exhibits spontaneous nonzero magnetic moments.

2.2.3 Exchange-correlation functionals

Following the Hohenberg-Kohn theorems and the Kohn-Sham formulation, an exact solution for the many-electron problem could be obtained from Eqs. (2.15) or (2.20). However, one still has to deal with the unknown functional for the exchange-correlation energy E_{xc} , for which some approximation is required. In the following, the approximations relevant for this work are briefly discussed.

Local-density Approximation

A first approximation to the exchange-correlation potential can be formulated in terms of the local electronic density alone, i.e., the local value of $n(\mathbf{r})$ at each point of the space \mathbf{r} disregarding a possible dependence on its derivatives and other non-local contributions [72, 74, 75, 81]. Such an approach was first introduced by Kohn and Sham in 1965 [77] and is known as local-density approximation (LDA) [82]. It is still nowadays one of the most widely used methods of electronic structure calculations. The general expression for the energy functional within the LDA has the form:

$$E_{xc} = \int \varepsilon_{xc}[n(\mathbf{r})]n(\mathbf{r})d\mathbf{r}, \quad (2.21)$$

where the exchange-correlation energy per particle ε_{xc} is usually constructed assuming

that the exchange-correlation energy at any point \mathbf{r} is the same as that of a locally uniform electron gas with the same density $n(\mathbf{r})$. This condition is fairly fulfilled in those systems where the electronic density varies slowly, as it is for instance, in the case of simple metals. Nevertheless, LDA works remarkably well even in strongly inhomogeneous cases such as atoms and molecules [83]. The reason of its success relies on physically relevant conditions on the definition of ε_{xc} , which satisfies important the sum rules for the exchange-correlation hole. This restriction is not trivially fulfilled by an arbitrary function [74]. Another reason is that the angular average of the exchange-correlation hole density is very well described by the LDA even if the exchange correlation hole density distribution is highly anisotropic (e.g., in atoms or near surfaces).

The generalization of the LDA for spin-polarized systems, known as local spin-density approximation (LSDA) [84], is straightforward considering densities for the two independent spin directions $n_{\uparrow}(\mathbf{r})$ and $n_{\downarrow}(\mathbf{r})$ with $n(\mathbf{r}) = n_{\uparrow}(\mathbf{r}) + n_{\downarrow}(\mathbf{r})$. The general form of the LSDA functional is simply

$$E_{xc}[n_{\uparrow}, n_{\downarrow}] = \int \varepsilon_{xc}[n_{\uparrow}(\mathbf{r}), n_{\downarrow}(\mathbf{r})]n(\mathbf{r})d\mathbf{r}. \quad (2.22)$$

One of the most common expressions for $\varepsilon_{xc}[n_{\uparrow}(\mathbf{r}), n_{\downarrow}(\mathbf{r})]$ in Eq. (2.22) is given by

$$\begin{aligned} \varepsilon_{xc}[n_{\uparrow}(\mathbf{r}), n_{\downarrow}(\mathbf{r})] &= -\frac{3e^2}{4\pi}(3\pi^2)^{\frac{1}{3}} \left[\frac{n_{\uparrow}(\mathbf{r})^{\frac{4}{3}} + n_{\downarrow}(\mathbf{r})^{\frac{4}{3}}}{n(\mathbf{r})} \right] \\ &= \varepsilon_{xc}^P + (\varepsilon_{xc}^{FM} - \varepsilon_{xc}^P) \left[\frac{(n_{\uparrow}/n)^{\frac{4}{3}} + (n_{\downarrow}/n)^{\frac{4}{3}} - (1/2)^{\frac{1}{3}}}{1 - (1/2)^{\frac{1}{3}}} \right] \end{aligned} \quad (2.23)$$

where $\varepsilon_{xc}^P = \varepsilon_{xc}(n_{\uparrow} = n_{\downarrow} = n/2)$ corresponds to the non-spin-polarized value and $\varepsilon_{xc}^{FM} = \varepsilon_{xc}(n_{\uparrow} = n, n_{\downarrow} = 0)$ to the fully polarized ferromagnetic (FM) case.

Although the electronic structure can be reasonably well described within the LDA approximation, the predictions of equilibrium lattice parameters are frequently smaller than in experiment and the binding energies are often overestimated.

Generalized gradient approximation

In LDA approximation, the exchange-correlation energy of the true density is replaced with that of a locally uniform electron gas. This approach suffers of strong limitations for the description of situations where the density undergoes rapid changes as it often occurs, for instance, within low-dimensional systems [72, 74, 75, 83]. An improved description can be obtained by taking into account the dependence of the exchange-correlation functional on the local gradient of the electron density. Such functionals are known as generalized gradient approximations (GGA) and can be written as

$$E_{xc} = E_{xc}[n(\mathbf{r}), \nabla n(\mathbf{r})]. \quad (2.24)$$

In the GGA, the density-gradient dependence of the functional facilitates density inhomogeneity. The GGA has demonstrated to improve the description of the binding energies and, accordingly, provides better results of the optimized geometries [72]. In comparison with LDA, GGA expands and softens bonds improving total energies, energy barriers and structural energy differences.

GGA is a semi-local approximation in the sense that the exchange correlation potential at each point \mathbf{r} depends on the value of the density and its gradient at the exact same point \mathbf{r} . Specifically, the energy functional has the general form

$$E_{xc}[n_{\uparrow}, n_{\downarrow}] = \int f [n_{\uparrow}(\mathbf{r}), n_{\downarrow}(\mathbf{r}), \nabla n_{\uparrow}(\mathbf{r}), \nabla n_{\downarrow}(\mathbf{r})] d\mathbf{r}. \quad (2.25)$$

Several different parametrizations of the GGA have been developed [85]. The functionals are typically constructed considering a density-gradient expansion for the exchange-correlation hole around the electron, in a system of slowly varying density [72, 85].

2.3 Bloch's theorem and plane waves

The present section follows the discussion of Ref. [74] on the solution of the Schrödinger equation in a plane wave basis.

Any periodic function can be decomposed into the complete set of Fourier components. In particular, for the eigenstates ψ_i of a single-electron Schrödinger equation, for example the Kohn-Sham Eqs (2.15), an expansion can be written in terms of

orthonormal plane waves $|\mathbf{q}\rangle$ satisfying

$$\langle \mathbf{q}' | \mathbf{q} \rangle \equiv \frac{1}{\Omega} \int_{\Omega} d\mathbf{r} \exp(-i\mathbf{q}' \cdot \mathbf{r}) \exp(i\mathbf{q} \cdot \mathbf{r}) = \delta_{\mathbf{q},\mathbf{q}'} \quad (2.26)$$

as

$$\psi_i(\mathbf{r}) = \sum_{\mathbf{q}} c_{i,\mathbf{q}} \frac{1}{\sqrt{\Omega}} \exp(i\mathbf{q} \cdot \mathbf{r}). \quad (2.27)$$

In the expression (2.27) the states ψ_i are normalized and subject to periodic boundary conditions in a volume Ω which is allowed to go to infinity. In a similar way, for electrons in a periodic crystal, the ionic effective potential v_{eff} can be expressed as

$$v_{eff}(\mathbf{r}) = \sum_m v_{eff}(\mathbf{G}_m) \exp(i\mathbf{G}_m \cdot \mathbf{r}), \quad (2.28)$$

where the \mathbf{G}_m are the reciprocal vectors of the crystal lattice and

$$v_{eff}(\mathbf{G}) = \frac{1}{\Omega_{uc}} \int_{\Omega_{uc}} v_{eff}(\mathbf{r}) \exp(-i\mathbf{G} \cdot \mathbf{r}) d\mathbf{r} \quad (2.29)$$

with Ω_{uc} the volume of the primitive unit cell. According to this, the resulting matrix elements of the corresponding Schrödinger Hamiltonian in Fourier space are

$$\langle \mathbf{q}' | \hat{H} | \mathbf{q} \rangle = \langle \mathbf{q}' | -\frac{\hbar^2}{2m_e} \nabla^2 + v_{eff} | \mathbf{q} \rangle = \frac{\hbar^2}{2m_e} |q|^2 \delta_{\mathbf{q},\mathbf{q}'} + \sum_m v_{eff}(\mathbf{G}_m) \delta_{\mathbf{q}-\mathbf{q}',\mathbf{G}_m}, \quad (2.30)$$

where the last terms are non-zero only if \mathbf{q} and \mathbf{q}' differ by the reciprocal lattice vector \mathbf{G}_m . From the last expression, it is clear that plane waves are particularly appropriate to describe electrons in periodic crystals. By defining $\mathbf{q} = \mathbf{k} + \mathbf{G}_m$ and $\mathbf{q}' = \mathbf{k} + \mathbf{G}'_m$, the Schrödinger equation can be rewritten for any given \mathbf{k} in the matrix form

$$\sum_{m'} H_{m,m'}(\mathbf{k}) c_{i,m'}(\mathbf{k}) = \varepsilon_i(\mathbf{k}) c_{i,m}(\mathbf{k}) \quad (2.31)$$

where

$$H_{m,m'}(\mathbf{k}) = \langle \mathbf{k} + \mathbf{G}_m | \hat{H} | \mathbf{k} + \mathbf{G}'_m \rangle = \frac{\hbar^2}{2m_e} |\mathbf{k} + \mathbf{G}_m|^2 \delta_{m,m'} + v_P(\mathbf{G}_m - \mathbf{G}'_m). \quad (2.32)$$

From (2.27) and (2.32) it follows that the eigenfunctions of Eq. (2.31) for a given \mathbf{k} can be written as

$$\psi_{i,\mathbf{k}}(\mathbf{r}) = \sum_m c_{i,m}(\mathbf{k}) \frac{1}{\sqrt{\Omega}} \exp(i(\mathbf{k} + \mathbf{G}_m) \cdot \mathbf{r}) = \sqrt{\frac{\Omega_{uc}}{\Omega}} \exp(i\mathbf{k} \cdot \mathbf{r}) U_{i,\mathbf{k}}(\mathbf{r}) \quad (2.33)$$

where

$$U_{i,\mathbf{k}}(\mathbf{r}) = \frac{1}{\sqrt{\Omega_{uc}}} \sum_m c_{i,m}(\mathbf{k}) \exp(i\mathbf{G}_m \cdot \mathbf{r}) \quad (2.34)$$

is a function with the periodicity of the crystal. This result is known as Bloch theorem. Notice that, in the limit $\Omega \rightarrow \infty$, the energies $\varepsilon_i(\mathbf{k})$ are continuous functions of the wave vector \mathbf{k} and form energy bands which can be labeled with the band index i . The eigenvalues for a given i are periodic in \mathbf{k} with the periodicity of a reciprocal lattice vector. Therefore, only values of \mathbf{k} within the first or reduced *Brillouin zone* need to be considered.

2.4 Coupling between localized magnetic moments

A simplified picture of magnetism regards magnetic order as the result of the interaction among localized microscopic magnetic moments. The magnetic behavior can be then represented by an effective spin-spin Heisenberg Hamiltonian

$$H = - \sum J_{mn} \mathbf{S}_m \cdot \mathbf{S}_n \quad (2.35)$$

where \mathbf{S}_m denotes the spin vector of the m_{th} localized moment, and J_{mn} is defined as the exchange parameter. The \mathbf{S}_m may represent, for example, the spin of single electrons localized at magnetic impurities in a non-magnetic material, the total d -electron spin moment of TM ions in a crystal lattice or the combined spin and orbital moments in rare-earth materials. The exchange constants J_{mn} of the model account for the energy contribution from the pair of moments at the m_{th} and n_{th} sites. The sign of J_{mn} determines a favorable ferromagnetic (FM) or antiferromagnetic (AF) coupling. In real materials, the legitimacy of expression (2.35) is not evident and the rendering of the exchange parameters often fails to predict the experimental magnetic behavior. However, in special situations, as it is the case of the RKKY interaction discussed below, the use of this highly simplified Hamiltonian is justified.

2.4.1 The RKKY interaction

The Hamiltonian (2.35) is often used to describe lattices of magnetic atoms where only the coupling between nearest-neighbors is relevant. Under certain circumstances, a *super-exchange* magnetic coupling between next NN atomic spin moments can result

from the indirect interaction mediated by an intermediate non-magnetic atom [86, 87]. Furthermore, in some non-magnetic metals, the localized wavefunctions of an embedded magnetic atom couple with the conduction electron band, inducing a spin polarization of the free electron gas. In this way, an effective exchange-coupling mechanism between embedded localized magnetic moments can be driven by the polarization of the delocalized conduction electrons of the host.

Consider the interaction between the localized spin \mathbf{S} of a magnetic impurity embedded in a bulk metal and the spin \mathbf{s} of an electron in the conduction band of the host. An effective coupling is written in the form

$$H_{sb} = -J\mathbf{S} \cdot \mathbf{s}\delta(\mathbf{r}), \quad (2.36)$$

where J is a constant of dimension energy times volume [88]. The wavefunctions of the conduction band can be represented by plane waves $U_{\mathbf{k}\sigma} = \frac{1}{\sqrt{V}} \exp(i\mathbf{k} \cdot \mathbf{r})|\sigma\rangle$ normalized within the volume V of the crystal bulk.

At the first order in the perturbation H_{sb} , a state $U_{\mathbf{k}\uparrow}$ is scattered into a state

$$\tilde{U}_{\mathbf{k}\uparrow} = \frac{1}{\sqrt{V}} \exp(i\mathbf{k} \cdot \mathbf{r})|\uparrow\rangle + \frac{1}{\sqrt{V}} \frac{2mJ \exp(ikr)}{\hbar^2} \frac{1}{4\pi r} \mathbf{S} \cdot \mathbf{s} |\uparrow\rangle \quad (2.37)$$

giving rise to a density of spin up electrons given by

$$n_{\mathbf{k}\uparrow}(\mathbf{r}) = |\tilde{U}_{\mathbf{k}\uparrow}|^2 = \frac{1}{V} + \frac{1}{V} \left[\frac{mJ}{\hbar^2} S_z \frac{\exp(ikr)}{4\pi r} \exp(-i\mathbf{k} \cdot \mathbf{r}) + c.c. \right] + O(J^2). \quad (2.38)$$

where *c.c.* indicates the complex conjugate [88]. Integrating Eq. (2.38) over all \mathbf{k} vectors within the Fermi sphere, one obtains

$$\begin{aligned} n_{\mathbf{k}\uparrow}(\mathbf{r}) &= n_0 + \frac{mJ}{\hbar^2} S_z \frac{1}{(2\pi)^3} \int_{F_s} \left[\frac{\exp(ikr)}{4\pi r} \exp(-i\mathbf{k} \cdot \mathbf{r}) + c.c. \right] \\ &= n_0 + \frac{mJ}{\hbar^2} S_z \frac{1}{(2\pi)^3} \frac{1}{r^2} \int^{k_F} 2 \cos kr \cdot \sin kr \cdot k \, dk \\ &= n_0 + \frac{4mJ}{\hbar^2} \frac{k_F^4}{(2\pi)^3} F(2k_F r) S_z, \quad \text{where } F(x) = \frac{x \cos x - \sin x}{x^4} \end{aligned} \quad (2.39)$$

Similar calculations can be performed for $n_{\mathbf{k}\downarrow}(\mathbf{r})$. A net spin polarization, which

oscillates as a function of the distance r from the impurity site, is found from the difference

$$n_{\mathbf{k}\uparrow}(\mathbf{r}) - n_{\mathbf{k}\downarrow}(\mathbf{r}) = -\frac{8mJ}{\hbar^2} \frac{k_F^4}{(2\pi)^3} F(2k_F r) S_z. \quad (2.40)$$

Furthermore, for a pair of localized spins \mathbf{S}_1 and \mathbf{S}_2 located at $\mathbf{r}_1 = 0$ and $\mathbf{r}_2 = \mathbf{R}$, an indirect exchange coupling results from the interaction of \mathbf{S}_2 with the spin polarization created by \mathbf{S}_1 . The interaction energy is given by

$$\begin{aligned} \Delta E(\mathbf{R}) &= \sum_{\mathbf{k}\sigma} \langle \tilde{U}_{\mathbf{k}\sigma} | -J\mathbf{S}_2 \cdot \mathbf{s} \delta(\mathbf{r} - \mathbf{R}) | \tilde{U}_{\mathbf{k}\sigma} \rangle \\ &= -\frac{4mJ^2}{\hbar^2} \frac{k_F^4}{(2\pi)^3} F(2k_F R) \mathbf{S}_1 \cdot \mathbf{S}_2, \end{aligned} \quad (2.41)$$

where the last expression is obtained using the property of the scalar product:

$$\langle \uparrow | \mathbf{S}_1 \cdot \mathbf{s} \mathbf{S}_2 \cdot \mathbf{s} | \uparrow \rangle + \langle \downarrow | \mathbf{S}_1 \cdot \mathbf{s} \mathbf{S}_2 \cdot \mathbf{s} | \downarrow \rangle = \frac{1}{2} \mathbf{S}_1 \cdot \mathbf{S}_2.$$

This effective spin coupling, known as the Rudderman-Kittel-Kasuya-Yosida (RKKY) interaction, oscillates from antiferromagnetic to ferromagnetic for increasing separation distances between the localized moments [29–31]. For the RKKY interaction mechanism mediated by a metallic two-dimensional band (e.g., surface states), the general form for the effective exchange coupling is given by

$$J_{mn}(R_{mn}) \sim \frac{\cos(2\mathbf{k}_F \cdot \mathbf{R}_{mn})}{R_{mn}^2} \quad (2.42)$$

where \mathbf{k}_F is the Fermi wavevector of the conducting host, \mathbf{R}_{mn} is the vector of length R_{mn} connecting the m_{th} and n_{th} localized moments and the range of the interaction is determined by a quadratic decay exponent.

2.4.2 Noncollinear formulation

For the description of ferromagnetic (FM) and antiferromagnetic (AF) materials, it is sufficient to consider the magnetic moment as having only two possible (collinear) orientations: parallel and antiparallel respect to each other. Nevertheless, noncollinear ground-state magnetic arrangements can emerge as a result of frustrated magnetic interactions (e.g., AF order restricted by the crystal geometry in triangular lattices). The description of such kind of system requires to specify the spatial orientation of the spin-quantization axis and allow its variation from site to site.

In a collinear formulation, although the relative orientation between local moments can be determined, the orientation of this magnetization with respect to some frame of reference (e.g., with respect to the underlying crystal lattice) is not defined [68, 74, 89]. In real systems, the spin-orbit interaction couples the magnetic moments to the crystal lattice giving rise to the magnetocrystalline anisotropy and determining the ground-state magnetic orientation (see Sec. 2.5). Therefore, the use of a noncollinear scheme for the treatment of the SO coupling and the study of magnetic anisotropy is compelling.

In a noncollinear formulation of spin-polarized DFT, the electronic and magnetization densities are expressed in terms of the 2×2 density matrix with elements $n^{\alpha\beta}(\mathbf{r})$ as

$$n(\mathbf{r}) = \text{Tr}[n^{\alpha\beta}(\mathbf{r})] = \sum_{\alpha} n^{\alpha\alpha}(\mathbf{r}) \quad , \quad \mathbf{m}(\mathbf{r}) = \sum_{\alpha\beta} n^{\alpha\beta}(\mathbf{r}) \cdot \boldsymbol{\sigma}^{\alpha\beta} \quad (2.43)$$

where $\boldsymbol{\sigma}^{\alpha\beta} = (\sigma_x, \sigma_y, \sigma_z)$ stands for the vector of Pauli spin matrices defined as

$$\sigma_x = \begin{pmatrix} 0 & 1 \\ 1 & 0 \end{pmatrix}, \quad \sigma_y = \begin{pmatrix} 0 & -i \\ i & 0 \end{pmatrix}, \quad \sigma_z = \begin{pmatrix} 1 & 0 \\ 0 & -1 \end{pmatrix}. \quad (2.44)$$

2.5 The spin-orbit coupling

Considering a bounded electron as a classical electric charge circulating around the nucleus, a magnetic field can be associated to its motion. Equivalently, in the reference frame of the electron, this movement can be regarded as a current loop generated by the nucleus charge circulating around the electron [90]. In response to the magnetic field created by its orbital motion around the nucleus, the spin associated to an electron experiences an effective potential which tends to align its orientation with the direction of the magnetic field, giving rise to the spin-orbit coupling (SOC) effect. For a nuclear electrostatic potential $V(r)$ and the electron mass m_e , an approximation of the SOC interaction can be taken into account in the non-relativistic Hamiltonian as an additional term of the form

$$\hat{H}_{SO} = \sum_i \frac{1}{2m_e^2 c^2} \frac{1}{r} \frac{\partial V(r)}{\partial r} \hat{\mathbf{S}}_i \cdot \hat{\mathbf{L}}_i, \quad (2.45)$$

where $\hat{\mathbf{S}}_i$ and $\hat{\mathbf{L}}_i$ are the spin and orbital moment operators of electron i . In Eq. (2.45)

inter-atomic SOC terms are neglected since their contribution is very small in comparison with the intra-atomic values.

For electrons moving at non-relativistic velocities the SOC interaction is very small. However, in heavy atoms this effect becomes important. In the limit $v/c \ll 1$, expression (2.45) provides fairly good results for the spin-orbit coupling of real systems. A rigorous derivation of this term is obtained from the Dirac equation, in which the form of Eq. (2.45) can be regarded as the first order relativistic correction. Besides its contribution to the total energy, to account for this term can become essential for the description of magnetic systems. In particular, the SOC interaction is responsible for the third Hund's rule which determines the relative alignment between the atomic spin and orbital magnetic moments. Namely, since $\partial V(r)/\partial r > 0$ in the near of the atomic nucleus, an electron spin in the ground state will tend to align antiparallel to its angular momentum. As a result, the atomic spin magnetization and orbital moment will be aligned parallel in the ground state of atoms with a less than half-filled shell, while they will be found anti-parallel in atoms having a more than half-filled shell.

Moreover, in larger systems the spin-orbit interaction splits electronic states which are degenerated in a non-relativistic description. Due to the underlying structural dependence involved through the potential $V(r)$, the electronic states and the energy become dependent on the orientation of the magnetization with respect to the crystal lattice. The resulting magnetic anisotropy (MA) is an important consequence of relativistic effects with relevant implications for technological purposes.

2.6 The Hellmann-Feynman theorem

In the discussion of the last sections, the parametrical dependence of the interaction between electrons and nuclei on the set of nuclear positions \mathbf{R}_j (derived in Sec. 2.1.1) has been ignored. However, since the functional $F[n]$ is universal, it is clear that the dependence of the total energy functional on \mathbf{R}_j originates from the term E_{ext} . The first formulation of an expression which relates the force conjugated to any parameter in the Hamiltonian with the expectation value of the derivative of the Hamiltonian with respect to that parameter was introduced in the context of a variational principle by H. Hellmann. This concept was reformulated as an electrostatic theorem by R. Feynman, [91] when considering forces between atoms. His work emphasizes that the force exerted on a given nucleus is simply the electrostatic force resulting from the

charge density distribution of all other nuclei and electrons. The Hellmann-Feynman theorem extends the classical concept of the force conjugate to the position of a nucleus (\mathbf{R}_j) as the derivative of the total energy with respect to the parameter \mathbf{R}_j to its corresponding expression for a quantum system. Namely, that the force can be written as

$$\mathbf{F}_j = -\frac{\partial E}{\partial \mathbf{R}_j} = -\frac{\partial \langle \Psi | \hat{H} | \Psi \rangle}{\partial \mathbf{R}_j}, \quad (2.46)$$

where the derivative is to be taken from the expression of the total energy as the expectation value of the Hamiltonian operator keeping the normalization condition $\langle \Psi | \Psi \rangle = 1$ for all \mathbf{R}_j . Eq. (2.47) implies

$$-\frac{\partial E}{\partial \mathbf{R}_j} = -\langle \Psi | \frac{\partial \hat{H}_e}{\partial \mathbf{R}_j} | \Psi \rangle - \langle \frac{\partial \Psi}{\partial \mathbf{R}_j} | \hat{H}_e | \Psi \rangle - \langle \Psi | \hat{H}_e | \frac{\partial \Psi}{\partial \mathbf{R}_j} \rangle - \frac{\partial E_{NN}}{\partial \mathbf{R}_j}, \quad (2.47)$$

where E_{NN} is the classical energy concerning the electrostatic interaction among the nuclei ($E_{NN} = \langle \hat{V}_{NN} \rangle$, see 2.3) [72, 74, 91]. Considering that

$$\frac{\partial}{\partial \mathbf{R}_j} \langle \Psi | \Psi \rangle = \langle \frac{\partial \Psi}{\partial \mathbf{R}_j} | \Psi \rangle + \langle \Psi | \frac{\partial \Psi}{\partial \mathbf{R}_j} \rangle = 0, \quad (2.48)$$

the derivative consists exclusively of the terms which depend explicitly on the position of the nuclei. Since

$$\frac{\partial \hat{H}_e}{\partial \mathbf{R}_j} = \frac{\partial V_{ext}}{\partial \mathbf{R}_j}, \quad (2.49)$$

the final expression for the force \mathbf{F}_j conjugated to the position of the ion j reads

$$\mathbf{F}_j = -\int d\mathbf{r} n(\mathbf{r}) \frac{\partial V_{ext}}{\partial \mathbf{R}_j} - \frac{\partial E_{NN}}{\partial \mathbf{R}_j} \quad (2.50)$$

with $n(\mathbf{r})$ the electronic density. Thus, the local force depends only on the charge distribution of the electrons and the other nuclei. The Hellmann-Feynman theorem finds application on the evaluation of interatomic forces in molecules and solids, allowing the calculation of their equilibrium geometries.

Computational methods

Over the last decades, DFT has grown in popularity by proving its accuracy and remarkable efficiency in describing the ground-state properties of a large variety of systems. Motivated by this success, an extensive work in molecular and solid state physics has been accomplished along with the development of new computational techniques. Diverse implementations of DFT with different specific capabilities are available nowadays [83]. Throughout the present research work, two state-of-the-art computational methods have been used. This chapter provides a general overview of each of these implementations outlining their most relevant features, differences and distinctive advantages.

3.1 The Vienna *ab-initio* simulation package

The Vienna *ab-initio* simulation package (VASP) is a very efficient and widespread computational code which allows to perform electronic structure calculations within a first principles formulation [92, 93]. VASP provides an implementation of density functional theory based on the self-consistent solution of the Kohn-Sham equations. A plane-wave basis set is used for the expansion of the one-electron wavefunctions [92, 94].

The composition and structure of the system are defined inside a unit cell, which is subject to periodic boundary conditions. Thus, periodic crystal structures can be studied involving a minimal number of atoms. However, non-periodic systems require the construction of large supercells. In particular, isolated atomic structures can be defined by introducing a large vacuum region, which avoids the interaction between neighboring images [94].

The symmetry imposed by the periodic boundary conditions results in Bloch-like electronic states which are characterized by the wave vector \mathbf{k} (see Sec 2.3). The evaluation of important quantities such as the charge density, the density of states and the total energy, which involve an integration over the first Brillouin zone (BZ), are approximated by a weighted sum over a discrete set of \mathbf{k} -points [94]. For instance, the calculation of the band-structure energy requires an integration over the filled bands given by

$$\sum_n \frac{1}{\Omega_{BZ}} \int_{\Omega_{BZ}} \epsilon_{n\mathbf{k}} \Theta(\epsilon_{n\mathbf{k}} - \mu) d\mathbf{k}, \quad (3.1)$$

where $\Theta(x)$ is the Heaviside step function and μ is the chemical potential. The integral over the first Brillouin zone Ω_{BZ} can be replaced by a weighted sum over a discrete set of \mathbf{k} -points

$$\sum_{\mathbf{k}} \omega_{\mathbf{k}} \epsilon_{n\mathbf{k}} \Theta(\epsilon_{n\mathbf{k}} - \mu). \quad (3.2)$$

The accuracy of the calculation is conditioned by the number of \mathbf{k} -points used for the evaluation of (3.2). In metallic systems, the discontinuity of the occupancies at the Fermi-level leads to very slow convergencies of the sum (3.2). VASP employs the method of partial occupancies to reduce the number of \mathbf{k} -points required for an accurate calculation of the band-structure energy. This method consists in replacing $\Theta(\epsilon_{n\mathbf{k}})$ with a smoother function $f(\{\epsilon_{n\mathbf{k}}\})$, which allows a faster convergence preserving at the same time a high accuracy in the evaluation of the sum. Several choices for the function $f(\{\epsilon_{n\mathbf{k}}\})$ are available within the finite temperature approaches and smearing methods implemented in the VASP code.

In the calculations presented in this work, the orthogonality constraints between the valence electrons and the ion cores is described by the projector-augmented wave (PAW) method, which allows accurate frozen core-electron calculations. The PAW method is discussed in Sec. 3.1.1.

Moreover, structural optimizations can be performed within VASP. The instantaneous forces and stress tensors are calculated following the Hellmann-Feynman theorem. These are used to relax the atomic positions towards their lowest-energy configura-

ration (see Sec. 2.6). Steepest-descent, conjugate-gradient and quasi-Newton-Rapson methods are implemented in this context [74, 94].

Finally, VASP has implemented a fully unconstrained approach to noncollinear magnetism which treats the magnetization density as a continuous vector variable of the position [68, 95]. Relativistic effects (i.e., including the spin-orbit coupling interaction) are also treated within this framework. This is a clear improvement with respect to other methods (e.g., those based on the atomic moment approximation) where fixed local quantization axes are considered within each atomic volume.

3.1.1 Projector augmented waves

An accurate description of the wavefunctions in terms of plane-waves alone can result in considerably large basis set requirements. On one side, the core electrons remain tightly bound to the nucleus. They are strongly localized near the ions and do not contribute substantially in the formation of chemical bonds. Being fully occupied, they do not contribute to magnetism either. On the other side, in the case of the valence electrons, the requirement of orthogonality with respect to the core states leads to rapid oscillations of the valence wavefunctions near the ion cores. The projector-augmented wave (PAW) method provides a computationally efficient way to take into account these oscillations without requiring to involve prohibitively large plane wave vectors k (i.e., very short wavelengths) [74, 96–98]. The method uses a linear transformation T which maps the original valence wavefunctions $|\psi_n\rangle$ onto auxiliary functions $|\tilde{\psi}_n\rangle$ with rapid convergency in a plane waves expansion. With $|\psi_n\rangle = T |\tilde{\psi}_n\rangle$, the evaluation of a physical quantity defined by the operator A can be taken in the representation of either the true or the auxiliary wavefunctions as

$$\langle A \rangle = \sum_n f_n \langle \psi_n | A | \psi_n \rangle = \sum_n f_n \langle \tilde{\psi}_n | T^\dagger A T | \tilde{\psi}_n \rangle \quad (3.3)$$

In the PAW method, the transformation is defined to be non-zero only within a spherical augmentation region of radius \mathbf{R} around each atom. Thus, it is expressed in the form

$$T = 1 + \sum_R S_R, \quad (3.4)$$

where S_R accounts for the difference between the real and the pseudo wavefunction around each atom. Starting from the expansion of the wavefunction in a convenient set of atomic partial waves as $|\Psi\rangle = \sum_i |\phi_i\rangle c_i$, one defines a similar expansion for the

auxiliary pseudo wavefunctions $|\tilde{\Psi}\rangle = \sum_i |\tilde{\phi}_i\rangle c_i$, where the pseudo partial waves $|\tilde{\phi}_i\rangle$ obey $S_R|\tilde{\phi}_i\rangle = |\phi_i\rangle - |\tilde{\phi}_i\rangle$. Notice that outside the augmentation regions the pseudo partial waves $|\tilde{\phi}_i\rangle$ are identical to the all-electron partial waves $|\phi_i\rangle$.

The expansion of $|\tilde{\Psi}\rangle$ defines the projector functions $|\tilde{p}_i\rangle$ from which the coefficients c_i are obtained as the product $\langle p_i|\tilde{\Psi}\rangle$. In this sense, the all-electron wavefunctions are finally expressed as

$$|\psi_n\rangle = |\tilde{\psi}_n\rangle + \sum_i (|\phi_i\rangle - |\tilde{\phi}_i\rangle) \langle \tilde{p}_i|\tilde{\psi}_n\rangle. \quad (3.5)$$

Usually, the set of atomic partial waves $|\phi_i\rangle$ is taken from the solution of the Schrödinger equation for the isolated atoms. In fact, in a frozen-core approximation, the density and energy of the core electronic states is retained and the set $|\phi_i\rangle$ is composed only by valence states orthogonal to the core wavefunctions of the atom.

3.2 Green's function Korringa-Kohn-Rostoker method

The Green's function (GF) Korringa-Kohn-Rostoker (KKR) method is based on the multiple-scattering formalism [99–102]. The method deals with the scattering of particles described by a single-particle Hamiltonian with an effective potential of the form

$$v(\mathbf{r}) = v_{ext} + \sum_i v_i(\mathbf{r}), \quad (3.6)$$

where $v_i(\mathbf{r})$ are non-overlapping potentials representing the atoms, and v_{ext} is an external potential which can be set arbitrarily [101, 103–105].

In the KKR method, the space is divided into non-overlapping atomic regions in which each ion is represented by a scattering potential defined within an otherwise potential-free space. Hence, electrons propagating between scattering sites are described by the free propagator Green's function. The KKR formulation allows a separation between the potential and structural attributes of the system by dividing the problem into *single-scattering* and *multiple-scattering* parts. In the first part, the potential dependent single-site scattering problem is solved inside the atomic region in terms of a local GF. In the second, the solution of the structural dependent multiple-scattering problem is found self-consistently by requiring that the incident wave to each atomic potential corresponds to the sum of the outgoing waves from all other scattering centers. As a Green's function formulation, the KKR method has the advantage of avoiding the construction of big supercells and the computation of large wavefunctions by evaluating the electronic properties directly from the

GF [100, 103, 106, 107].

3.2.1 Green's function formulation

The KKR Green's function is defined as the resolvent of the time-independent Schrödinger equation (2.3) with a Dirac-delta inhomogeneity term at \mathbf{r}' :

$$[\hat{H} - E]G(\mathbf{r}, \mathbf{r}'; E) = -\delta(\mathbf{r} - \mathbf{r}'), \quad (3.7)$$

which can be expressed through the operator equation

$$G(E) = [E - \hat{H}]^{-1}. \quad (3.8)$$

For an arbitrary complex energy E (having an infinitesimal positive imaginary part), a formal solution for Eq. (3.7) is given in terms of the complete set of eigenstates ψ_i and eigenvalues ϵ_i of the Hamiltonian as

$$G(\mathbf{r}, \mathbf{r}'; E) = \sum_i \frac{\psi_i(\mathbf{r})\psi_i^*(\mathbf{r}')}{E - \epsilon_i}. \quad (3.9)$$

Thus, the stationary states of the system are given by the poles of $G(E)$. Moreover, Eq. (3.9) entails the relation between the imaginary part of the GF and the energy and space resolved single particle electronic density $n(\mathbf{r}; E)$ where

$$n(\mathbf{r}; E) = -\frac{1}{\pi} \text{Im} G(\mathbf{r}, \mathbf{r}; E). \quad (3.10)$$

The electronic density can be found integrating Eq. (3.10) up to the Fermi level E_F

$$n(\mathbf{r}) = -\frac{1}{\pi} \text{Im} \int_{-\infty}^{E_F} G(\mathbf{r}, \mathbf{r}; E) dE = -\frac{1}{\pi} \text{Im} \int_{-\infty}^{E_F} \text{Tr} (\hat{r} G(E)) dE \quad (3.11)$$

with \hat{r} representing the position operator. In general, it follows from (3.9) that the expectation value of any operator \hat{A} representing a physical quantity can be evaluated directly from the GF by

$$\langle A \rangle = -\frac{1}{\pi} \text{Im} \int_{-\infty}^{E_F} \text{Tr} (\hat{A} G(E)) dE. \quad (3.12)$$

Particularly, the energy-resolved density of states can be obtained straightforwardly from (3.10) as

$$n(E) = -\frac{1}{\pi} \text{Im} \int G(\mathbf{r}, \mathbf{r}; E) d\mathbf{r} = -\frac{1}{\pi} \text{Im} \text{Tr}G(E). \quad (3.13)$$

Thus, the single-particle GF comprises all the information concerning the physical properties contained in the non-interacting Hamiltonian \hat{H} .

3.2.2 The Dyson equation and the Lloyd's formula

The representation of the electronic structure in terms of the GF facilitates the use of a perturbative approach which offers great advantages for the treatment of substitutional impurities, disordered systems and crystal surfaces [100, 107]. Given a perturbing potential V added to a Hamiltonian H_0 , the Dyson equation allows the efficient computation of the GF of the perturbed system by relating it with the GF of the non-perturbed ‘‘reference’’ medium. For a Hamiltonian H_1 , which relates to a reference Hamiltonian H_0 through the perturbation potential V as $H_1 = H_0 + V$, it follows from the definition (3.8) that their corresponding GF operator obeys $G_0^{-1}(E) = E - H_0$ and $G_1^{-1}(E) = E - (H_0 + V)$, which implies

$$G_1^{-1}(E) = G_0^{-1}(E) - V. \quad (3.14)$$

After a substitution of terms in (3.14), the Dyson equation

$$G_1(E) = G_0(E) + G_0(E)V G_1(E) \quad (3.15)$$

$$= G_0(E) + G_0(E)V G_0(E) + G_0(E)V G_0(E)V G_0(E) + \dots \quad (3.16)$$

is obtained. The last expression enables an interpretation of $G(E)$ in terms of multiple-scattering events. Furthermore, Eq. (3.15) can be rewritten in terms of the scattering matrix $T(E)$ as

$$G_1(E) = G_0(E) + G_0(E) T(E) G_0(E), \quad (3.17)$$

where $T(E) = VG_1V = V + V G_0(E) V + V G_0(E) V G_0(E) V + \dots$

The scattering matrix or T-matrix can be used to express the change in the total single-particle density of states caused by the perturbation potential with respect to the unperturbed system. Substituting Eq. (3.17) in (3.13), the density of states of the perturbed system is given by

$$\begin{aligned}\eta_1(E) &= -\frac{1}{\pi} \text{Im Tr} (G_0(E) + G_0(E) T(E) G_0(E)) \\ &= \eta_0(E) + \delta\eta(E)\end{aligned}\quad (3.18)$$

where

$$\eta_0(E) = -\frac{1}{\pi} \text{Im Tr} (G_0(E)), \quad (3.19)$$

and

$$\begin{aligned}\delta\eta(E) &= -\frac{1}{\pi} \text{Im Tr} (G_0(E) T(E) G_0(E)) \\ &= -\frac{1}{\pi} \text{Im Tr} (G_0(E)^2 T(E))\end{aligned}\quad (3.20)$$

$$= \frac{1}{\pi} \text{Im Tr} \left(\frac{dG_0(E)}{dE} T(E) \right). \quad (3.21)$$

In the last step, the identity $\frac{dG_0(E)}{dE} = -G(E)^2$, which follows from (3.8), has been used.

Moreover, from the definition of $T(E)$, it can be shown that

$$\begin{aligned}\frac{dT(E)}{dE} &= V \frac{dG_1(E)}{dE} V = -VG_1(E)^2V \\ &= -T(E) G_0(E)^2 T(E) = T(E) \frac{dG_0(E)}{dE} T(E)\end{aligned}\quad (3.22)$$

and thus,

$$T(E)^{-1} \frac{dT(E)}{dE} = \frac{dG_0(E)}{dE} T(E). \quad (3.23)$$

Finally, by substitution of (3.23) into (3.21) yields

$$\begin{aligned}\delta\eta(E) &= \frac{1}{\pi} \operatorname{Im} \operatorname{Tr} \left(T(E)^{-1} \frac{dT(E)}{dE} \right) \\ &= \frac{d}{dE} \left(\frac{1}{\pi} \operatorname{Im} \operatorname{Tr} \{ \ell n T(E) \} \right).\end{aligned}\quad (3.24)$$

The integrated density of states can be expressed as

$$N(E) = N_0(E) + \delta N(E), \quad (3.25)$$

where

$$N_0(E) = \int_{-\infty}^E dE' \eta_0(E') \quad (3.26)$$

and

$$\delta N(E) = \frac{1}{\pi} \operatorname{Im} \operatorname{Tr} \{ \ell n T(E) \}. \quad (3.27)$$

Equation (3.27), known as the Lloyd's formula, provides an efficient way to compute the number of states as a function of the energy [108].

When considering problems involving non-interacting particle Hamiltonians, a convenient choice of $G_0(E)$ is the Green's function of a free electron gas given by

$$G_0(\mathbf{r}, \mathbf{r}'; E) = -\frac{1}{4\pi} \frac{\exp[\kappa(|\mathbf{r} - \mathbf{r}'|)]}{|\mathbf{r} - \mathbf{r}'|}, \quad (3.28)$$

where $E = (\hbar^2/2m_e)\kappa^2$. In a spherical potential approximation, the scattering amplitude $t(E)$ (single site T-matrix) of an incoming electron (described by the plane wave 3.28) conserves angular momentum with respect to the potential center (i.e., $t(E)$ is diagonal in angular momentum representation L and the diagonal elements are independent of m). Since the scattering is unitary, the elements $t_l(E)$ can be written in terms of the scattering phase shifts $\delta_l(E)$ as

$$t_l(E) = -\frac{1}{\kappa} \exp(i\delta_l(E)) \sin(\delta_l(E)) \quad (3.29)$$

Generally, most electronic properties can be described considering only a small number of $\delta_l(E)$ shifts (usually $l \leq 3$) [74, 107]. The small basis required for an accurate calculation of the electronic structure constitutes an additional advantage of this method.

In particular, the change in the density of states given by the Lloyd's formula in Eq. (3.27) is reduced to

$$\delta N(E) = \frac{1}{\pi} \sum_l (2l + 1) \delta_l(E). \quad (3.30)$$

Furthermore, the $\delta_l(E)$ are closely related to the Friedel oscillations around impurities, known to result in long-ranged interactions between localized impurities in crystals [107]. Therefore, the perturbational approach the GF-KKR method (together with Eq. 3.30) allow to provide an improved description of the interaction energies between impurities [107, 109–112].

Finally, the full multiple scattering problem of an array of scattering centers located at positions \mathbf{R}_n is solved using the site-centered expression for the GF $G(\mathbf{r} + \mathbf{R}_n, \mathbf{r}' + \mathbf{R}'_n; E)$, which describes the propagation of a wave between the sites \mathbf{R}_n and \mathbf{R}'_n assuming a constant potential in the interstitial region. The solution is obtained by demanding that the incident wave to each scattering center is the sum of the outgoing waves of all other centers. This matching can be achieved only for certain energies which correspond to the eigenvalues of the Hamiltonian (i.e., the allowed electronic states of the system).

*Transition-metal impurities in highly polarizable hosts:
magnetic order and anisotropy*

The strong intra-atomic spin-orbit coupling of $5d$ elements and their potentially significant magnetic polarization when combined with $3d$ -TMs, have consistently shown to enhance the comparatively poor MAE of the pure TM components [62, 113]. In the search of a route to tailor the MAE, a remarkable research activity has been dedicated to a broad variety of $3d$ - $5d$ systems [19, 61, 62, 113, 114]. Still, the precise mechanisms associated with the role of the composition and chemical order on the development of the MAE of TM alloys remain unclear to a large extent. In fact, all the main alloy parameters are expected to affect the magnetic behavior in a non-trivial way. An illustrative example of the importance of chemical composition is the significant dispersion of anisotropy constants found by Tournus *et al.* in dilute assemblies of CoPt small clusters [115]. In their study, a wide distribution of MAEs is attributed to the differences in the chemical order within the clusters. Recently, another important question has been addressed by Brown *et al.* in their theoretical study of the FePt $L1_0$ phase [116]. The study reports a competition between FM and AF ordering between Fe planes. They conclude that the highly anisotropic FM phase observed experimentally is due to the presence of imperfections in the long-range ordering of

the crystal samples or as a result of substitutional disorder. Moreover, their work also reveals the importance of structural distortions.

Fe is traditionally considered an ideal ferromagnet. However, its electronic configuration is not so far from half-band filling, so that transitions between FM and AF order are possible. Let us recall that γ -Fe is AF at low temperatures. Furthermore, Fe is likely to display complex non-collinear magnetic behavior driven by small changes in the local environment [62, 69, 117]. A recent research investigation on the magnetism of Pt-supported Fe nanostructures shows an interesting behavior of the magnetic anisotropy as a function of surface coverage, which results from a complex interplay of spin-orbit coupling, exchange interaction and induced Pt moments [62]. The study revealed a coordination-dependent competition of FM and AF exchange coupling between Fe moments which causes the collapse of the average magnetization with increasing Fe coverage in the low-concentration regime. These examples open new important questions regarding the magnetism of $3d$ - $5d$ compounds: How does the $3d$ magnetic ordering affects the polarization of the $5d$ substrate? What are the consequences of these modifications on the MAE? How does $3d$ concentration affects the magnetic order and the average magnetization? It is the purpose of this Chapter to investigate this interplay and shed some light on the underlying processes governing the magnetic behavior of these systems. Two particularly interesting examples of $3d$ -Pt systems will be addressed, for which a comprehensive analysis on the interplay between local properties, long-ranged magnetic order and MAE has been performed. In the first part, the effects of $3d$ -doping, concentration and magnetic order in a one-dimensional Pt host are examined in some detail. The case of one-dimensional systems is of particular interest, since small local differences are expected to induce large variations of the magnetic response. In the second part of the Chapter we consider the magnetic ordering and MAE of Co atoms on top the Pt(111) surface as a function of coverage and distribution. In both cases, the effects of structural relaxations effects have been analyzed. Emphasis is given to the correlations between the long-ranged magnetic ordering between the $3d$ elements and the polarization of the host and its relevance for the magnetic anisotropy energy of the systems.

4.1 Magnetic order and anisotropy of $3d$ -Pt_{*n*} wires

One-dimensional (1D) systems are expected to display extraordinary large MAEs. The very low atomic coordination allows the development of large spin and orbital

magnetic moments and the high symmetry renders the magnetization to be sensitively dependent on its orientation. The relevance of these systems is backed up by the modern experimental techniques for synthesizing 1D materials. Indeed, 1D structures can be nowadays assembled on surfaces, for example, by direct atomic manipulation using a scanning tunneling microscope (STM) or via self-assembly processes [18, 118, 119]. The singularity of one-dimensionality has been demonstrated in previous theoretical studies. For example, Dorantes-Dávila and Pastor have shown that the enhanced MAE of TM monoatomic chains is largely reduced already for the thinnest ladder structures. In fact, their study shows that the easy axis of magnetization of Fe chains alternates with the transversal size N of the ladder: lying on the axis chain for $N = 1$, changing to the perpendicular plane and back to the chain axis for $N = 2$ and $N = 3$ [64]. Another exceptional example of the determinant effect of low-dimensionality is the colossal MAE reported in Pt monoatomic wires, which results from the intrinsic impossibility of the magnetization to rotate out of the wire axis [120]. In this context, only few theoretical investigations of magnetic anisotropy of one-dimensional alloys are available at present. For example, the study of Wang *et al.* [121] reports very large MAEs in free-standing monoatomic wires, which are significantly reduced upon encapsulation in carbon nanotubes.

In order to shed light on the mechanisms responsible for the magnetic anisotropy of 1D alloys, this study considers ordered $3d$ -Pt alloy monoatomic wires in a free-standing geometry. Pt is a particularly relevant example of $5d$ metal due to its high magnetic polarizability and strong intra-atomic SO coupling, while the free-standing geometry is expected to display the largest low-dimensional effects. The present study concentrates on the interplay and influence of the internal $3d$ magnetic ordering on the local magnetic properties and the development of the overall MAE. In the first part, the role of the $3d$ band filling is investigated by varying systematically the alloying element across the $3d$ series. Considering the possible magnetic arrangements between the $3d$ components within the system, we analyze the role of the local properties on the anisotropic behavior of equiatomic $3d$ -Pt wires. In the second part, we focus on the particular case of ordered FePt $_n$ wires and concentrate on the relative magnetic order between Fe dopants as a function of the chemical composition and its influence on the long-range magnetic behavior.

4.1.1 Computational details

Following the previous perspective, self-consistent electronic calculations have been performed using the Vienna *ab initio* simulation package (VASP) described in Chapter 3.1. Exchange and correlation effects were treated within the Perdew-Wang generalized-gradient approximation (GGA) [85].

The infinite wires are constructed in a rectangular supercell of length $a = 12 \text{ \AA}$ in the directions perpendicular to the wire. This size ensures that the interaction of the wire with its neighboring images is negligible. Moreover, both ferromagnetic (FM) and antiferromagnetic (AF) alignments of the magnetic moments of the $3d$ atoms within the supercell have been considered. This prescription, together with the freedom for the alignment of the $5d$ moments, allows to account for FM and AF superexchange-like couplings between the $3d$ moments mediated by the intermediate $5d$ atoms and vice versa. To explore the effects of structural relaxation on the investigated properties, we performed self-consistent optimizations of the atomic positions using the conjugate gradient and quasi-Newtonian methods [94]. The optimized structure is found by requiring that the calculated force acting on each atom is less than 0.001 eV/\AA . The k -point meshes $n_k = 1 \times 1 \times 91$ and $n_k = 1 \times 1 \times 41$ have been used to evaluate all integral quantities within the Brillouin zone, together with the Gaussian smearing method with a small final standard deviation $\sigma = 0.02 \text{ eV}$ applied for the determination of the partial occupancies.

The calculation of the MAE, which involves very small energy differences (of the order of a few meVs/atom) requires the use of large plane-wave basis and accurate numerical convergence in order to be reliable. Accordingly, an energy cut-off of 450 eV for the plane-wave basis set has been used. The criterion of total energy convergence was assumed when the difference between two self-consistent cycles was smaller than 10^{-7} eV . The MAE is calculated as the difference in the total energy corresponding to independent self-consistent calculations where the magnetization of the system lies along and perpendicular to the wire axis. A pre-converged scalar relativistic solution, being rotationally invariant, was used to initialize both calculations. Notice that the self-consistently determined magnetization direction is, in principle, allowed to relax and rotate to its minimum energy axis. However, due to the symmetry of the wires, the total energy is stationary at the considered directions. While solutions involving non-collinear magnetic arrangements might exist, they are avoided by this prescription of initialization and by the finite size of the supercell.

4.1.2 Magnetic order and MAE in $3d$ -Pt wires

In the following, we consider the case of binary ordered $3d$ -Pt alloy wires having 50% concentration of each component. Such composition, which maximizes the $3d$ - $5d$ hybridization, will provide us with a local perspective to the $3d$ - $5d$ proximity effects.

The magnetic anisotropy energy $\Delta E = E_x - E_z$, where E_δ refers to the total energy per atom when the magnetization lies along the axis δ , has been calculated for $3d$ -Pt wires varying the $3d$ component. The cartesian z axis is taken along the axis of the wires. Results for ΔE corresponding to a FM and an AF ordering between the moments of the $3d$ atoms are shown in Fig. 4.1 for wires at their equilibrium interatomic distances. The ground-state (GS) magnetic order (i.e., FM or AF) is identified with solid symbols. Here, one observes strong even-odd oscillations of ΔE as a function of the $3d$ dopant. Significantly large values of the MAE ($\Delta E \simeq 20\text{meV}$) are obtained in the case of NiPt and VPt wires, while relatively small values are found, for instance, in CrPt and MnPt. Furthermore, one observes that, in general, the values of ΔE are larger for a FM ordering between the $3d$ elements. In this sense, the dependence of the MAE on the $3d$ doping element is not easily generalizable. However, it is interesting to notice that the calculated MAE of CoPt wires is quantitatively comparable to available experimental results of Co monoatomic chains deposited on a Pt substrate [118]. This indicates that the MAE obtained for free-standing wires can provide useful insights on more complex situations, provided that the local environments are comparable, for instance, similar low coordination numbers and type of neighbors.

In order to provide a local perspective to the MAE Table 4.I shows the local spin moments μ_δ and orbital moments L_δ calculated inside the Wigner-Seitz spheres at the $3d$ and $5d$ sites of the wires. For TiPt, VPt and CrPt in the FM configuration, we find that the $3d$ and Pt moments are antiparallel to each other, while they are parallel in the case of ferromagnetic CoPt and NiPt [57]. As indicated by the full symbols in Fig. 4.1, the later configurations correspond to the ground-state magnetic order of these wires. It is important to notice that in the case of an AF alignment between the $3d$ elements, the magnetic moment at the intermediate Pt sites is precluded by the antisymmetry of the potential. Interestingly, such AF configuration is found as the ground-state of FePt and MnPt wires. In the case of FePt wires, the large reduction of charge at the $3d$ orbitals, caused by a significant charge transfer of about 0.5 electrons to the Pt $5d$ orbitals, brings Fe closer to half d -band filling and possibly favors the

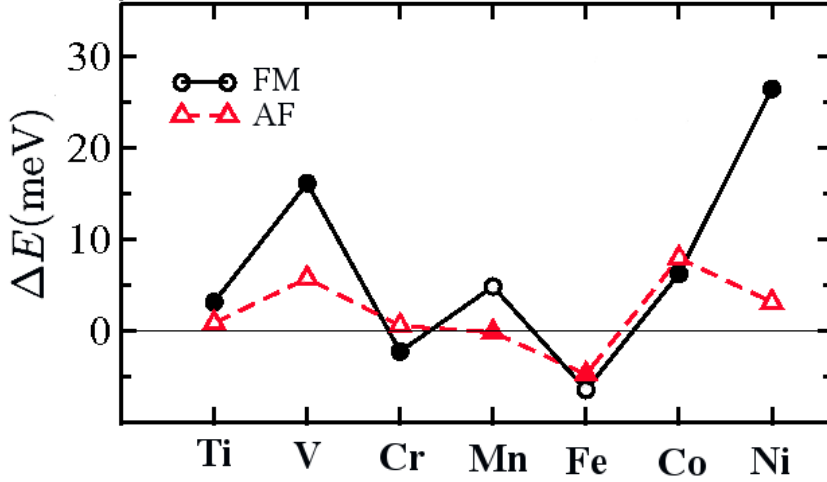


Figure 4.1: Calculated MAE $\Delta E = E_x - E_z$ of 3d-TM wires at their equilibrium interatomic distance. Positive (negative) values of ΔE correspond to an easy axis along (perpendicular to) the wire axis. Results are given in meV/atom for FM (circles) and AF (triangles) ordering between the 3d moments. Full symbols indicate the ground-state magnetic order (See Ref. [57]).

observed AF order. This GS magnetic order is, moreover, not affected by moderate variations of the interatomic distances around the equilibrium values.

From a local perspective, the main contribution to the MAE is expected to arise from the change in the intra-atomic SO energies (ΔE_{SO}) which, in the limit of saturated spin moments, is proportional to the anisotropy of the local orbital moments $\Delta L = L_x - L_z$. A simple approximation of ΔE_{SO} for alloys is given by

$$\Delta E_{SO} = \frac{1}{N} \sum_{\alpha} \Delta E_{\alpha} \simeq \sum_{\alpha} \left(\pm \frac{\xi_{\alpha}}{2} \right) \Delta L_{\alpha}, \quad (4.1)$$

where ξ_{α} and ΔL_{α} refer to the SO coupling constant and anisotropy of the local orbital moments ΔL at the atom α . This definition extends the relation derived by Bruno for homogeneous systems. The positive (negative) sign applies to Ti-Mn (Fe-Ni and Pt) [57]. Notice that Eq. (4.1) neglects the spin-flip off-diagonal terms of the SO coupling, as well as the energy contributions arising from the anisotropy of the kinetic and Coulomb energies. The later terms are not negligible if important redistributions of spin-polarized density occur upon a rotation of the magnetization. Such redistributions are found in strongly hybridized systems which exhibit an anisotropy of the spin moments [57]. According to Eq. (4.1), one can qualitatively understand the behavior of ΔE by looking at the changes in the local spin and orbital moments

Table 4.I: Local spin and orbital moments in 3d-Pt wires at their equilibrium interatomic distances: μ_z and L_z correspond to an in-line orientation of the magnetization, while μ_x and L_x correspond to a perpendicular direction. Results are given in μ_B for a ferromagnetic (FM) and an antiferromagnetic (AF) arrangement between the 3d moments. The corresponding values of the MAE $\Delta E = E_x - E_z$ are given in meV/atom (See Ref. [57]).

FM	Ti	V	Cr	Mn	Fe	Co	Ni
Pt μ_z/μ_x	-0.15/-0.14	-0.24/-0.22	-0.18/-0.20	0.32/0.23	0.66/0.64	0.64/0.66	0.60/0.47
Pt L_z/L_x	-0.11/-0.08	-0.21/-0.12	-0.06/-0.20	0.01/-0.12	0.28/0.23	0.25/0.28	0.38/0.16
3d μ_z/μ_x	1.51/1.51	2.62/2.61	3.63/3.63	4.27/4.26	3.45/3.45	2.27/2.32	1.00/0.96
3d L_z/L_x	-0.30/0.06	-0.63/0.08	-0.04/0.14	-0.10/0.16	-0.16/0.21	0.47/0.15	0.44/0.04
ΔE	3.1	16.1	-2.3	4.8	-6.5	6.2	26.4
AF							
3d μ_z/μ_x	0.95/0.94	2.06/2.05	3.36/3.38	4.02/4.02	3.26/3.26	2.10/2.09	0.47/0.00
3d L_z/L_x	-0.20/0.04	-0.49/0.17	-0.23/0.50	-0.07/0.13	0.12/0.20	0.74/-0.16	0.30/0.00
ΔE	0.8	5.7	0.5	-0.2	-4.8	7.9	3.1

for the different orientations of the magnetization. For instance, relatively large spin and orbital moments $\mu \simeq 0.6\mu_B$ and $L \simeq 0.25\mu_B$ are induced at the Pt atoms in FePt and CoPt FM wires. However, these values are almost independent of the orientation of the magnetization and, therefore, the MAE remains relatively small (See Table 4.I).

Consistent with that, the large MAE found in the FM arrangement of NiPt is in agreement with the strong dependence of the local moments of both Ni and Pt on the directions of the magnetization. In addition, the local contributions to ΔE_{SO} of Ni and Pt have the same sign and therefore favor the same easy axis. As a consequence, an exceptionally large value of ΔE is found for this composition. In contrast with this result is the example of CoPt wires, where ΔE_{Co} and ΔE_{Pt} are competing and the resulting MAE is rather low. It is interesting to analyze the role of the magnetic polarization of the Pt atoms in this context. For example, in the case of NiPt, one observes a remarkable difference in the values of ΔE corresponding to a FM and an AF ordering between the 3d moments. The strong enhancement of ΔE for the FM case can be interpreted straightforwardly in terms of the additional E_{SO} contribution of the Pt atoms, since they are magnetically polarized only in the FM configuration.

One observes that the spin moments of Pt are systematically larger for alloying elements at the end of the 3d series. Similar is the case of the induced orbital moments, which provide an important contribution to the total magnetization and be-

come determinant for the MAE. Indeed, the easy-axis of magnetization corresponds in general to the direction yielding the maximum total orbital moment. In the case of FePt and MnPt wires the spin and orbital moments of Pt vanish and the anisotropy is determined only by the $3d$ component. In this context, it seems questionable to consider that the MAE originates essentially at the $5d$ atoms. This analysis shows that none of the local contributions ΔE_α alone accounts for a complete description of the MAE of the alloyed wires.

Furthermore, the coupling between the local spin and orbital moments follows the 3_{rd} Hund's rule in all ground-state configurations. This means, that the spin and orbital moments are antiparallel (parallel) for $3d$ elements below (above) the half-band filling. However, notice that the orbital moment of the $3d$ atoms aligns antiparallel to the spin moment for an in-line magnetization of the FM FePt wire and for a perpendicular magnetization in AF CoPt wires. This feature indicates that, in these $3d$ atoms, more complex hybridization effects dominate over the spin SO interactions alone, which would favor a parallel alignment in accordance with Hund's third rule.

From these observations, one concludes that not only the $5d$ element is responsible of the anisotropic behavior of the alloyed wires, but also, a strong contribution of the $3d$ element to the development of the MAE is involved. Moreover, the local properties and consequently the MAE suffer strong changes as a consequence of the different internal magnetic order between the $3d$ elements (i.e., FM or AF). From this local perspective, it would be desirable to investigate the interplay between chemical order, magnetic ordering and MAE.

4.1.3 Magnetic order and anisotropy of FePt_{*n*} wires: 3*d*-concentration dependence

In the context of Sec. 4.1.2, it is worthwhile to investigate the effect of the concentration of the $3d$ element on the magnetic behavior of the Pt alloyed wires. In particular, it would be interesting to analyze how the concentration of $3d$ -dopants and its magnetic order affects, for example, the magnetic polarization of the Pt wire and the resulting consequences on the development of the MAE. Besides the fundamental differences in the electronic structure related to the chemical composition, strong modifications should also be expected in the equilibrium atomic positions when varying the concentration of the $3d$ element. The bond length between $3d$ neighboring atoms is in general shorter than that of alloyed $3d$ - $5d$ bonds, while it is larger for $5d$ - $5d$ bonds.

Thus, the resulting structural relaxations can lead to a reduction of the translational symmetry of the wires (e.g., dimerization) which could have important consequences on the electronic and magnetic properties (e.g., magnetic order and MAE). In this context, a systematic study of the magnetic properties as a function of the $3d/5d$ composition which accounts for the diversity of possible internal magnetic orders seems essential. The case of FePt alloys is of special interest. In the previous section, an antiparallel arrangement between Fe magnetic moments is found as the ground-state of ordered FePt wires. Such configuration precludes the magnetic polarization of the Pt atoms. As a consequence, the Pt atoms do not contribute to the resulting MAE which is, hence, rather low. The AF order in the FePt wires is surprising since Fe is a well known ferromagnetic material. Nevertheless, the AF coupling between Fe moments in ordered FePt wires is consistent with the AF ordering between Fe planes of the ordered L1₀ phase of FePt reported by Brown *et al.* [116]. In the later case, the AF phase has been found to be extremely sensitive to imperfections in the long-range chemical order and substitutional disorder. Structural modifications have been also addressed in this context. These results suggest the existence of a super-exchange-like interaction between Fe components, mediated by the intermediate Pt atoms. This could open the possibility of tuning the internal magnetic order and the MAE of the system by varying the chemical composition. Furthermore, one also expects that FePt wires could present modifications of the Fe coupling as a function of the chemical order. These observations motivate the present study of FePt nanowires in the low Fe-concentration regime, in which we specifically analyze the interplay between the composition, magnetic order and magnetic anisotropy. For this purpose, we consider ordered FePt $_n$ free-standing wires ($1 \leq n \leq 4$) having a fixed interatomic distance of 2.4 Å, which corresponds roughly to the equilibrium value of the pure Pt monoatomic wire [120]. Self-consistent calculations are performed in the scalar and fully relativistic approximation schemes implemented in the Vienna *ab initio* simulation package (See Sec. 3.1). The comparison between both results allows us to quantify the effects of the SO interaction on the electronic and magnetic properties. As in the case of the $3d$ -Pt wires studied in the Sec. 4.1.2, the FM and AF coupling between FePt $_n$ unit cells has been considered. To be conclusive it is essential that the orientation and strength of the spin and orbital moments of the Pt atoms are not restricted by any prescription in the input of the calculations. Therefore, we do not assume any a priori magnetization of the Pt atoms. Only the spin moments of the Fe atoms are assumed to be align in a parallel or antiparallel configuration.

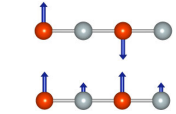
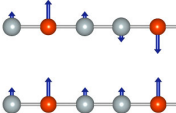
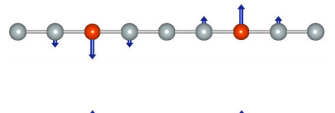
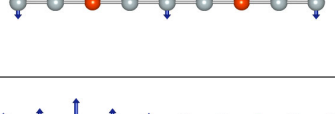
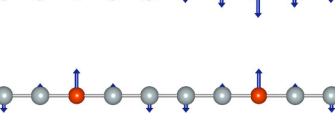
Structure	μ_{Fe}	μ_{Pt}	$\bar{\mu}_T$	E_{xc}
	3.38	0.0	0.0	34.17
	3.51	0.69	2.1	
	3.46	0.39	0.0	40.11
	3.47	0.57	1.54	
	3.36	0.35	0.0	-12.16
	3.38	0.13	0.83	
	3.37	0.40	0.0	-40.88
	3.39	0.01	0.40	
		-0.33		
		-0.72		

Table 4.II: Calculated total magnetic moment per atom $\bar{\mu}_T$ and local spin moments μ_{Fe} and μ_{Pt} in ordered FePt_n wires having a fixed interatomic distance of 2.4 Å. Results are given in μ_B for AF and FM ordering between Fe moments as illustrated in the figures. Values for the central Pt sites are displayed in a second line. Energy differences between the AF and FM configurations $E_{\text{xc}} = E_{\text{FM}} - E_{\text{AF}}$ are given in meV/atom. A negative (positive) value of E_{xc} implies a FM (AF) ground state.

Magnetic coupling and local properties

We begin the discussion with an analysis of the local properties. In Table 4.II, the results of scalar-relativistic calculations for FePt_n wires ($1 \leq n \leq 4$) are shown. The figures illustrate the chemical and magnetic order within the wires with arrows representing the calculated local spin moments μ_{Fe} and μ_{Pt} given in the table. The total magnetization per atom $\bar{\mu}_T$ and the total energy difference E_{xc} between FM and AF alignments between FePt_n units are also shown.

As discussed in the previous section, a favorable AF coupling between the Fe moments is found for the FePt wire. The FM arrangement is about 35 meV/atom above the AF solution. For the AF configuration, the magnetic polarization of Pt is

quenched by the antisymmetry of the potential at these sites. In contrast, for a FM arrangement, the Pt atoms develop important magnetic moments of nearly $0.7\mu_B$. In addition, μ_{Fe} is about $0.13\mu_B$ larger in the FM case than in the AF one. One can thus conclude that the energy gained due to magnetic polarization in the FM configuration ($\bar{\mu}_T \simeq 2.0\mu_B/\text{at}$) is in competition with an energetically favorable AF coupling between Fe second nearest neighbors (NNs). In a similar way, for the case of ordered FePt₂ wires, the AF order between the Fe atoms in nearby cells is about 40meV/atom more stable than the FM order. For this composition the Fe atoms occupy third NNs positions which allows the magnetic polarization of the intermediate Pt atoms in both FM and AF configurations. The value of $\mu_{\text{Pt}} \simeq 0.4\mu_B$ found for the AF arrangement can be compared with $\mu_{\text{Pt}} \simeq 0.6\mu_B$ found for the FM case. These spin moments are parallel to those of the corresponding Fe NN. Notice, however, that this Fe-Pt coupling results in an antiparallel alignment between NN Pt atoms in the AF arrangement of FePt₂. As it will be discussed below, this antiferromagnetic coupling of Pt NNs is likely responsible for the small values of μ_{Pt} found in this configuration. Moreover, it is interesting to notice that, already for this chemical composition, the difference in the local spin moments of the Fe atoms for the FM and AF configurations is negligible. One can say that the two intermediate Pt atoms are sufficient to avoid a direct electronic coupling between the Fe atoms.

For the ordered FePt₃ wire, the FM coupling between Fe moments at adjacent cells is 12 meV/atom more stable than the AF arrangement. At this concentration three Pt atoms separate the Fe atoms. As in the case of the FePt wire, the symmetry of an AF coupling leads to the suppression of μ_{Pt} at the central Pt site. Nevertheless, spin moments $\mu_{\text{Pt}} = 0.35\mu_B$ parallel to their NN Fe are induced at the adjacent Pt atoms. Smaller values ($\mu_{\text{Pt}} = 0.13\mu_B$) are found at these positions for a FM alignment of FePt₃. However, a fairly large spin moment $\mu_{\text{Pt}} = -0.33\mu_B$ is found at the central Pt atom. Notice that this Pt moment is aligned antiparallel to the adjacent Pt and to the Fe moments. Consequently, the resulting magnetic configuration involves two AF couplings between Pt NNs per FePt₃ unit. Once again, the smaller value of μ_{Pt} found at the Pt sites in contact with Fe is probably related to this antiparallel alignment. It is interesting to notice that the lowest energy configuration (i.e., FM coupling between FePt₃ units) corresponds also to an AF arrangement between second NN Fe and Pt. Thus, despite the FM coupling between Fe moments, this configuration still shows a strong tendency to the AF short-range order. Thus, at low Fe concentration, the FM coupling of Fe enables not only the magnetic polarization but also the antiparallel alignment of the magnetic moment of the central Pt atom. Moreover, notice that

the magnetic moments of the adjacent Pt atoms are still parallel to those of Fe, but its strength is strongly decreased ($\mu_{\text{Pt}} = 0.13\mu_B$) compared to the case of FM FePt ($\mu_{\text{Pt}} = 0.69\mu_B$) and FePt₂ ($\mu_{\text{Pt}} = 0.57\mu_B$). A similar arrangement is found for ordered FePt₄ wires. The FM coupling between Fe moments is established as the ground-state with 41 meV/atom lower energy than the AF order. The two central Pt atoms couple ferromagnetically to each other and develop large magnetic moments $\mu_{\text{Pt}} \simeq -0.7\mu_B$. The magnetization of the adjacent Pt atoms, being aligned to the NN Fe moments, is quenched to only $0.01\mu_B$. Thus, the total magnetization per atom is reduced to only $\bar{\mu}_T = 0.4\mu_B$.

As a general observation, one can conclude that a purely FM configuration, which would maximize the total magnetization $\bar{\mu}_T$, is not favorable in FePt alloy wires at the studied limit of low Fe concentration. The maximum total magnetic moment per Fe atom is found for the FM configuration of FePt₂. However, this configuration does not correspond to the ground-state of the wire. In the cases of FePt₃ and FePt₄, where the ferromagnetic coupling between Fe dopants is favored, the large antiferromagnetic moments of the central Pt atoms strongly reduce the total magnetization. Our results are in good agreement with those obtained by Bezerra-Neto *et al.* for deposited FePt_n chains on Pt(111) [66].

The local properties and the differences regarding the magnetic order can be analyzed from the point of view of the local density of states (LDOS). In Fig. 4.2 the LDOS at the Fe and Pt sites of the FePt and FePt₂ wires is shown. Both FM and AF arrangements between FePt_n units are considered. One observes strongly localized Fe states in both configurations of the FePt wire. In the FM case, the magnetic moment is completely saturated with the LDOS showing a single peak of majority-spin states at about 3.7 eV below the Fermi energy ε_F . A similar peak is found for the AF arrangement, presenting two additional peaks at slightly higher energies and a minority-spin orbital lying at ε_F . The LDOS at the Pt site corresponds, for the AF configuration, to a non spin-polarized Pt having broader bands between 0.5 eV and 2.0 eV below ε_F . At similar energies, the Pt atoms in the FM configuration show majority-spin and minority-spin orbitals with a relatively large exchange splitting of about 0.5 eV. The splitting is in accordance with the large values of μ_{Pt} found for this arrangement. In the case of FePt₂, the LDOS at the Fe sites is almost identical for both configurations. A single peak is found, as in the case of FePt, at about 3.5 eV below ε_F while the minority-states orbitals lie well above ε_F . This features agree with the saturated and similar values of the magnetic moments found in both configurations of this composition. The LDOS of Pt atoms is, in this case, spin-polarized for both

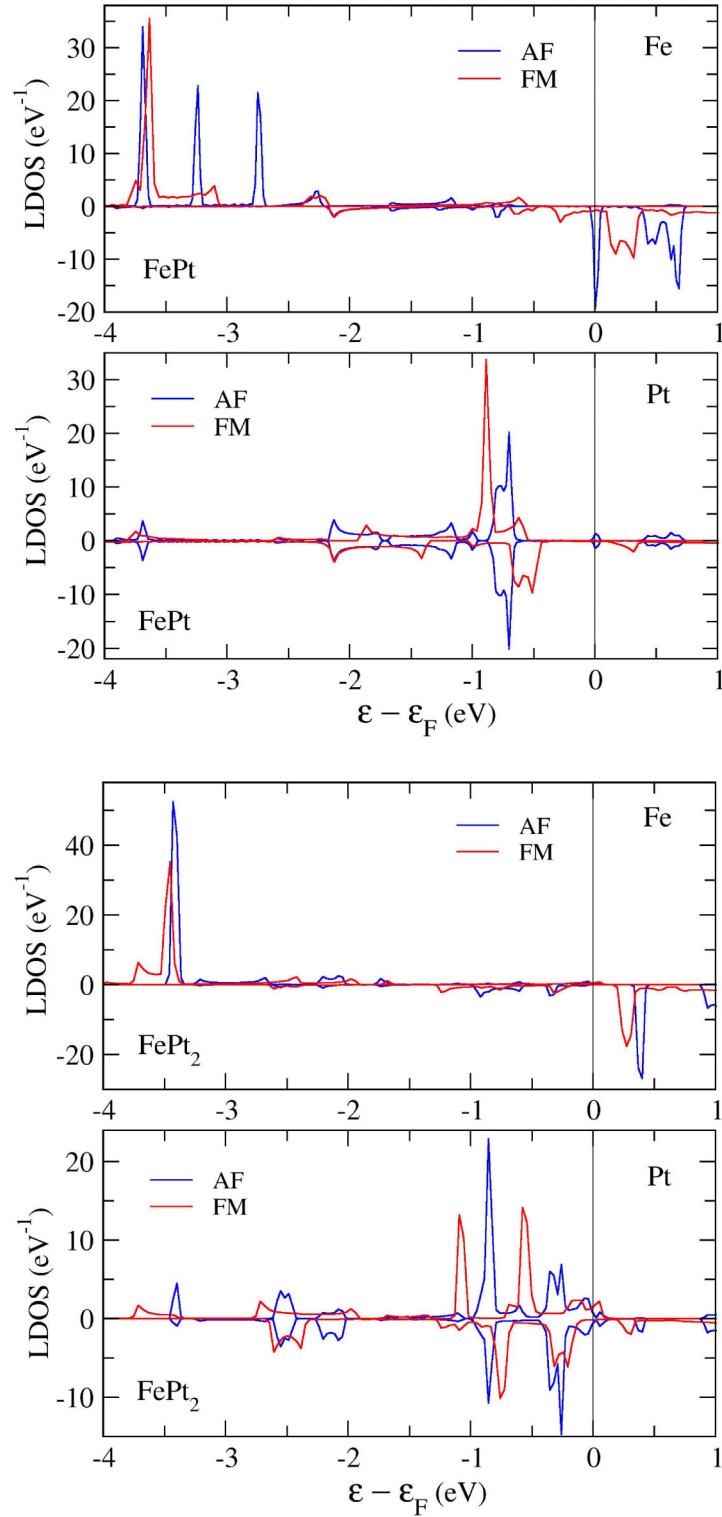


Figure 4.2: Local density of d -states (d -LDOS) at the Fe and Pt sites of FePt and FePt₂ wires. Curves are shown for the AF and FM ordering between Fe moments.

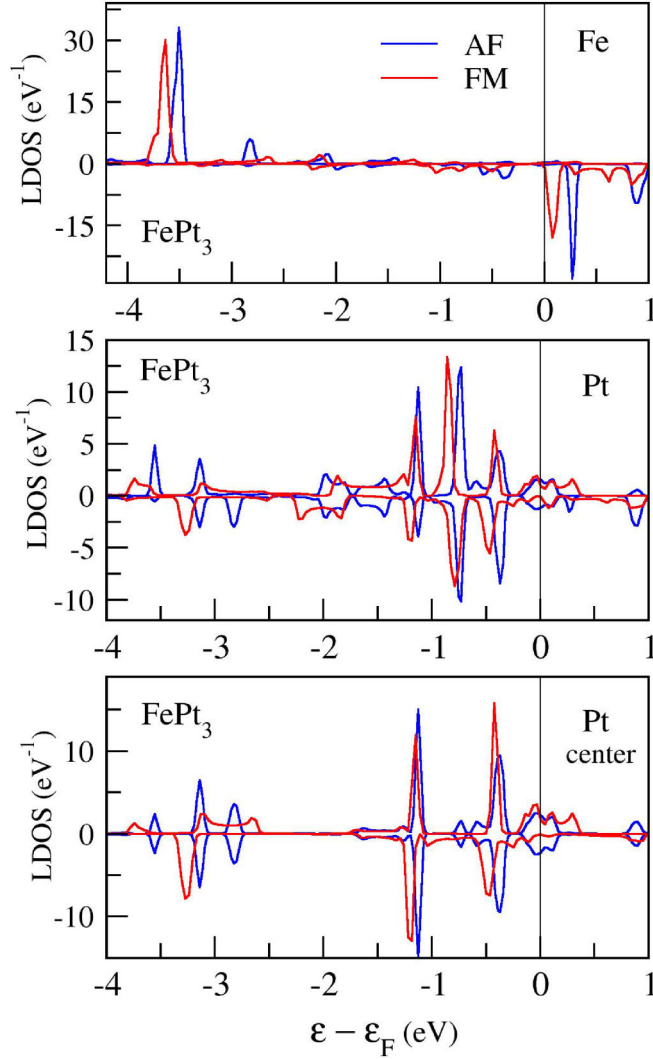


Figure 4.3: Local density of d -states (d -LDOS) at the Fe and Pt sites of a FePt_3 wire. Curves are shown for the AF and FM ordering between Fe moments.

FM and AF arrangements. The exchange splitting is, however, insignificant in the AF configuration. In fact, the magnetic moment of Pt is mainly a result of the spin asymmetry of the majority and minority bands. Notice that, in addition, a second peak emerges in the LDOS of Pt for FePt_2 which is absent in the FePt wire. For the sake of comparison, Fig. 4.3 shows the LDOS of the FePt_3 wire. At the Fe sites, the LDOS remains essentially the same as in FePt_2 , while for the adjacent Pt atoms a third peak appears. The exchange splitting is also reduced, as compared the one found in FePt_2 . This is consistent with the observed reduction of μ_{Pt} . Finally, the LDOS at the central Pt atom is, as in the case of FePt , non-spin polarized for the AF

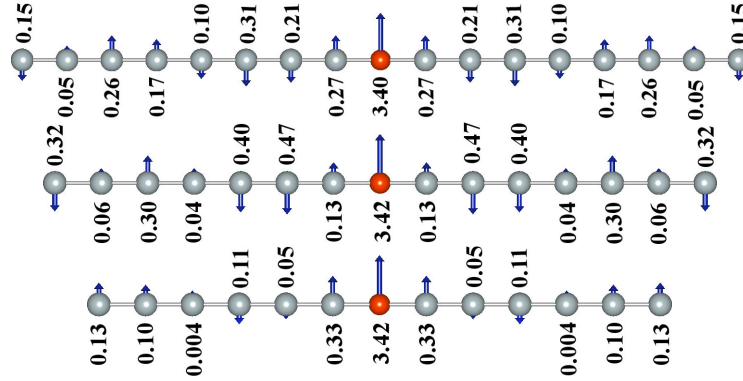


Figure 4.4: Illustration of the internal magnetic order and local spin moments in μ_B of ordered FePt $_{16}$, FePt $_{14}$ and FePt $_{12}$ wires.

configuration, while for the FM case it displays a shifting of the majority and minority spin bands which is opposite to that of Fe. This is correlated with the antiparallel alignment of the respective local moments.

In order to analyze in further detail the overall magnetic behavior of FePt $_n$ wires, Fig. 4.4 illustrates the internal magnetic order in FePt $_{12}$, FePt $_{14}$ and FePt $_{16}$ wires having a FM alignment between Fe impurities. Here, one observes that the alignment of the Pt moments with respect to the Fe moments switches periodically from FM to AF as a function of the distance to the Fe atom. The oscillation period is about five interatomic distances ($\lambda \approx 12\text{\AA}$). Still, important differences in the local moments μ_{Pt} are observed for different numbers of Pt atoms n . In particular, the values of μ_{Pt} for Pt atoms located at the same distance respect to the Fe impurity differ for each composition (see Fig. 4.4). For instance, the Pt atom located at the second NN position of Fe couples antiferromagnetically with the impurity in all cases. However, its magnetic moment varies from $0.05\mu_B$ in FePt $_{14}$ up to $0.47\mu_B$ in FePt $_{16}$. Therefore, despite the similarity of the systems and the general magnetic arrangement, the total magnetization per atom $\bar{\mu}_T$ is largely affected by the composition. Additionally, the same trend of internal magnetic couplings has been observed in finite systems. This behavior suggests the presence of Friedel-like oscillations caused by the quantum confinement of electrons which are scattered by the Fe impurities. The electronic charge inside the Wigner-Seitz (WS) spheres of the different atoms show oscillations of the local charge density along the Pt sites. In fact, about 0.2 additional electrons are found inside the WS volume of a Pt site within FePt $_n$ wires as compared to the case of a pure Pt wire. This difference can be associated with a greater localization of the electrons near the nuclei. Furthermore, the density oscillations are caused by

the scattering of delocalized electrons at the impurity potentials. In this sense, the spin-polarization of the impurity, showing saturated values of the magnetic moment in the present case of Fe, causes a strong spin dependence on the electron scattering which results in oscillations of the magnetization density.

Moreover, the perturbation caused by the Fe defects is not restricted to energies close to the Fermi level. The electronic localization and the hybridizations between atomic orbitals are expected to modify the energy levels well below ε_F . Fig. 4.5 shows the local density of d -states at the different Pt sites of an FePt₁₆ wire (see Fig. 4.4 top). The corresponding LDOS of a Pt atom within a pure Pt wire is shown for comparison. At all Pt sites, one observes important changes in the LDOS at energies far below the Fermi level. Such modifications do not weaken at the most distant sites from the impurity. Although the band width is not significantly changed, the majority- and minority-spin bands are affected in different ways resulting in the formation of local magnetic moments. Furthermore, a relatively low density of states of Pt is found at about 3.6eV below ε_F , which corresponds to the energy of the majority-spin band of the Fe impurity. This feature is an indicative of the strong localization of the Fe d -states which show only a small hybridization with the neighboring Pt atoms. Instead, the largest hybridization takes place between the delocalized s and p orbitals near the Fermi level.

The internal magnetic order of the wires as well as the variations in the values of μ_{Pt} can also be described from a local point of view as a competition between ferromagnetic NN and antiferromagnetic second-NN interactions. Such a situation can be phenomenologically characterized within a classical Heisenberg Hamiltonian of the form

$$H = \sum_i H_i = \sum_i [-J_0 \mathbf{S}_i \cdot \mathbf{S}_{i+1} + J_1 \mathbf{S}_i \cdot \mathbf{S}_{i+2}] \quad (4.2)$$

where \mathbf{S}_i represents the local magnetic moment of the atom i . In general, the lowest energy configuration of Eq. (4.2) corresponds to a non-collinear (spin-wave-like) magnetic arrangement of the local moments \mathbf{S}_i in which the magnetization rotates along the wire axis. However, this behavior is not expected in the case of free-standing Pt wires given its extraordinarily large magnetic anisotropy and strong tendency to the non-magnetic state [120]. Instead, one could interpret the variations of the internal vector product of Eq. (4.2) as a variation on the magnitude of \mathbf{S}_i . In this sense, the energy is reduced by the decrease of the local moments rather than by the rotation of the magnetization.

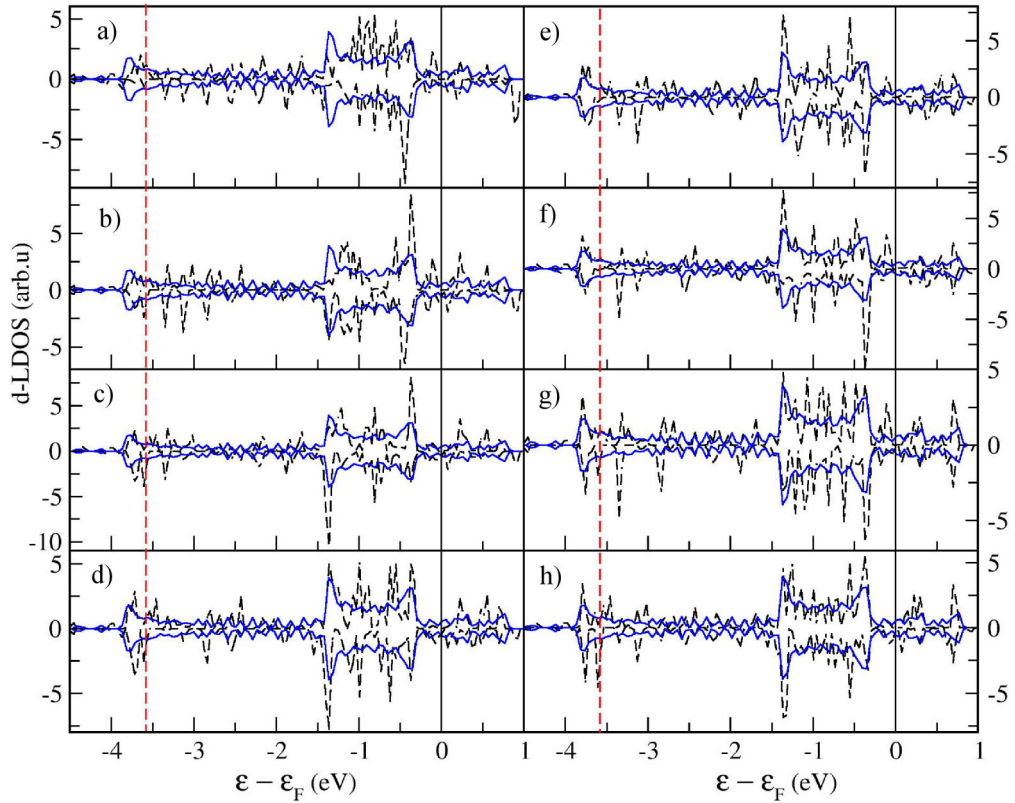


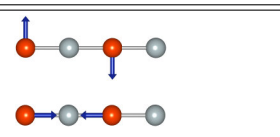
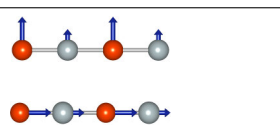
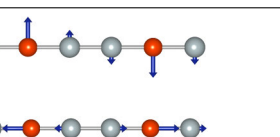
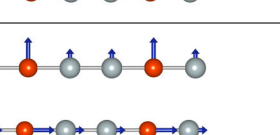
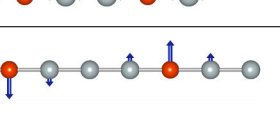
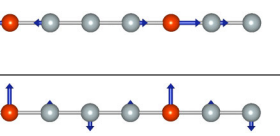
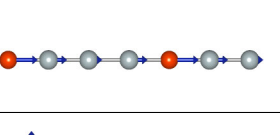
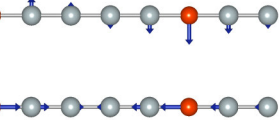
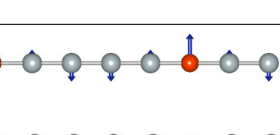
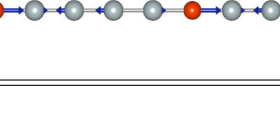


Figure 4.5: Local density of d -states (d -LDOS) at the Pt sites of an FePt $_{16}$ wire (see Fig. 4.4 top). Subfigures (a)-(h) correspond to Pt positions ordered by increasing distance with respect to the Fe atom. The dashed vertical line indicates the location of the majority-spin band of the Fe impurity. The d -LDOS of a Pt atom within a pure Pt wire (full lines) is shown for comparison.

From the previous observations and analysis, the magnetic arrangement between Fe impurities is also expected to oscillate as a function of the distance. In this sense, the coupling would depend on the concentration as well as on the chemical order. Particularly, at the limit of low Fe concentration, the magnetic coupling between the dopants is expected to follow the oscillating polarization of the Pt wire.

Magnetic anisotropy

In order to investigate the anisotropic properties and orbital magnetism of the wires calculations which take into account the spin-orbit coupling (SOC) contribution to the energy have been performed. The results for MAE ΔE and local orbital moments L_α of FePt $_n$ ($1 \leq n \leq 4$) wires are presented in Table 4.III. Values are shown for a parallel and a perpendicular orientation of the magnetization with respect to the

Table 4.III: Calculated local spin and orbital moments μ_α and L_α ($\alpha = \text{Fe, Pt}$) and total magnetic moment per atom $\bar{\mu}_T$ in ordered FePt_n wires having a fixed interatomic distance of 2.4 Å. Values for the central Pt sites are displayed in a second row. Results are given in μ_B for an AF and a FM ordering between Fe moments when the magnetization is oriented along and perpendicular to the wire axis as illustrated in the inset figures. The anisotropy energy $\Delta E = E_x - E_z$ is also given in meV/atom. Negative (positive) values of ΔE correspond to an in-line (perpendicular) easy-axis of magnetization.

Structure	μ_{Fe}	μ_{Pt}	L_{Fe}	L_{Pt}	$\bar{\mu}_T$	ΔE
	3.37	0.0	0.21	0.0	0.0	7.34
	3.36	0.0	0.07	0.0	0.0	
	3.48	0.63	0.24	0.27	2.31	7.09
	3.48	0.65	-0.20	0.33	2.13	
	3.42	0.33	0.21	0.17	0.0	-3.64
	3.40	0.32	-0.43	0.15	0.0	
	3.40	0.40	0.25	0.12	1.56	-15.75
	3.45	0.53	-0.46	0.25	1.52	
	3.36	0.33	0.24	0.12	0.0	-3.87
	3.39	0.44	-0.39	0.24	0.0	
	3.34	0.12	0.24	-0.07	0.87	-8.95
	3.41	-0.20	-0.48	-0.01	1.11	
	3.40	0.37	0.27	0.12	0.0	5.81
	3.40	0.12	-0.34	0.08	0.0	
	3.36	0.03	0.22	-0.02	0.40	21.07
	3.39	-0.57	-0.35	-0.24	0.39	
	3.39	0.11	-0.35	0.06	0.39	
		-0.47		-0.25		

wire axis. The MAE is computed as the difference in the total energy of the system corresponding to these two orientations of the magnetization. Negative (positive) values of ΔE correspond to an in-line (perpendicular) easy magnetization axis.

In Table 4.III, one observes that the behavior of the internal magnetic order and local spin moments found in Sec. 4.1.3 is preserved after considering the relativistic effects. This result is, in fact, not evident. As we will see, the energy differences between the FM and AF arrangements are comparable with those between the easy and hard axes of magnetization of a system with the same internal magnetic order. The values of μ_{Fe} and μ_{Pt} are, nevertheless, not significantly modified by the SOC contribution. The FM configuration of the equiatomic FePt wire lies about 30 meV/atom higher in energy than the AF ground state. For both magnetic configurations (i.e., FM and AF) a perpendicular magnetic orientation is energetically favored with a similar value of $\Delta E \simeq 7$ meV/atom. In addition, large orbital moments are induced at all atomic sites which are strongly directional dependent. Notice, in particular, the negative value of L_{Fe} for an in-axis magnetic orientation of the FM configuration. In this case, L_{Fe} is in fact antiparallel to the local spin moment μ_{Fe} . This feature, which represents a violation of the atomic third Hund's rule, appears in all considered compositions of the FePt_n ($1 \leq n \leq 4$) wires and will be discussed later in the text.

The AF configuration of FePt_2 is nearly 20 meV/atom lower in energy than the FM state, with both configurations having an in-line easy axis of magnetization. The MAE of the FM state is, however, about four times larger than that of the AF configuration. This difference can be understood in terms of Eq. (4.1) from the variations in the local spin and orbital moments of the Pt atoms. Notice that the violation of the third Hund's rule at the Fe atoms appears for the easy axis magnetization of FePt_2 . In fact, the local orbital moment $L_{\text{Fe}} \approx -0.45\mu_B$ is antiparallel to the spin moment μ_{Fe} for an in-line magnetization of both FM and AF configurations, and thus, in the magnetic ground state of the wire.

Large differences in μ_{Pt} and L_{Pt} are also present in FePt_3 . However, the MAE remains relatively small ($\Delta E < 10$ meV/atom) for both FM and AF configurations. In the FM case, an in-line orientation of the magnetization leads to a ferromagnetic coupling between all the local moments, including the central Pt site (see inset in Table. 4.III). This contrasts with the AF coupling found in the absence of SO interactions, which is conserved only for the perpendicular orientation of the magnetization (see illustrations in Table. 4.II). As a consequence of this ferromagnetic coupling, the in-line orientation of magnetization allows an enhancement of μ_{Pt} at the adjacent Pt

sites which reach $\mu_{\text{Pt}} = 0.42\mu_B$, in contrast to $\mu_{\text{Pt}} = 0.12\mu_B$ found for a perpendicular magnetization. In addition, a slight increase of μ_{Fe} is also observed. Once again, the in-line easy axis corresponds to the direction acquiring the largest magnetic moments in both FM and AF configurations. Furthermore, the parallel coupling of the central Pt atom found for the in-line magnetization of the FM arrangement significantly reduces the energy difference between the FM and AF configurations of FePt₃ to only 2.6 meV/atom.

A perpendicular easy axis is found for FePt₄ wires. The FM configuration shows the largest MAE among the considered wires with $\Delta E \simeq 20$ meV/atom. The local magnetic moments are, nonetheless, comparable with those of the in-line magnetization. Similar small differences lead to a MAE of less than 6 meV/atom for the AF configuration, which is 34 meV/atom less stable than the FM ground-state.

From these observations one concludes that, at the studied low Fe concentration regime, the composition is not decisive for the MAE of the FePt_{*n*} wires. Moreover, the internal magnetic order between the 3*d* components affects the MAE to a large extent. Still, a general trend of the behavior of ΔE can not be derived straightforwardly. Furthermore, the results show that relativistic effects do not lead to strong modifications of the local spin moments and internal magnetic order. However, large local orbital moments are induced which are strongly directional dependent. In particular, a violation of the third Hund's rule at the Fe sites occurs in most configurations whenever the magnetization is oriented along the axis of the wire. Such atypical behavior has been previously reported in the literature for VAu₄, MnAu₄ and VPt₃ ordered alloys. In these cases, the effect has been attributed to spin interactions with the orbits of neighboring atoms and the interplay between interatomic and intra-atomic interactions. Namely, the SO coupling of the 5*d* atoms influences, via hybridization of the *d* orbitals, the orbital moment of the 3*d* element causing its reversal [122, 123].

The fact that the violation occurs only for an in-line orientation of the magnetization is likely associated with hybridizations among orbitals of different symmetry for the parallel and perpendicular orientations of the magnetization. The anisotropic behavior of the orbital bonding determines to a large extent the resulting magnetic anisotropy.

Table 4.IV: Calculated local spin and orbital moments μ_α and L_α ($\alpha = \text{Fe, Pt}$) and total magnetic moment per atom $\bar{\mu}_T$ in ordered FePt_n wires at the equilibrium interatomic positions. Results are given in μ_B for an AF and a FM ordering between Fe moments when the magnetization is oriented along and perpendicular to the wire axis as illustrated in the inset figures. The equilibrium interatomic distances $d_{\text{Fe-Pt}}$ and $d_{\text{Pt-Pt}}$ are given in Å. Values for the central Pt sites are displayed in a second row. The anisotropy energy $\Delta E = E_x - E_z$ given in meV/atom is also shown. Negative (positive) values of ΔE correspond to an in-line (perpendicular) easy-axis of magnetization.

Structure	μ_{Fe}	μ_{Pt}	L_{Fe}	L_{Pt}	$\bar{\mu}_T$	$d_{\text{Fe-Pt}}$	$d_{\text{Pt-Pt}}$	ΔE
	3.41	0.45	0.24	0.15	0.0	2.30	2.60	-0.52
	3.40	0.47	-0.38	0.24	0.0	2.30	2.60	
	3.36	0.43	0.27	0.07	1.53	2.29	2.63	-15.14
	3.41	0.56	-0.42	0.24	1.54	2.29	2.62	
	3.31	0.36	0.23	0.10	0.0	2.32	2.48	-11.63
	3.35	0.0	-0.40	0.0	0.0	2.31	2.49	
	3.26	0.18	0.22	-0.01	0.62	2.29	2.50	-4.75
	3.32	-0.39	-0.45	-0.26	0.79	2.29	2.51	
	3.35	0.38	0.26	0.08	0.0	2.30	2.49	2.38
	3.36	0.08	-0.37	0.07	0.0	2.30	2.41	
	3.30	0.14	0.24	-0.00	0.31	2.30	2.50	20.84
	3.32	-0.65	-0.39	-0.30	0.38	2.30	2.40	
	3.30	0.21	-0.39	0.06	0.38	2.30	2.49	20.84
	3.32	-0.57	-0.39	-0.39		2.30	2.41	

Effects of structural optimization

To conclude this analysis, Table 4.IV presents the results of electronic calculations obtained performing a self-consistent optimization of the atomic positions. As a general feature, one observes the expected reduction of about 0.1 Å in the Fe-Pt bond length, and the enlargement of the Pt-Pt bonds. As a result of the increased Fe-Pt hybridization, the values of μ_{Pt} are enhanced while μ_{Fe} is slightly reduced. In FePt₃ and FePt₄, an increase in the bond distance between the antiferromagnetically coupled central and adjacent Pt atoms allows the development of larger moments.

The effects of the structure relaxation have an important influence on the energy relation which concerns the internal magnetic order. After structure optimization, the AF state of FePt₂ is only about 3.5meV/atom lower in energy than the FM configuration. Similarly, the FM ground-state of FePt₃ differs about 4meV/atom from the AF state. The magnetic properties of the chains do not present strong changes in FePt₂ and FePt₄. The differences observed in FePt₃ are related with the change coupling at the central Pt atom.

4.2 Co adatoms on Pt(111): surface coverage, magnetic order and anisotropy

One of the main challenges to achieve the ultimate high-density limit of magnetic recording is the realization of nanostructures which are sufficiently stable against thermally activated magnetic fluctuations. In this context, the MAE is the main factor determining the stability of a magnetic structure. At the nanoscale, the magnetization and MAE are not only strongly sensitive to the size, structure and symmetry of the particle but are also significantly influenced by its coupling with the environment. For instance, the MAE of a supported nanoparticle can be significantly enhanced as a result of the electronic hybridization with the substrate of deposition. This kind of behavior, greatly desirable for magnetic storage applications, is found in a variety of 3d-TM particles deposited at polarizable 5d metal surfaces [19, 20, 61, 66, 114, 124–126]. A remarkable example is the case of a single Co atom deposited at the Pt(111) surface. The Co adatom displays an exceptionally enhanced spin magnetization, which is increased beyond its atomic value as a consequence of electronic charge transfer with the Pt substrate. At the same time, the low atomic coordination allows it to preserve most of its free-atom orbital moment and develop a perpendicular MAE (i.e., an easy axis

perpendicular to the surface plane) of about 9.3 meV [20]. Under this perspective, the use of the particle-substrate interaction as instrument for the further enhancement of the MAE of TM nanoparticles appears as a promising strategy. Moreover, the substrate can also play an important role on the collective behavior of ensembles of magnetic nanostructures, e.g., by mediating an indirect exchange interaction between them. An example of this effect is the RKKY exchange observed among diluted magnetic particles in nonmagnetic host metals. Indeed, such interaction has been recently studied and experimentally measured for Co adatoms on a Pt(111) [47, 48]. It has been shown that Co adatoms occupy both the fcc and hcp hollow sites of the Pt(111) surface [47]. An RKKY exchange interaction, which causes the oscillatory magnetic coupling between adparticles as a function of the distance, is mediated by an unoccupied Pt surface band [47, 48, 127]. Furthermore, a single Co atom induces a large polarization of the surrounding Pt substrate giving rise to an effective magnetic moment of about $5 \mu_B$. This polarization cloud can play an important role on the magnetic coupling of particles at short distances [60]. In particular, the polarization of the substrate can introduce an additional exchange between the nanoparticles which may become essential at higher surface coverages. RKKY interactions and spin-orbit coupling effects can compete with direct exchange interactions and play an important role in determining the MAE. The realization of magnetic devices based on supported TM nanoparticles requires a good understanding of their magnetic interactions in terms of their basic parameters such as adsorption site and density of particles. From this perspective, a detailed study which accounts for all particle-substrate interactions becomes essential. The study of ensembles of deposited atoms organized into regular patterns offers the possibility to investigate the effects of surface coverage and eventually identify trends which can be extrapolated to more complex systems. Here, we consider different two-dimensional arrays of Co adatoms and dimers deposited at a Pt(111) surface and study their fundamental magnetic properties. By varying the Co adsorption position, local arrangement and surface coverage, the role of substrate-particle interactions on the exchange-coupling strength, spin and orbital moments and MAE can be explored and qualitatively estimated.

4.2.1 Computational details

Self consistent electronic calculations have been performed using the VASP computational code (see Chapt. 3.1). Exchange and correlation effects were treated within the GGA approximation [85]. In a supercell approach, surfaces are modeled by a crystal

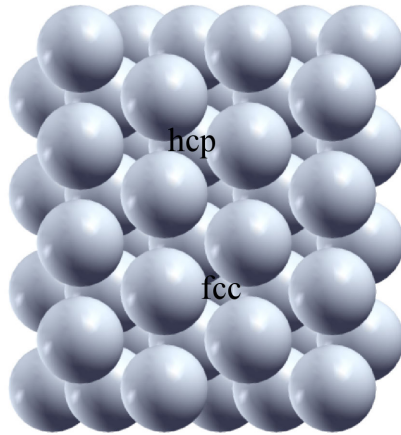


Figure 4.6: Illustration of the considered adatom positions corresponding to the hcp and fcc adsorption sites of a Pt(111) surface.

slab defined within a sufficiently large vacuum region which ensures a negligible interaction between neighboring cells. The study of isolated deposited particles is restricted by the periodicity of the cell. However, ordered arrays of adparticles corresponding to different arrangements and surface coverages can be studied by varying the size and shape of the supercell. In the present study, a five-layer thick slab was constructed based on a previously calculated equilibrium lattice constant of bulk Pt $a = 3.989 \text{ \AA}$, and vacuum space of 14 \AA has been included in the supercell. Co adatoms deposited on top of the Pt(111) slab surface have been studied. Both fcc and hcp hollows of the surface are considered as adsorption positions (see Fig. 4.6). In order to avoid a spurious additional polarization of the slab, the adparticles were located only on one side of the slab. Dipolar corrections have not been included in the calculations. Moreover, the evaluation of all the integrals within the Brillouin zone have been performed using a k -point mesh of $n_k = 5 \times 5 \times 1$. An energy cut-off of 450 eV for the plane-wave basis set has been used. The criterion of total energy convergence was assumed when the difference between two self-consistent cycles was smaller than 10^{-6} eV. Furthermore, the effects of structural relaxation are taken into account by optimizing the atomic positions of the adsorbed atoms and the two topmost layers of the Pt surface. The equilibrium positions are found when the calculated force at each atom is less than 0.001 eV/\AA . Finally, the MAE of the system has been evaluated in the frame of the magnetic force theorem [128] as the difference in the total energy corresponding to two independent non self-consistent calculations corresponding to different orientations of the magnetization.

4.2.2 Local properties

We begin this section by discussing the results obtained for Co adatoms at the lowest considered surface coverages of 1/30 and 1/16. These concentrations correspond roughly to the experimental situations studied in Refs. [20, 47, 48].

For a surface coverage of 1/30, similar values of the calculated local moments are found for Co adatoms at the fcc and hcp perfect lattice positions of the Pt(111) surface ($\mu_{\text{Co}}^{\text{fcc}} = 2.26 \mu_B$ and $\mu_{\text{Co}}^{\text{hcp}} = 2.25 \mu_B$). The hcp site is energetically favorable by an energy difference $E_s = E_{\text{fcc}} - E_{\text{hcp}} = 23.0 \text{ meV}$. Slightly different values are obtained for the 1/16 concentration: $\mu_{\text{Co}}^{\text{fcc}} = 2.20 \mu_B$, $\mu_{\text{Co}}^{\text{hcp}} = 2.24 \mu_B$ and $E_s = 15.5 \text{ meV}$. This difference results from the variation on the substrate polarization due to periodic boundary conditions imposed on supercells of different sizes. In other words, energy changes arise as a consequence of the differences in the total magnetization of the supercell (μ_T).

Moreover, relaxation of the atomic positions decreases the Co local moments by about $\mu_{\text{Co}} \approx 0.1 - 0.15 \mu_B$ while it enhances the polarization of the Pt neighboring surface atoms. Furthermore, structural optimization favors the fcc adsorption site by $E_s = E_{\text{fcc}} - E_{\text{hcp}} = 2.1 \text{ meV}$. Furthermore, calculated values of the MAE $\Delta E = -0.2 \text{ meV}$ and $\Delta E = 4.3 \text{ meV}$ for fcc and hcp adatoms respectively show dissimilar easy-axes.

Similar trends are found for higher Co concentrations. Let us consider Co adatom configurations corresponding to surface coverages of 1/8, 1/6 and 1/4. Results for the calculated magnetic moments, MAE ΔE and site adsorption energy differences $E_s = E_{\text{fcc}} - E_{\text{hcp}}$ are summarized in Tables 4.V, 4.VI, and 4.VII respectively.

First of all, one observes that the local moment of the Co adatoms remains essentially unmodified by increasing surface coverage. An enhancement of the spin moment μ_{Co} beyond its free atomic value is found as a result of adatom-substrate charge transfer. Slightly larger values of μ_{Co} are found for adatoms adsorbed at hcp hollow positions. At the same time, the total magnetization of the systems is enhanced by increasing surface coverage due to a larger polarization induced at the Pt surface. Once more, the total moment μ_T is larger in the case of hcp adatoms.

Furthermore, the values of μ_{Co} are reduced when spin-orbit interactions are taken into account, while large orbital moments $L_{\text{Co}} \approx 0.5 \mu_B$ are induced. Magnetic mo-

Table 4.V: Local (total) spin and orbital moments μ_{Co} and L_{Co} (μ_{T} and L_{T}) in Co/Pt(111) for a surface Cage 1/8. Results are given for non-relaxed (upper box) and relaxed (lower box) structures, with the magnetization lying on (X) and perpendicular to the surface (Z). Values of the MAE $\Delta E = E_{\text{X}} - E_{\text{Z}}$ and site adsorption energy difference $E_{\text{s}} = E_{\text{fcc}} - E_{\text{hcp}}$ are also shown.

fcc	X / Z	hcp	X / Z
$\mu_{\text{Co}} = 2.18 \mu_{\text{B}}$ $\mu_{\text{T}} = 2.52 \mu_{\text{B}}$	$\mu_{\text{Co}} = 1.77/1.81 \mu_{\text{B}}$ $\mu_{\text{T}} = 1.86/2.15 \mu_{\text{B}}$ $L_{\text{Co}} = 0.33/0.45 \mu_{\text{B}}$ $L_{\text{T}} = 0.47/0.55 \mu_{\text{B}}$	$\mu_{\text{Co}} = 2.19 \mu_{\text{B}}$ $\mu_{\text{T}} = 2.49 \mu_{\text{B}}$	$\mu_{\text{Co}} = 1.85/1.86 \mu_{\text{B}}$ $\mu_{\text{T}} = 1.96/2.16 \mu_{\text{B}}$ $L_{\text{Co}} = 0.35/0.46 \mu_{\text{B}}$ $L_{\text{T}} = 0.50/0.48 \mu_{\text{B}}$
$E_{\text{s}} = -13.2 \text{ meV}$	$\Delta E = -15.5 \text{ meV}$	$E_{\text{s}}^{\text{SOC}} = -9.0 \text{ meV}$	$\Delta E = -20.4 \text{ meV}$
$\mu_{\text{Co}} = 2.16 \mu_{\text{B}}$ $\mu_{\text{T}} = 2.85 \mu_{\text{B}}$	$\mu_{\text{Co}} = 1.88/1.85 \mu_{\text{B}}$ $\mu_{\text{T}} = 2.56/2.74 \mu_{\text{B}}$ $L_{\text{Co}} = 0.12/0.23 \mu_{\text{B}}$ $L_{\text{T}} = 0.51/0.40 \mu_{\text{B}}$	$\mu_{\text{Co}} = 2.20 \mu_{\text{B}}$ $\mu_{\text{T}} = 11.58 \mu_{\text{B}}$	$\mu_{\text{Co}} = 1.92/1.88 \mu_{\text{B}}$ $\mu_{\text{T}} = 9.26/9.22 \mu_{\text{B}}$ $L_{\text{Co}} = 0.17/0.28 \mu_{\text{B}}$ $L_{\text{T}} = 2.25/1.92 \mu_{\text{B}}$
$E_{\text{s}} = 38.7 \text{ meV}$	$\Delta E = -36.8 \text{ meV}$	$E_{\text{s}}^{\text{SOC}} = -100.2 \text{ meV}$	$\Delta E = -12.1 \text{ meV}$

Table 4.VI: Local (total) spin and orbital moments μ_{Co} and L_{Co} (μ_{T} and L_{T}) in Co/Pt(111) for a surface coverage 1/6. Results are given for non-relaxed (upper box) and relaxed (lower box) structures, with the magnetization lying on (X) and perpendicular to the surface (Z). Values of the MAE $\Delta E = E_{\text{X}} - E_{\text{Z}}$ and site adsorption energy difference $E_{\text{s}} = E_{\text{fcc}} - E_{\text{hcp}}$ are also shown.

fcc	X / Z	hcp	X / Z
$\mu_{\text{Co}} = 2.20 \mu_{\text{B}}$ $\mu_{\text{T}} = 2.92 \mu_{\text{B}}$	$\mu_{\text{Co}} = 1.86/1.87 \mu_{\text{B}}$ $\mu_{\text{T}} = 2.56/2.64 \mu_{\text{B}}$ $L_{\text{Co}} = 0.33/0.49 \mu_{\text{B}}$ $L_{\text{T}} = 0.54/0.67 \mu_{\text{B}}$	$\mu_{\text{Co}} = 2.24 \mu_{\text{B}}$ $\mu_{\text{T}} = 3.55 \mu_{\text{B}}$	$\mu_{\text{Co}} = 2.15/2.15 \mu_{\text{B}}$ $\mu_{\text{T}} = 3.47/3.56 \mu_{\text{B}}$ $L_{\text{Co}} = 0.25/0.37 \mu_{\text{B}}$ $L_{\text{T}} = 0.66/0.69 \mu_{\text{B}}$
$E_{\text{s}} = 76.8 \text{ meV}$	$\Delta E = 6.3 \text{ meV}$	$E_{\text{s}}^{\text{SOC}} = 52.7 \text{ meV}$	$\Delta E = 14.4 \text{ meV}$
$\mu_{\text{Co}} = 2.18 \mu_{\text{B}}$ $\mu_{\text{T}} = 8.98 \mu_{\text{B}}$	$\mu_{\text{Co}} = 1.83/1.78 \mu_{\text{B}}$ $\mu_{\text{T}} = 7.43/7.40 \mu_{\text{B}}$ $L_{\text{Co}} = 0.14/0.28 \mu_{\text{B}}$ $L_{\text{T}} = 1.68/1.56 \mu_{\text{B}}$	$\mu_{\text{Co}} = 2.20 \mu_{\text{B}}$ $\mu_{\text{T}} = 9.30 \mu_{\text{B}}$	$\mu_{\text{Co}} = 1.96/1.94 \mu_{\text{B}}$ $\mu_{\text{T}} = 7.79/7.89 \mu_{\text{B}}$ $L_{\text{Co}} = 0.16/0.19 \mu_{\text{B}}$ $L_{\text{T}} = 1.74/1.53 \mu_{\text{B}}$
$E_{\text{s}} = 11.7 \text{ meV}$	$\Delta E = -1.0 \text{ meV}$	$E_{\text{s}}^{\text{SOC}} = -26.1 \text{ meV}$	$\Delta E = 8.1 \text{ meV}$

Table 4.VII: Local (total) spin and orbital moments μ_{Co} and L_{Co} (μ_{T} and L_{T}) in Co/Pt(111) for a surface coverage 1/4. Results are given for non-relaxed (upper box) and relaxed (lower box) structures, with the magnetization lying on (X) and perpendicular to the surface (Z). Values of the MAE $\Delta E = E_{\text{X}} - E_{\text{Z}}$ and site adsorption energy difference $E_{\text{s}} = E_{\text{fcc}} - E_{\text{hcp}}$ are also shown.

fcc	X / Z	hcp	X / Z
$\mu_{\text{Co}} = 2.18 \mu_{\text{B}}$ $\mu_{\text{T}} = 4.69 \mu_{\text{B}}$	$\mu_{\text{Co}} = 1.77/1.80 \mu_{\text{B}}$ $\mu_{\text{T}} = 3.73/3.93 \mu_{\text{B}}$ $L_{\text{Co}} = 0.33/0.45 \mu_{\text{B}}$ $L_{\text{T}} = 0.95/0.91 \mu_{\text{B}}$	$\mu_{\text{Co}} = 2.23 \mu_{\text{B}}$ $\mu_{\text{T}} = 5.05 \mu_{\text{B}}$	$\mu_{\text{Co}} = 2.09/2.09 \mu_{\text{B}}$ $\mu_{\text{T}} = 4.31/4.43 \mu_{\text{B}}$ $L_{\text{Co}} = 0.23/0.35 \mu_{\text{B}}$ $L_{\text{T}} = 0.94/0.87 \mu_{\text{B}}$
$E_{\text{s}} = 80.2 \text{ meV}$	$\Delta E = -8.4 \text{ meV}$	$E_{\text{s}}^{\text{SOC}} = 52.0 \text{ meV}$	$\Delta E = -11.5 \text{ meV}$
$\mu_{\text{Co}} = 2.16 \mu_{\text{B}}$ $\mu_{\text{T}} = 5.64 \mu_{\text{B}}$	$\mu_{\text{Co}} = 1.84/1.83 \mu_{\text{B}}$ $\mu_{\text{T}} = 1.04/0.86 \mu_{\text{B}}$ $L_{\text{Co}} = 0.10/0.20 \mu_{\text{B}}$ $L_{\text{T}} = 1.04/0.86 \mu_{\text{B}}$	$\mu_{\text{Co}} = 2.19 \mu_{\text{B}}$ $\mu_{\text{T}} = 7.22 \mu_{\text{B}}$	$\mu_{\text{Co}} = 1.92/1.85 \mu_{\text{B}}$ $\mu_{\text{T}} = 6.0/5.94 \mu_{\text{B}}$ $L_{\text{Co}} = 0.19/0.25 \mu_{\text{B}}$ $L_{\text{T}} = 1.43/1.18 \mu_{\text{B}}$
$E_{\text{s}} = -3.9 \text{ meV}$	$\Delta E = -16.1 \text{ meV}$	$E_{\text{s}}^{\text{SOC}} = -50.5 \text{ meV}$	$\Delta E = -15.0 \text{ meV}$

ments are, in general, slightly larger for a perpendicular (Z) orientation of the magnetization.

Moreover, an enhancement of the total orbital moment μ_{T} is observed for increasing surface coverage. The increment is, however, lessened after the relaxation of the structure, which causes a strong overall enhancement of the induced Pt polarization and therefore of the total magnetization μ_{T} and L_{T} . This effect is the result of a larger Co-Pt hybridization, since the Co adatom is found closer to the surface after structural optimization. In contrast to this, the local orbital moment of the Co adatoms are reduced.

Finally, one observes strong fluctuations of the calculated values of ΔE and E_{s} , in particular, when comparing results for different sizes of the supercell. These variations are mostly a result of large differences in the total magnetization μ_{T} , which are consistently overestimated for high surface coverages due to the finite thickness of the slab used to model the surface. These deviations represent an indication of the critical dependence of the magnetic properties on the atomic environment. Although this inconsistency prevents us to provide a quantitative picture of the effects of surface coverage on the MAE, one can generalize a qualitative trend. In particular, the strong tendency towards ferromagnetism at all surface coverages, displaying enhanced spin and orbital moments for Co as well as for Pt.

*Tuning substrate-mediated exchange interactions
between TM impurities in Cu(111) by means of
external surface charging*

One of the main interests concerning modern device engineering is the development of methods to control the magnetic state of nanoscaled materials. The use of external electric fields (EFs) for the reversible tuning of the intrinsic magnetic properties is currently a most active research area in this context. [129–137] Important advances have been recently achieved in this field. A noteworthy example is, for instance, the electrical manipulation of ferromagnetism in a Mn semiconductor alloy demonstrated by Ohno *et al.* [133] In this system, valence-band holes are responsible of mediating a ferromagnetic exchange interaction between the localized moments of the Mn atoms. The electric field modifies the concentration of charge carriers inside the semiconductor, thereby allowing the tuning of the ferromagnetic-state transition temperature. In a similar way, Chiba *et al.* succeeded to control the magnetization vector (i.e the magnitude as well as the orientation of magnetization) of a metal-insulator-semiconductor structure [131].

Recently, the effects of EFs on metallic systems have been explored. It is well known that EFs are effectively screened, within an atomic length scale, by the conduction electrons at the surface of a metal. Despite the minimal screening length, the charge density redistribution induced by an external field can significantly influence the surface electronic structure [138–141].

In the case of magnetic transition metals (TMs), the charge redistribution caused by the EF is likely to affect the unpaired d -electron states close to the Fermi energy which are responsible of itinerant-electron magnetism. As a consequence, the spin-dependent screening of the EF can induce substantial modifications of the magnetization and magnetic anisotropy energy [141]. Outstanding examples of this effect have been reported, for instance, in ultra-thin ferromagnetic films [135, 142–144].

In this context, similar manipulations have been achieved experimentally by applying a voltage through a liquid-electrolyte in contact with the metal surface. The formation of an electrolytic-charge double layer above the metallic surface allows to exert rather high EFs by applying relatively low voltages. Using this method, Shimamura *et al.* [137] attained a modification of up to 100K in the Curie temperature of Co ultra-thin films using gate voltages in the range of $\pm 2V$. By similar means, the reversible tuning of the MAE of FePt and FePd thin-films has been successfully achieved [136]. From a theoretical perspective, calculations performed by Ruiz-Díaz *et al.* show that the MAE and even the easy-axis of magnetization of Fe-Pt multilayers can be tuned by surface charging [145]. Similarly, a study of Gong *et al.* reveals a large reduction of the magnetic moments and MAE of an Fe monolayer caused by its deposition on graphene, which is lifted by introducing an excess of charge in the system [147].

In supported nanoparticles the EF can lead to modifications of the electronic coupling between the particles and the substrate, which further influence their magnetic properties. A notable theoretical study performed by Hu *et al.* revealed that the substrate induced spin reorientation of a Fe-phthalocyanine molecule on O-Cu(110) can be controlled by means of an applied EF [148]. The importance of the substrate has been also pointed out for Ag and Ni supported manganese dimers, [23] and in gold atoms and NO₂ molecules on graphene [149]. In this context, the EF control of the structure and deposition patterning of ad-particles on graphene and MgO films has been theoretically addressed [149, 150].

Besides the modification of the intrinsic magnetic properties, another promising application of EFs has been illustrated by Fechner *et al.* [151]. Their theoretical study

shows the possibility of switching the relative orientation of magnetization of two Fe layers in a Fe/Au/Fe trilayer, which is the result of a Ruderman-Kittel-Kasuya-Yosida-like (RKKY) interactions between them. An external EF is used to induce the polarization of a ferroelectric material in contact with one of the external Fe layers, which causes a spin-dependent screening of charge at the interface. The resulting spin asymmetry modifies the phase and amplitude of the Au mediated RKKY interactions controlling the exchange coupling between the Fe layers. This opens new exciting possibilities of EF controlled magnetic coupling, since the RKKY interactions are found in a variety of layered systems [42, 152, 153] as well as between magnetic particles deposited at metal surfaces [17, 25, 32–34, 42, 47, 48, 152–156]. In the later case, an interparticle magnetic exchange coupling is mediated by surface-state electrons, which are located precisely in the surface region, where significant charge redistributions are expected to be induced by external EFs. Although the strength of these interactions is rather weak, of the order of few meVs, they have a strong influence on the growth and relative magnetic ordering of nanostructures at low temperatures [26, 27, 33, 46]. Furthermore, interesting modifications in the dispersion relation of the surface states, which involve modifications of the effective electron mass and Fermi wavevector, have been revealed by theoretical investigations on the effect of EFs on the Cu(111) surface [138–140]. Such changes are expected to have consequences on the scattering of these surface electrons, which can affect the RKKY interactions between deposited particles [33]. It is therefore of considerable interest, to investigate the possibility of manipulating interparticle magnetic interactions by tuning the surface electronic density of a noble metal surface.

In the present study, we consider the case of substitutional Co and Fe atomic impurities at the Cu(111) surface and investigate the modifications of the substrate-mediated magnetic interaction as a result of an external-charge gathering at the interface. This study intends to simulate the behavior of the system when immersed in a liquid electrolyte, used as an insulating ionic layer, where an electrolytic-charge accumulation at the surface can be induced and controlled by applying an external voltage. In the present work, such situation is modeled by introducing an overlayer of point charges q on top of a Cu(111) surface.

The difficulties of modeling real metal/electrolyte systems by first principles techniques have been discussed in the literature. A recent survey on this matter can be found, for instance, in Ref. [158]. It is true that the present model overlooks the possible effects associated to the binding and adsorption energies of the electrolyte ions accumulated on the surface. Nevertheless, for the purpose of this study, the sim-

plification of the electrolyte ions as a sheet of fixed point charges of varying value q can be justified by the fact that the adsorption energy and position of the ions are approximately independent of the strength of the applied electrode potential [158]. Notice that an influence of the charge and adsorption energy of the ions on the surface reconstruction has been reported for some metal-electrolyte interfaces [159–162]. Still, the possible structural changes of the surface caused by ion adsorption are beyond the scope of the present investigations.

In a real metal-electrolyte system, the accumulated external charge depends on the ion coverage of the metal surface, which is distributed over several layers above the surface. In our model we assume for simplicity that the surface charges are located at a single layer just above the surface. This is not expected to be a serious limitation as long as the distribution of charge is uniform within the surface, since the electric field generated by a uniform planar density is independent of the distance to the plane. Moreover, the Coulomb forces exerted by a large electrolytic-charge accumulation adsorbed at the surface cause the formation of a diffuse additional layer of opposite-charge electrolyte-ions, which constitutes the so called electrical double layer. In order to evaluate the possible effects of this phenomenon, we have performed test calculations considering a second charge overlayer consisting of point charges of value $-q$ located at the atomic layer above the surface. The results show that the electronic structure of the surface is not significantly affected by the presence of the additional overlayer. Therefore, in the present investigation, we have considered the effect of a single overlayer of external charges on the modification of the substrate-mediated interactions as a result of the metallic screening and charge rearrangements at the surface and impurity sites.

5.1 Computational details

Density-functional calculations of the magnetic exchange couplings between Co and Fe atomic surface impurities have been performed using the Green function (GF) Korringa-Kohn-Rostoker (KKR) method described in Sec. 3.2. Exchange and correlation effects are treated in the local spin-density approximation (LSDA) [84]. In all calculations, the atomic positions remain fixed to the bulk Cu crystal structure having the experimental lattice constant $a = 3.615 \text{ \AA}$. The surface has been modeled by replacing the ion potentials of a six-layer-thick Cu(111) slab with vacuum spheres. The separation distance between the resulting two half-crystals is thus large enough to avoid

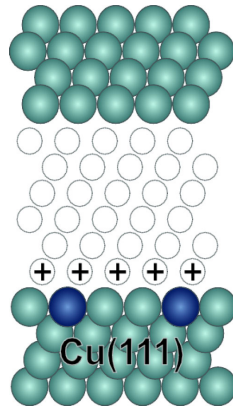


Figure 5.1: Schematic diagram of the surface model. Impurities (dark spheres) and external overlayer charges (plus signs) are also depicted.

any significant electronic interaction between them. Impurities occupy atomic sites in the top-most layer of the Cu(111) surface [164]. The overlayer of external charges simulating the effect of the electrolyte is modeled by point charges q located at the perfect lattice positions of a crystal layer just above the Cu(111) surface [see Fig. 5.1]. In other words, the external charges are located at the atomic positions of an idealized Cu-crystal layer above the surface. Values of q in the range $-0.5 \leq q/e \leq 0.5$ have been considered for the calculations. Moreover, notice that these overlayer-charges are treated as external potentials and are therefore not involved in the self-consistent redistribution of electronic density [42, 101, 138, 152, 153, 165].

Self-consistent calculations have been performed for ferromagnetic (FM) and antiferromagnetic (AF) alignments between two impurities, for inter-impurity distances r corresponding to all lattice positions up to eleventh nearest neighbors (NNs) on the Cu(111) surface. The exchange interaction energy is then obtained from the difference $\Delta E = E_{\text{FM}} - E_{\text{AF}}$ between the corresponding total energies.

5.2 Results

5.2.1 Clean surface

Before discussing the effect of external surface charges on the magnetic behavior of the impurities, it is interesting to analyze the changes taking place in the electronic

structure of the clean surface. For a clean Cu(111) in the absence of external charges, a spill-off of electronic density of about 0.2 electrons per atom is found in the vacuum region above the surface. A charged overlayer having $q < 0$ causes the depletion of up to 75% of this interface charge density, which is pushed into the bulk crystal. The topmost layer of Cu(111) is also affected by the EF generated by the external charge, which shifts part of the electron density towards deeper layers. A reduction of charge of 0.3 electrons, is observed at the Cu surface atoms for the largest considered $q = -0.5$. On the contrary, external charges $q > 0$ shift about 0.4 electrons per surface atom towards the vacuum (for $q = 0.5$). In this case, the amount of charge at top most layer of Cu(111) is almost unaffected.

Important changes are also found in the electronic structure. Fig. 5.2 shows the local density of s and p states at the top-most layer of the Cu(111) surface. The black line corresponds to the LDOS in the absence of external charges. A step feature is observed at about 0.5 eV below the Fermi energy ε_F , which is consistent with the onset of the surface-state band. As shown in Fig. 5.2, strong modifications of this characteristic profile are induced by the presence of external surface charge. The dotted (dashed) curves demonstrate the modification of the LDOS caused by increasing negative (positive) values of the overlayer external charge for $|q| \leq 0.5$. One observes that negative surface charges enhance the step feature, progressively shifting it towards higher energies as $|q|$ increases. In fact, for the smallest considered value of $q = -0.1$, the step is near the Fermi level, while it is shifted well beyond ε_F already for $q < -0.2$. Additionally, a peak in the local density of s states arises at about 1.5 meV below ε_F . This peak is also observed in the absence of charge and softened for $q > 0$. Thus, it should not be related to the formation of a new localized electronic band.

In general, positive surface charges affect the LDOS to a much lower extent. However, notice that any trace of the surface band vanishes for all considered values of $q > 0$. Furthermore, one observes that the density of s (p) states below ε_F is reduced in the presence of positive (negative) external charge. These results indicate that surface charging should dramatically affect the substrate-mediated interaction between impurities.

Finally, in order to assess the possibility of structural modifications induced by such accumulation of external charge density at the surface, we have performed a few test calculations on a five-layer Cu(111) slab using VASP (see Sec. 3.1). Self-consistent structural optimizations of the two topmost layers of the surface have been

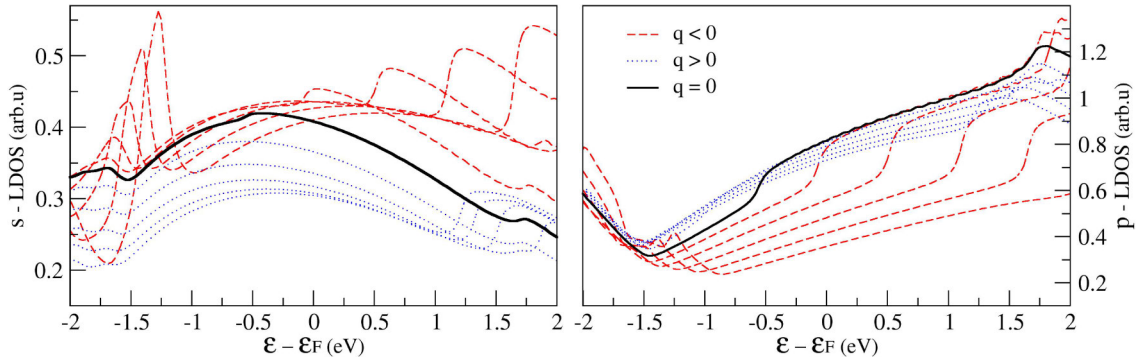


Figure 5.2: Local density of s and p states at the topmost layer of the Cu(111) surface. Dotted (dashed) lines correspond to increasing negative (positive) values of the overlayer external charge $|q| = 0.1, 0.2, 0.3, 0.4$ and 0.5 .

performed for a neutral system and in the presence of a negative (positive) charge unbalance of $q \pm 0.3$ electrons per surface atom. In this case, the charge doping is controlled by adding (removing) valence electrons to the neutral system (see for instance Refs. [145, 163]). After self-consistency is achieved, the additional or missing charge remains essentially near the Cu surface. The resulting structural relaxations are found to be small and nearly identical for the three considered systems. Therefore, we do not expect important external-charge induced changes in the surface structure for the values of overlayer charges q considered in this study.

5.2.2 Single impurity

It is instructive to begin our analysis discussing the magnetic behavior of a single impurity. In the absence of overlayer charge, the calculated magnetic moment of a surface substitutional Co impurity in Cu(111) is $\mu_{\text{Co}} = 1.35\mu_B$, while for an Fe impurity it is $\mu_{\text{Fe}} = 2.80\mu_B$. These magnetic moments are largely affected by the EF generated by overlayer charges. Fig. 5.3 shows the values μ_{Co} and μ_{Fe} as a function of the overlayer charge q . As in the case of the clean surface, for an overlayer of negative charges $q < 0$, the repulsive electrostatic potential displaces the electronic charge away from the surface into the Cu bulk, causing a reduction of the number electrons at the Co or Fe atom. The redistribution of charge density at the impurity sites concerns mainly the higher energy minority-spin states. It therefore leads to an enhancement of the impurity magnetic moments [146]. As $|q|$ increases ($q < 0$) a monotonous increase of μ_{Co} and μ_{Fe} is observed reaching $\mu_{\text{Co}} = 1.95\mu_B$ and $\mu_{\text{Fe}} = 3.24\mu_B$ for $q = -0.5$ [see

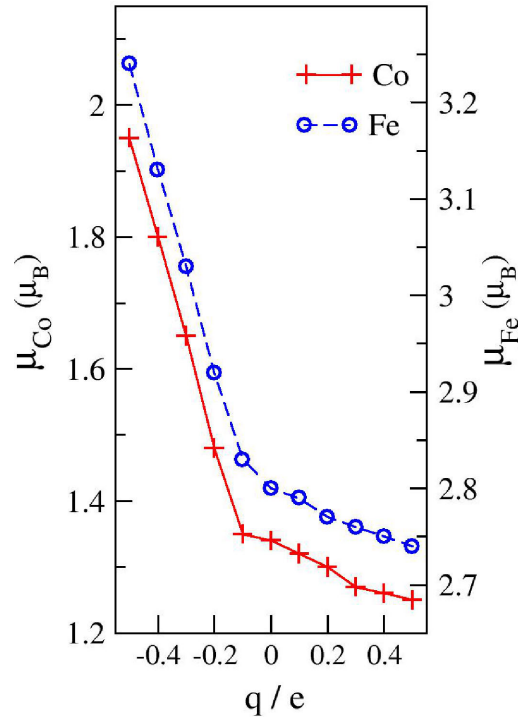


Figure 5.3: Calculated local magnetic moments at a single substitutional impurity as a function of overlayer charge q [146]. The left (right) scale corresponds to Co (Fe).

Fig. 5.3]. For this value of q , the number of electrons at the impurity site is reduced by about 0.3 to 0.4 electrons which causes an enhancement of $0.6\mu_B$ and $0.4\mu_B$ in the magnetic moment of Co and Fe respectively. It should be however noted that the decrease of electronic density and magnetic moments does not follow a linear behavior as a function of q . For instance, an overlayer charge $q = -0.1$ displaces only about 0.03 electrons from the Co impurity, enhancing μ_{Co} by less than $0.01\mu_B$ with respect to the neutral system. In contrast, increasing $|q|$ from $q = -0.2$ to $q = -0.3$ implies that the number of electrons inside the Co atomic sphere is reduced by nearly 0.1 and that μ_{Co} increases by about $0.17\mu_B$. A similar behavior is observed for Fe impurities.

The reason for the generally weak effect of small values of $|q|$ on the surface atoms, is probably related to the natural spill out of the surface electron density into the vacuum. As discussed in Sec. 5.2.1 for the neutral system, about 0.2 electrons per atom are found in the volume outside the atomic spheres of the surface. These are basically the electrons that are first displaced in order to screen the EF. Consequently, the orbital occupations at the impurity sites are not much affected for small q . It is

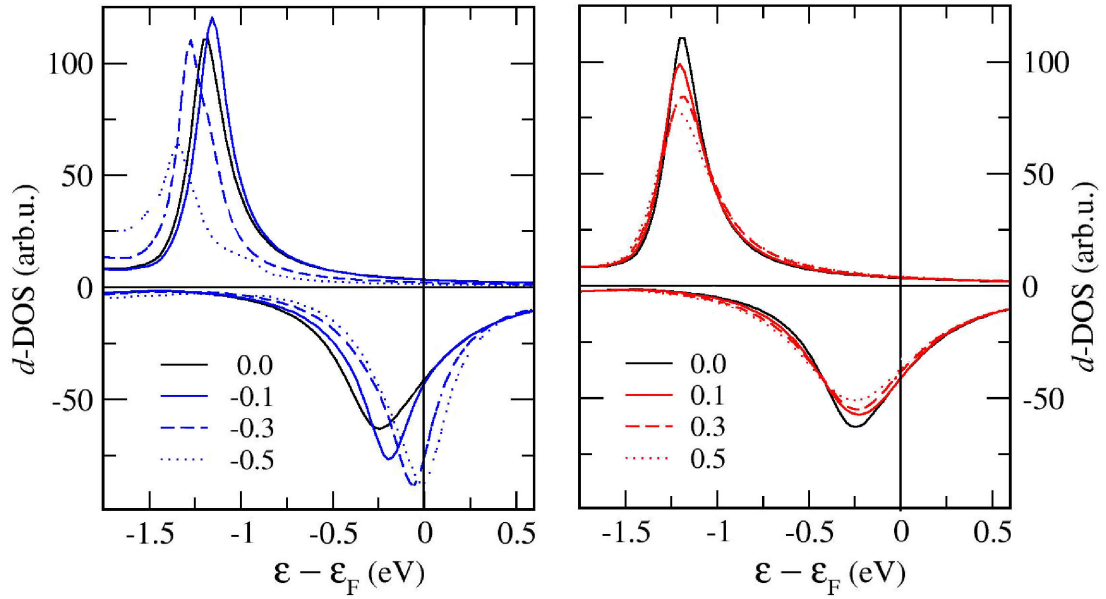


Figure 5.4: Local density of d -states at a surface substitutional Co impurity in Cu(111) [146]. The left (right) subfigure corresponds to negative (positive) surface charge per atom q , as indicated in the insets.

only for larger values of $|q|$ that a significant electron-density depletion at the impurity and surface atoms occurs.

For positive overlayer charge $q > 0$, one observes a slight reduction of the impurity magnetic moment. The effect is, however, far less important than for $q < 0$. For instance, $\mu_{\text{Co}} = 1.25\mu_B$ and $\mu_{\text{Fe}} = 2.74\mu_B$ for the largest considered overlayer charge $q = 0.5$. In fact, the attractive potential corresponding to $q > 0$ shifts the electronic density outside the surface by keeping the uppermost metal layer, where the magnetic impurities are located, essentially neutral.

The previous results can be understood by analysing the effects of the charge overlayer on the local DOS at the impurity site. Fig. 5.4 shows the local density of d -states at a surface substitutional Co impurity for different values of q . For $q < 0$ (Fig. 5.4 left) a shift is observed in both majority-spin and minority-spin bands. Near the Fermi level, the minority-spin band is progressively shifted towards higher energies for increasing values of $|q|$. The electronic occupation of this band is thereby reduced, resulting in the observed enhancement of the local magnetic moment. For a small value of overlayer charge ($q = -0.1$) the majority-spin band is, as in the case of the minority-spin band, slightly shifted towards higher energies. On the contrary, stronger EFs $q < -0.1$ displace this band towards lower energies. This difference

is probably related to the non-linear behavior observed in the enhancement of the magnetic moments, which is lower for small values of q . The opposite displacement of the majority and minority spin bands for $q < -0.1$ results in a larger exchange splitting which further increases the local moment. The behavior observed for $q > 0$ (Fig. 5.4 right) is remarkably different. Even for the largest considered value of $q = 0.5$, both majority-spin and minority-spin bands remain almost unmodified. The slight reduction of the local magnetic moments is probably related to the small decrease of the density of states.

As we shall see later, the changes in the magnetic moments are very important for the magnetic coupling between impurities. On one side, for large inter-impurity distances, the changes in the magnetic moment of the impurities modify the spin-dependent scattering potential of the surface electrons, which mediate the interactions among the magnetic $3d$ atoms. On the other side, at short inter-impurity distances, the depletion of charge density induced by the EF can lead to significant modifications of the direct hybridizations, for example, between NN impurities [146]. At such short distances, the direct electronic hybridizations generally results in further modifications on the local magnetic moments. In contrast, at larger impurity separations, beyond second NNs, the local magnetic moments have essentially the single-impurity values (see Fig. 5.3).

5.2.3 Magnetic exchange interactions

In order to investigate the effect of overlayer charges on the relative magnetic coupling between impurities, Fig. 5.5 shows the calculated effective exchange interaction energy $\Delta E = E_{\text{FM}} - E_{\text{AF}}$ between two Co impurities as a function of their separation distance r , for different values of overlayer charge q per surface atom. Negative (positive) values of ΔE imply that a FM (AF) alignment of the impurity moments is favored. The results for Fe impurities are shown in Fig. 5.6. Notice that the values of r correspond to the different substitutional impurity positions at the Cu(111) surface. They are the same in Figs. 5.5 and 5.6, whereas the ranges of ΔE differ.

Let us first discuss the behavior of ΔE in the absence of external charge, which corresponds to the dotted lines in Figs. 5.5 and 5.6. Although the strength of the interaction $|\Delta E|$ differ, the results for Co and Fe impurities display the same oscillatory form, which is characteristic of RKKY-like interactions due to conduction electrons. The similarity of the oscillations for both TMs indicates the common substrate-

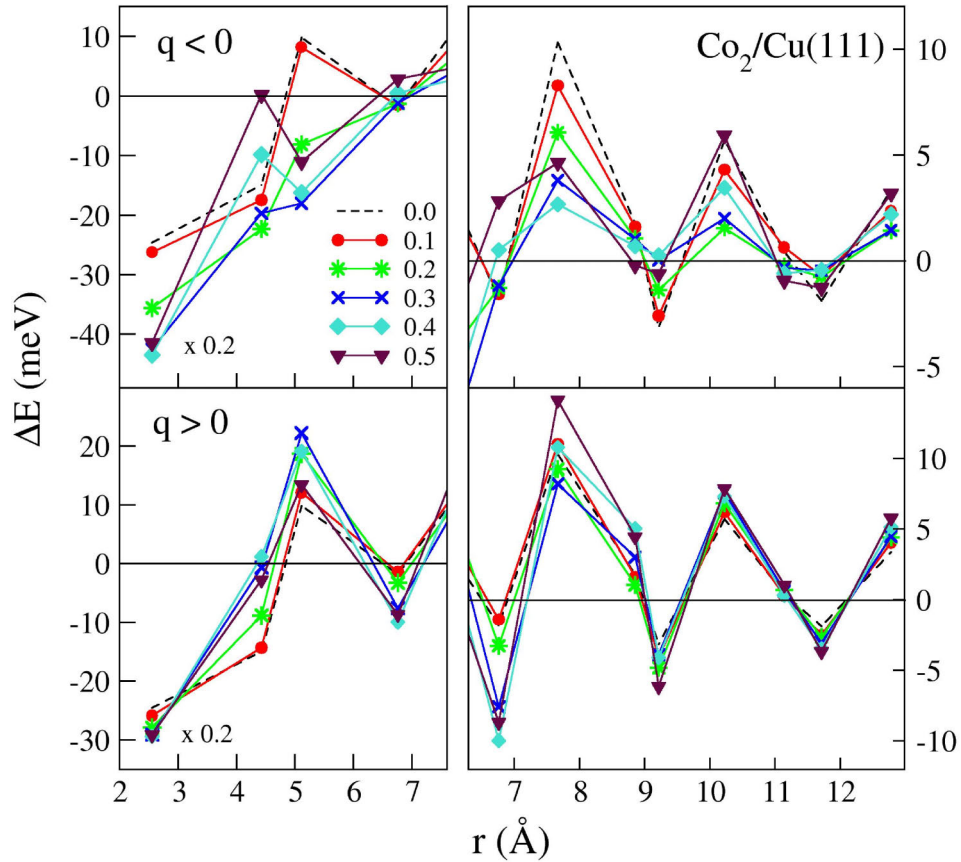


Figure 5.5: Exchange interaction energy $\Delta E = E_{\text{FM}} - E_{\text{AF}}$ between two Co impurities at the Cu(111) surface as a function of the Co-Co distance r [146]. The upper (lower) subfigure corresponds to negative (positive) surface charges per atom q . The considered absolute values of q are indicated in the inset. Note that the values of ΔE for NNs ($r = 2.55$) have been multiplied by a factor 0.2. The lines connecting the points are a guide to the eye.

mediated interaction mechanism [146]. In the present case, where the TM atoms occupy sites within the topmost layer of Cu(111), both surface and bulk electrons mediate the interaction between the impurities [32, 33, 155–157]. Therefore, the observed oscillation wavelength ($\simeq 2.5\text{\AA}$) lies in-between the values 1.7\AA and 14.5\AA expected for bulk impurities and surface adatoms respectively [44]. In the former case, bulk electrons are responsible for the exchange interactions, while in the latter case only surface electrons mediate the long-range magnetic coupling. Notice that the actual decay of the interaction amplitude differs from the $1/r^2$ and $1/r^5$ behaviors, which are typical of surface adatoms and bulk impurities [44]. In this sense, one can expect that at short inter-impurity distances r the contribution of the bulk-electrons dominates

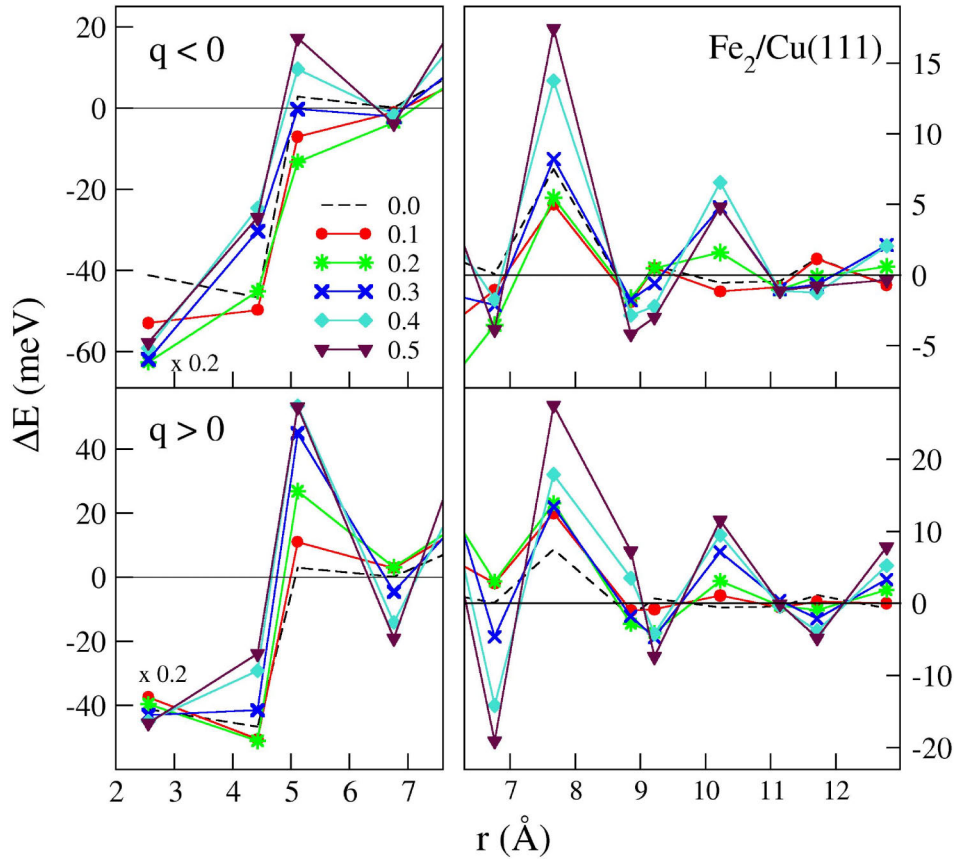


Figure 5.6: Exchange interaction energy $\Delta E = E_{\text{FM}} - E_{\text{AF}}$ between two Fe impurities at the Cu(111) surface as a function of the Fe-Fe distance r [146]. The upper (lower) subfigure corresponds to negative (positive) surface charges per atom q . The considered absolute values of q are indicated in the inset. Note that the values of ΔE for NNs ($r = 2.55$) have been multiplied by a factor 0.2. The lines connecting the points are a guide to the eye.

the magnetic exchange, while at larger distances the behavior will be predominantly determined by the scattering of the surface electrons. In any case, it should be recalled that the wavelength and decay law of the interactions should be evaluated in the asymptotic large distance regime, at much larger inter-impurity distances than those considered in this study.

In order to analyze the effects of the external charge overlayer on ΔE it is meaningful to distinguish two ranges of inter-impurity distance r : large separations, beyond fourth NNs ($r \gtrsim 7 \text{ \AA}$) where the magnetic exchange couplings are mediated by delocalized electrons, and short separations, where direct hybridizations involving localized

orbitals also play an important role. The calculated values of ΔE for large (short) inter-impurity distances are shown in Figs. 5.5 and 5.6 on the right (left) subfigures.

Independently of the value and polarity of the overlayer charge q , the RKKY-like oscillations of ΔE are still present at large distances. While the oscillation wavelength remains essentially as in the neutral surface, the strength of ΔE is significantly modified in various ways depending on the polarity of the external charge and on the impurity atom (Co or Fe). For instance, positive q causes an enhancement of $|\Delta E|$ with respect to the neutral surface, particularly in the case of Fe. For $q < 0$, $|\Delta E|$ is in general reduced for Co impurities, while it is enhanced in the case of Fe (See Figs. 5.5 and 5.6). A detailed observation of the behavior of $|\Delta E|$ as a function of $|q|$ (Fig. 5.6) reveals that for small values of $|q| < 0.3$ the strength of the interaction is, in fact, reduced. It is only for $q \leq -0.3$ that $|\Delta E|$ increases. Moreover, notice that negative (positive) external surface charges enhance the magnetic interaction at short (large) inter-impurity distances. For large r , the modifications of ΔE can be of the order of 10 meV. Furthermore, one observes that external surface charges $q > 0$ enhance FM as well as AF couplings for both TM impurities, while charges $q < 0$ do not significantly enhance FM interactions for any of them.

The effects of overlayer charging on the magnetic interactions become clearly stronger as the distance r is reduced. For example, if the impurities occupy any of the first four nearest neighbor (NN) positions, positive q can enhance $|\Delta E|$ by more than 10 meV in the case of Co impurities, and even by 40 meV in the case of Fe third NN pairs ($r = 5.11 \text{ \AA}$). The largest changes in $|\Delta E|$ are generally found already for $q = 0.3$ in Co and for $q = 0.4$ in Fe. For certain distances, varying the external charge q can result in a change of sign of ΔE which enables the tuning of the magnetic coupling from FM to AF or vice versa. One example of this switching is found for third NN impurities ($r = 5.11 \text{ \AA}$) where $q < 0$ favors a FM alignment for both TMs (see Figs. 5.5 and 5.6). A similar switching of the magnetic coupling is obtained at other inter-impurity distances r by changing the sign of q . See for example, for Co impurities at distances $r \simeq 6.8 \text{ \AA}$ and $r \simeq 11.1 \text{ \AA}$ in Fig. 5.5. In these cases, the coupling is FM (AF) for $q \geq 0$ while it is weakly AF (FM) for $q < -0.1$. Additionally, a remarkable non-monotonous dependence of ΔE on q is observed at several distances. For instance, the third NN Fe coupling in Fig. 5.6, which is weakly AF for $q = 0$, changes first to strongly ferromagnetic for small $q < 0$ ($\Delta E \simeq -12 \text{ meV}$ for $q = -0.2$) and finally returns to strongly AF for $q = -0.5$ ($\Delta E \simeq 18 \text{ meV}$). These results are quite remarkable. They demonstrate the possibilities of tuning the magnetic interaction between surface impurities by means of external electric fields.

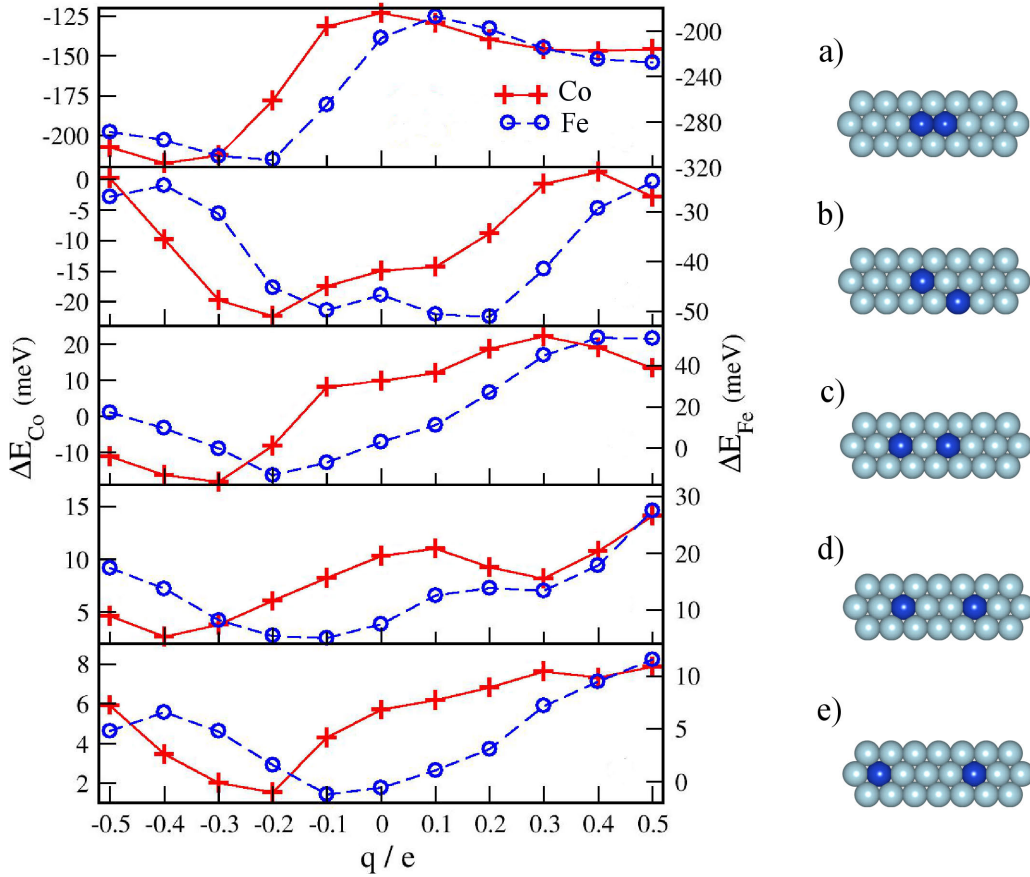


Figure 5.7: Exchange interaction energy $\Delta E = E_{\text{FM}} - E_{\text{AF}}$ of Co and Fe substitutional impurities at the Cu(111) surface as a function of the surface charge per atom q [146]. The subfigures (a)-(e) correspond to different impurity positions ordered by increasing distance as illustrated in the insets. Notice that the left (right) energy scale correspond to Co (Fe).

In Fig. 5.7 the exchange interaction energies ΔE between two Co impurities and between two Fe impurities are given as a function of q for impurity pairs at the different positions illustrated in the insets.

The calculated values of $|\Delta E|$ are generally greater for Fe due to its larger magnetic moment. Similarly, the modifications induced by the overlayer charges are also stronger in the case of Fe. Yet, the general behavior of ΔE as a function of q is comparable for both transition metals (TMs), in particular at the shortest inter-impurity distances. The results corresponding to impurities at NN positions are shown in Fig. 5.7(a). At this distance ($r \simeq 2.55 \text{ \AA}$) the direct electronic hybridization between the impurities is very strong and dominates their interaction. The absolute values of ΔE are, therefore, about one order of magnitude larger than for any impurity

pair at larger distances [146]. The overlayer charge affects significantly the magnetic exchange, since it controls the displacement of electronic density around the impurities. As a consequence, the orbital occupations near the Fermi energy are modified, thereby changing the spin-polarized density distribution and the TM hybridizations, which ultimately determine the coupling.

Modifications to ΔE of the order of 1 eV are indeed achieved for NN impurities when surface charging is in the range $-0.3 < q < 0.3$. As in the case of a single impurity, the most important possibilities of tuning the magnetic interactions are obtained by negative values of q . An illustrative way to analyze the behavior of ΔE for NN impurities is to consider their interaction energy E_{int} for different magnetic orders, which is defined as the total energy difference between a substitutional dimer and two isolated surface impurities: $E_{\text{int}} = E_{\text{d}} - 2E_{\text{s}}$, where E_{d} is the total energy of the dimer-at-surface complex and E_{s} the total energy of a single substitutional impurity. According to this, values of $E_{\text{int}} < 0$ indicate that the dimer formation is energetically favorable. In Fig. 5.8 E_{int} is shown for the FM and AF arrangement of a NN Co dimer as a function of q . For $q = 0$, both magnetic configurations of the dimer are stable. The binding energy is, however, about one order of magnitude larger for the FM state. The calculated local magnetic moment of the Co atoms in a ferromagnetic NN dimer is $\mu_{\text{Co}} = 1.45\mu_B$ ($q = 0$). This value is enhanced up to $\mu_{\text{Co}} > 1.7\mu_B$ for a negative overlayer charge $q \leq -0.3$. Accordingly, an increase of about 80 meV in $|E_{\text{int}}|$ is observed for the FM dimer (see Fig. 5.8). A contrasting behavior is found in the case of antiferromagnetic order. For the AF state the local moments are much smaller: $\mu_{\text{Co}} = 1.24\mu_B$ for $q = 0$. Here, already the smallest considered value of $q < 0$, causes an enhancement of the local spin moments which destabilizes the AF dimer significantly ($E_{\text{int}} \approx 0.0$). On the contrary, positive values of q induce a slight reduction of the local magnetic moments at the Co atoms irrespectively of the magnetic order. The change is in fact more pronounced in the AF configuration. Although the effect is far less important than for $q < 0$, the binding energy is slightly enhanced for both magnetic configurations (see Fig. 5.8). From this perspective, one conclude that the results for ΔE [Fig. 5.7(a)] are essentially dominated by the large change in the binding energy of the FM configuration. The ferromagnetic coupling between NNs is, thus, strongly stabilized for $q < 0$, being maximal at $q = -0.3$, while it is only slightly strengthened for $q > 0$. The behavior observed in Fig. 5.7(a) for Fe can be explained in a similar way by the changes of μ_{Fe} and E_{int} .

The enhancement of the local spin moments for negative q can be understood as in the single impurity case. Beyond a certain threshold (typically $|q| \geq 0.3$) the

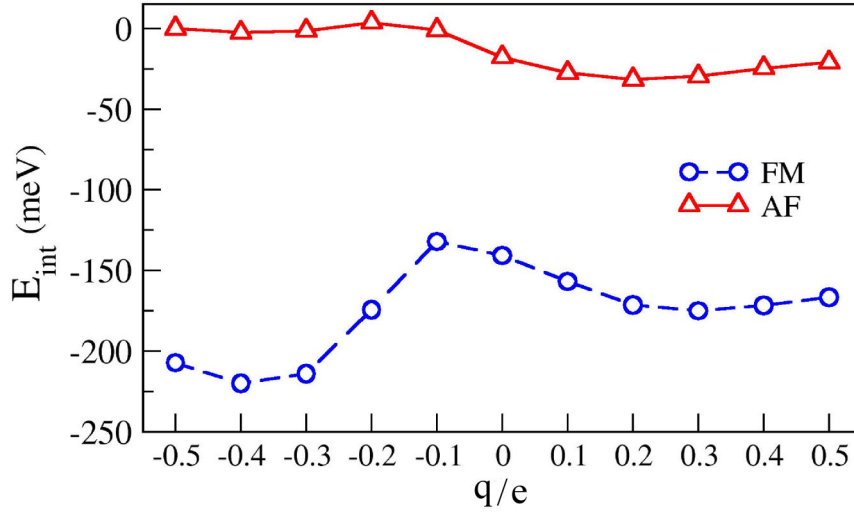


Figure 5.8: Interaction energy E_{int} between Co NN impurities as a function of overlayer charge q [146].

EF generated by the $q < 0$ overlayer charges causes a significant depletion of the electronic density at the surface layer. Thus, there are states near the Fermi energy which become unoccupied. At the impurity sites, these states involve local minority-spin orbitals. Therefore, an enhancement of the impurity spin moments follows in both the FM and AF configurations. The local DOS of d -electrons at a Co atom in a ferromagnetic NN dimer is shown in Fig. 5.9. Here, one observes that for $q < 0$ the majority-spin states are shifted towards lower energies, as compared to the neutral case (dotted line). At the same time, the minority-spin band becomes narrower and is shifted towards higher energies. In particular, one observes a splitting into bonding and anti-bonding orbitals [166], for which the level rearrangements occur in a different way. The bonding orbitals located at lower energies suffer a stronger shift of about 0.6 eV, while the antibonding states shift by about 0.3 eV. The latter smaller change in the position of the antibonding subband suffices for it to cross the Fermi energy and become unoccupied. Moreover, the opposite shifts of the majority- and minority-spin bands increase the magnetic exchange splitting, thus explaining the enhancement of the local magnetic moment. For $q > 0$, the majority- and minority-spin bands show a slight displacement towards lower energies and a decrease of intensity. These changes in the DOS are related to the enhancement of $|E_{\text{int}}|$ found for $q > 0$. Notice that the FM bonding and antibonding orbitals are similarly affected. Here, the local magnetic moments are not significantly modified. Similar changes in the local DOS at the

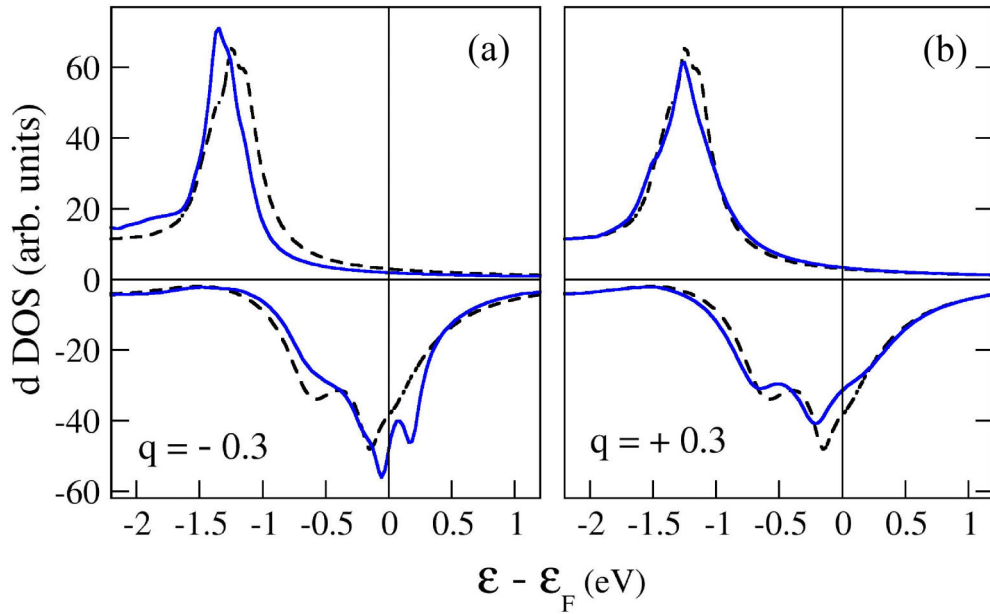


Figure 5.9: Local Co d -electron DOS of a FM dimer [see inset of Fig. 5.7(a)]. Results are given for overlayer charges (a) $q = -0.3$ and (b) $q = 0.3$. The corresponding DOS at the neutral surface ($q = 0$) is also shown (dashed curves) [146].

corresponding Co sites of the AF dimer explain the enhancement of the local moment and the destabilization of this configuration.

In summary, the depletion of electronic density induced by the overlayer charge at the impurity sites strongly affects the spin polarized density distribution and the TM hybridizations, which determine the exchange coupling between magnetic impurities at NN positions (dimers). At larger inter-impurity distances r (e.g., beyond second NNs) the direct electronic hybridizations between the impurities are no longer relevant. The local DOS at the impurity sites is not significantly affected by the relative magnetic coupling between the impurity moments. Hence, the local magnetic moments at the TM atoms are close to the single-impurity values (see Fig. 5.3). A different microscopic mechanism is found to control the exchange energy ΔE between second and third NN atomic impurities. At these intermediate distances, the surface Cu atoms located between the impurities play the central role. In fact, the overlayer charge modifies the local electronic structure of these Cu atoms, which result in most remarkable changes in ΔE including the switching from FM to AF alignment of the impurities and vice versa.

In Fig. 5.7(b), results are given for ΔE between second NN impurities as a function of the overlayer charge q . For $q < 0$ one observes that the FM coupling is preserved and even slightly enhanced by small values of $|q|$. See for example the results for $q = -0.1$ and -0.2 for Co pairs and $q = -0.1$ for Fe pairs. However, a remarkable non-monotonous dependence of ΔE on q is observed for larger $|q|$. The initial decrease of ΔE is followed by a rapid increase for stronger surface charges $q < 0$, which implies a strong destabilization of the FM state. The changes in ΔE are of the order of 20 meV (30 meV) for Co (Fe) impurities. Positive overlayer charges $q > 0.2$ also tend to reduce the strength of the FM coupling. In sum, for the second NN dimer geometry, both overlayer-charge polarities preserve the FM alignment of the impurities ($\Delta E < 0$), although the strength of the effective exchange coupling $|\Delta E|$ is drastically reduced for $|q| \geq 0.3$. In contrast, for impurities at third NN positions [Fig. 5.7(c)] negative overlayer charges destabilize the AF alignment and lead to a switching of the magnetic coupling. On the other side, for $q > 0$ the AF coupling is enhanced by about 10 meV for Co and by 40 meV for Fe.

At the second and third NN distances, the change in the total energy is dominated by the single-particle (SP) contribution

$$E_{\text{SP}} = \int_{-\infty}^{\varepsilon_F} \eta(\varepsilon)(\varepsilon - \varepsilon_F) d\varepsilon = - \int_{-\infty}^{\varepsilon_F} N(\varepsilon) d\varepsilon \quad (5.1)$$

where $\eta(\varepsilon)$ is the electronic DOS and $N(\varepsilon) = \int_{-\infty}^{\varepsilon} \eta(\varepsilon') d\varepsilon'$ is the integrated electronic DOS [111]. Therefore, the magnetic exchange energy ΔE is mainly determined by the differences between the DOS of the FM and AF configurations. However, already at second NNs distance, the local DOS at the impurity sites is not significantly affected by their relative alignment. Consequently, the change in the local DOS at the Cu atoms located between the impurities plays the major role. Appreciable changes in the electronic structure of these atoms are in fact induced by the proximity with the TM impurities, which depend sensitively on the relative orientation of the TM moments. Fig. 5.10 shows the local density of s and p states at the Cu atom located between two Co impurities at third NN positions [see the inset of Fig. 5.7(c)]. Results are given for FM and AF alignments between the impurities for $q = -0.3$ and $q = 0.3$. One observes that for $q = 0.3$ the main peak in the DOS of the Cu atom between AF impurities lies at lower energies than in the case of a FM alignment [see Fig. 5.10(b)]. Therefore, according to the single-particle picture [Eq. (5.1)], an AF coupling is stabilized. This result is in agreement with the AF coupling found for $q \geq 0$. For $q = -0.3$ the peak is shifted towards higher energies with a substantial reduction of its intensity [see

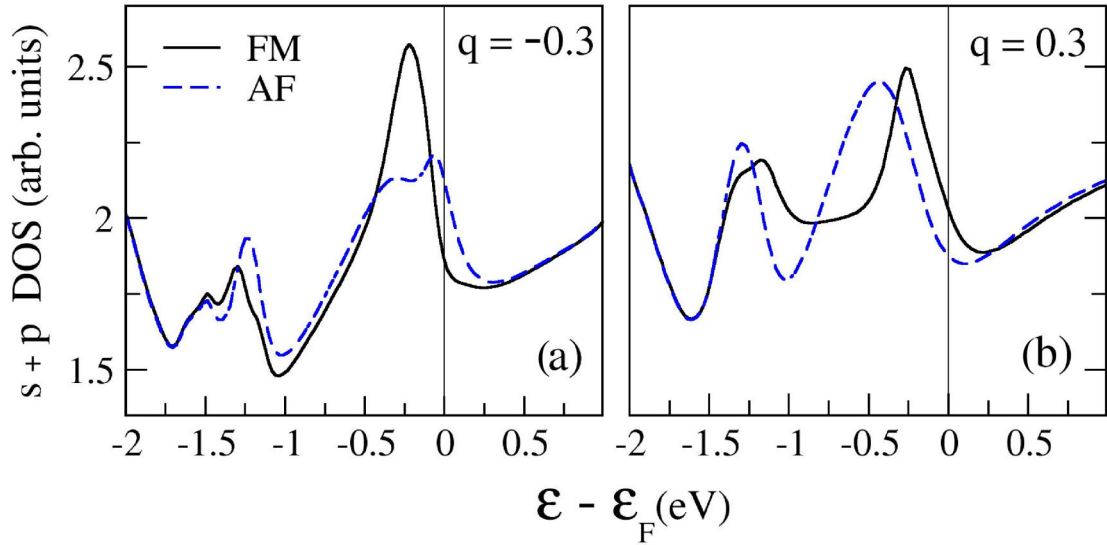


Figure 5.10: Local s - and p -electron density of states at the Cu atom located between two Co impurities at third NN positions [146]. See the inset of Fig. 5.7(c). Results are given for overlayer charges (a) $q = -0.3$ and (b) $q = 0.3$.

Fig. 5.10(a)]. As a consequence, the AF alignment is destabilized and the magnetic coupling between impurities switches to FM ($q \leq 0$).

While the q dependence of ΔE for Fe and Co are quite distinctive at first, second and third NN distances, the behaviors found at larger distances show qualitative similarities [see Figs. 5.7(c)–(e)]. This suggests that for large r the changes of ΔE induced by q are the result of the same microscopic mechanism, namely, the modifications of the delocalized electronic density at the Cu surface and the changes in the scattering properties at the impurities [146]. In order to estimate the contribution of the impurity scattering potentials on ΔE , we have considered an artificial test system: A neutral Cu(111) system ($q = 0$) where the Co surface impurities are represented (i.e., replaced) by the self-consistent local potential of substitutional Co atoms corresponding to systems with overlayer charges $q = \pm 0.3$. In this way we intend to isolate the effects due to the scattering at the impurity potential from the changes in the electronic structure of the substrate, which result from the electric field. For this fictitious arrangement, an approximate value of ΔE for large r can be calculated (non self-consistently) in terms of the change in the single-particle energies for the FM and AF alignment of the impurities [111]. The results show that only slight modifications of ΔE are caused by the change in the impurity potentials alone. In particular, the change of sign of ΔE for $q < 0$ is *not* observed for the test system. Therefore, one

concludes that the changes in the electronic density of the surface is crucial for the distinctive q dependence of ΔE at larger distances. As discussed in Sec. 5.2.1, for negative values of q , the electronic density at the topmost atoms of Cu(111) is reduced up to 0.3 electrons for $q < 0$. For $q > 0$, a large accumulation of electronic density is induced in the vacuum region above the surface. As a result, AF (FM) couplings between impurities is generally favored for $q > 0$ ($q < 0$).

5.3 Conclusions

The magnetic interaction between pairs of substitutional Co and Fe impurities at a Cu(111) surface in the presence of external electric charges has been studied as a function of the inter-impurity distance r . Density-functional calculations show that the EF produced by an accumulation of external charge at the surface can modify the local magnetic properties and interactions of TM impurities. Similar responses to the charging are found for Co and Fe impurities. At the impurity sites, the electric field generated by a charge overlayer induces a displacement of electronic density of minority-spin character. The resulting charge redistribution modifies the local magnetic moments. In particular, the repulsive potential of a negative charge accumulation causes a displacement of electronic density from the surface into the bulk. The consequent reduction of electronic charge at the impurity site leads to a monotonous enhancement of the local magnetic moment as a function of external charge per surface atom q . In contrast, the attraction of surface electronic density caused by an accumulation of positive charge, screens to a large extent its EF keeping the topmost metal layer essentially unmodified. In this case, only a slight reduction of the impurity magnetic moment is induced.

Furthermore, changes in the magnetic exchange energy ΔE between atomic impurities can be induced by an EF through three different microscopic mechanisms. For impurities at nearest neighbors distance, where the exchange interaction is mainly determined by direct electronic hybridization, the magnetic exchange coupling is modified through the reduction of electronic density induced by the EF at the impurity sites. In contrast, the relative magnetic coupling between impurities at second and third NN distances is rather driven by the changes in the local electronic density at the Cu atoms located between them. The EF induced modifications can cause important variations of ΔE including the switching between a FM and an AF alignment of the impurities. At larger distances, the RKKY exchange interaction mediated by the substrate determines the coupling between impurities. The external EF can cause

changes in the delocalized electronic density of the Cu surface which modify the scattering of the surface states and induce variations of ΔE in the order of 10 meVs. Notably, a contrasting behavior of the metallic screening is observed depending on the polarity of the overlayer charge, together with a non-monotonous behavior as a function of q .

This results open a new perspective in the development of methods to control the internal and collective magnetic properties of surface nanostructures.

Electric-field modulated exchange coupling within and between magnetic clusters on metal surfaces: Mn dimers on Cu(111)

The potential use of external electric fields (EFs) to control the magnetic order of nanostructures is particularly important for applications in high-density storage devices [129, 133]. A recent achievement towards this aim is the switching between the ferromagnetic (FM) and antiferromagnetic (AF) phases of ultrathin Fe layers demonstrated by Gerhard *et al.* [117] using the electric field of a scanning tunneling microscope. This effect is achieved by taking advantage of the structural instability between the AF face-centered cubic and the FM body-centered cubic phases of Fe thin films. This study constitutes a promising example of magnetoelectric effects in metals. In general, an EF is screened by the conduction electrons at the topmost one or two atomic layers of a metallic surface. However, in low-dimensional systems, where the surface to volume ratio is large, the charge density rearrangements caused by an EF are expected to cause strong modifications of the electronic properties of the system [23, 148–150]. In particular, the field-induced redistribution of spin polarized *d*-electrons at the Fermi energy can significantly affect the magnetic behavior of

transition metal (TM) nanostructures. It is the goal of this chapter to explore this challenging physical problem from a theoretical perspective.

Surface magnetic nanostructures are particularly interesting for future technological applications in atomic scaled devices [24]. Still, only few works have been so far devoted to investigate the effect of an applied EFs on the electronic properties of TM supported nanoparticles [23, 146]. Most of the recent studies have been devoted to the investigation of properties such as structure, adsorption energy and, to a small extent, to the modification of the intrinsic magnetic properties [23, 148–150]. In this context, it has been shown that applied EFs can induce switching between different magnetic states in multistable low-dimensional nanostructures [23, 134, 167–169]. One of these systems are polar magnetic molecules, where the Stark effect competes with the super-exchange interaction [167]. Electrically induced magnetic switching has been demonstrated experimentally by Loth *et al.* By means of a spin-polarized tunneling current they achieved the switching between the two Néel states of anti-ferromagnetic Fe nanochains deposited on Cu₂N/Cu(100) [134]. From a theoretical perspective, Negulyaev *et al.* investigated how EFs can induce a switching between the different magnetic states of an isolated Mn dimer on Ag(001) and Ni(001) [23]. In this case, the small energy difference between the FM and AF states of Mn₂ renders the substrate density distribution crucial for determining the ground-state magnetic order [23, 170, 171]. This work also shows that the EF effects are at least twofold. On the one hand, the EF modifies the electronic structure of the dimer and, on the other hand, it affects the electronic coupling between the cluster and the substrate. These studies highlight the importance of the substrate on the properties of the adsorbates and its influence on the response of the systems to an applied EF.

The previous studies have provided a useful insight on the consequences of applying external EFs on the magnetic properties of isolated particles [148–150]. However, very little is still known about the possibility of tuning the exchange interactions between magnetic clusters on surfaces. Since the EF induces changes in the spin polarized electronic density of the magnetic cluster and the metal surface, it should also provide a means of controlling the magnetic coupling between two or more supported nanoparticles. This effect is to be expected at the close-packed surfaces of noble metals, where changes in the dispersion of the electronic surface states have been reported [138, 139]. The surface-state electrons are responsible for the long-ranged RKKY interaction between nanostructures deposited on metal surfaces [33, 155, 156, 172–175]. In the case of magnetic particles, the RKKY interaction gives rise to a magnetic exchange coupling between neighboring particles, which con-

trols the relative magnetic orientation between them [25, 32, 47, 48, 176]. We have shown in Chap. 5, that the displacement of electronic density at metal surfaces has the potential to modify and eventually reverse the substrate-mediated interactions between magnetic impurities at relatively large distances [146]. Therefore, applied EFs can offer an interesting possibility to manipulate the magnetic exchange coupling within between supported TM nanostructures. It is the purpose of this Chapter to investigate and quantify the possibility of manipulating the magnetic couplings of surface nanostructures by means of applied external EFs.

In the context of electrically controlled magnetic coupling, the case of Mn dimers on Cu(111) is particularly interesting. On the one side, the magnetic multistability of Mn_2 has already been observed on other surfaces [23, 179]. This suggests the use of EFs to reverse the internal magnetic order. On the other side, the substrate-mediated exchange coupling between particles is expected to depend on their magnetic state (i.e., FM or AF). Thus, the manipulation of the coupling between the dimers can be presumably achieved either by inducing a switching of the magnetic state of the dimers or by directly affecting the surface electrons responsible of the substrate-mediated interaction [168]. The remainder of the chapter is devoted to understanding the magnetic exchange coupling within and between Mn dimers supported on Cu(111) as a function of applied external EFs.

6.1 Computational details

Self-consistent density-functional calculations of the magnetic couplings of Mn dimers on Cu(111) as a function of applied EF have been performed using the GF-KKR method described in Sec. 3.2. For metallic systems, the effect of applied external EFs can be treated within the KKR perturbation approach to crystal surfaces [138]. The surface is modeled by replacing a slab of bulk crystal with vacuum spheres. The resulting configuration is conformed by two half-infinite crystals and a vacuum region bounded by the metallic surfaces. An homogeneous external EF is simulated by introducing a two-dimensional layer of fixed point charges q inside the vacuum slab placed above the considered surface [138]. In such an arrangement, the resulting EF generated by the external charges is effectively screened at both metal surfaces and is, therefore, confined to a finite perturbation region. Positive (negative) values of charge q correspond to an inwards (outwards) direction of the EF with respect to the crystal

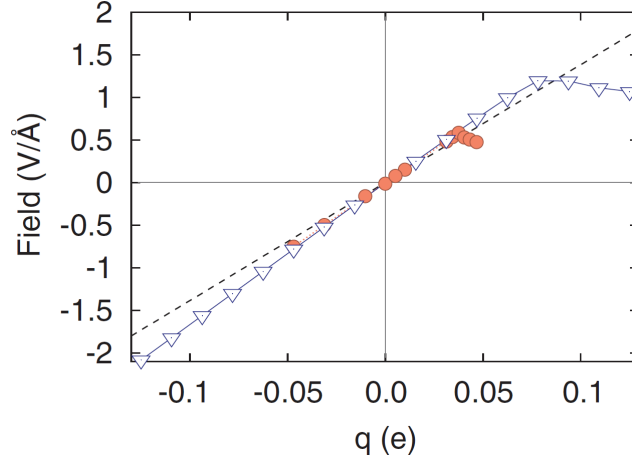


Figure 6.1: Effective EF strength as a function of the generating point charges q . Triangles correspond to a five-layer-thick vacuum slab with charges q located in the third layer above the crystal surface. The dashed line shows the field of a uniformly charged plane (Figure taken from Ref. [138]).

surface. Notice that the largest possible value of $q > 0$ (or inwards field strength) is limited by the work function of the metal surface. Excessively large values can lead to the transfer of electrons into the vacuum and its accumulation around the external charges generate the EF.

In the present study, the Cu(111) surface has been modeled by replacing a six-layer-thick slab of Cu-bulk potentials with vacuum spheres. The experimental Cu lattice constant $a = 3.615 \text{ \AA}$ is used and the corresponding atomic positions of the substrate are kept fixed for all considered configurations of the adclusters. The layer of point charges q generating the EF is located inside the vacuum slab at the atomic positions corresponding to the third layer above the surface. The vertical distance of the charges respect to the crystal surface is then about 6.3 \AA . Values of q in the range $|q/e| < 0.08$ have been considered [138]. For the corresponding strength of EF as a function of q see Fig. 6.1 [138].

The Mn dimers are located on top of the surface at perfect Cu lattice positions. The magnetic exchange interactions have been studied performing self-consistent calculations for different magnetic arrangements of two deposited dimers in the FM and AF states. The exchange energy $E_x = E_{\text{FM}} - E_{\text{AF}}$ accounts for the energy difference between the FM and AF order within the dimer. For each magnetic state of the dimers (FM or AF) the dimer-dimer exchange interaction energy is given by $\Delta E = E_{\text{P}} - E_{\text{AP}}$ where the total energies E_{P} and E_{AP} correspond to the parallel (P) and antiparal-

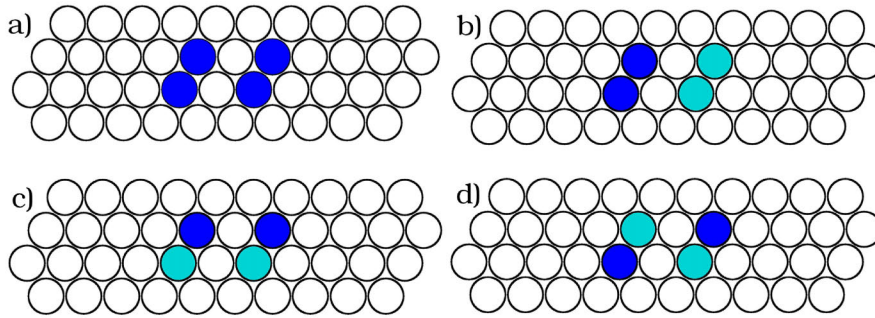


Figure 6.2: Illustration of the magnetic arrangements of a pair of dimers at second NN positions along the $[1\bar{1}0]$ direction of the (111) fcc surface. Dark (light) colored circles indicate atoms having up (down) magnetic moments. The subfigures (a) and (b) illustrate the parallel and antiparallel coupling between FM dimers, while (c) and (d) correspond to the parallel and antiparallel coupling between AF dimers.

parallel (AP) alignment of the magnetic moments of the two dimers with respect to each other (see Fig. 6.2). The values of ΔE have been calculated for interdimer separations corresponding to up to eighth nearest neighbors (NNs) along the $[1\bar{1}0]$ and $[\bar{1}\bar{1}2]$ directions of the Cu(111) surface.

6.2 Results

6.2.1 The clean Cu(111) surface

It is useful to begin the discussion by considering the effect of external EFs on the clean Cu(111) surface. Fig. 6.3 shows the local electronic density of s (p) states calculated for various strengths of the EF at the topmost Cu layer and at the vacuum spheres right above the surface. Black curves correspond to the local DOS in the absence of EF. At about 0.7 eV below ε_F the bottom of the surface band appears as a step-like feature. The external EF modifies the position and intensity of the band. Indeed, the density of surface states at the interface is higher than that of bulk electrons. Thus, the EF-induced changes in the LDOS of the topmost Cu layer concern mainly to modifications of the surface band. Negative EFs enhance the vacuum potential barrier and, consequently, shift the band towards higher energies [see Fig. 6.3(b)]. At the same time, the EF hinders the spill-out of surface-state electronic density. Therefore, the LDOS is reduced in the vacuum region above the surface [Fig. 6.3(c)]

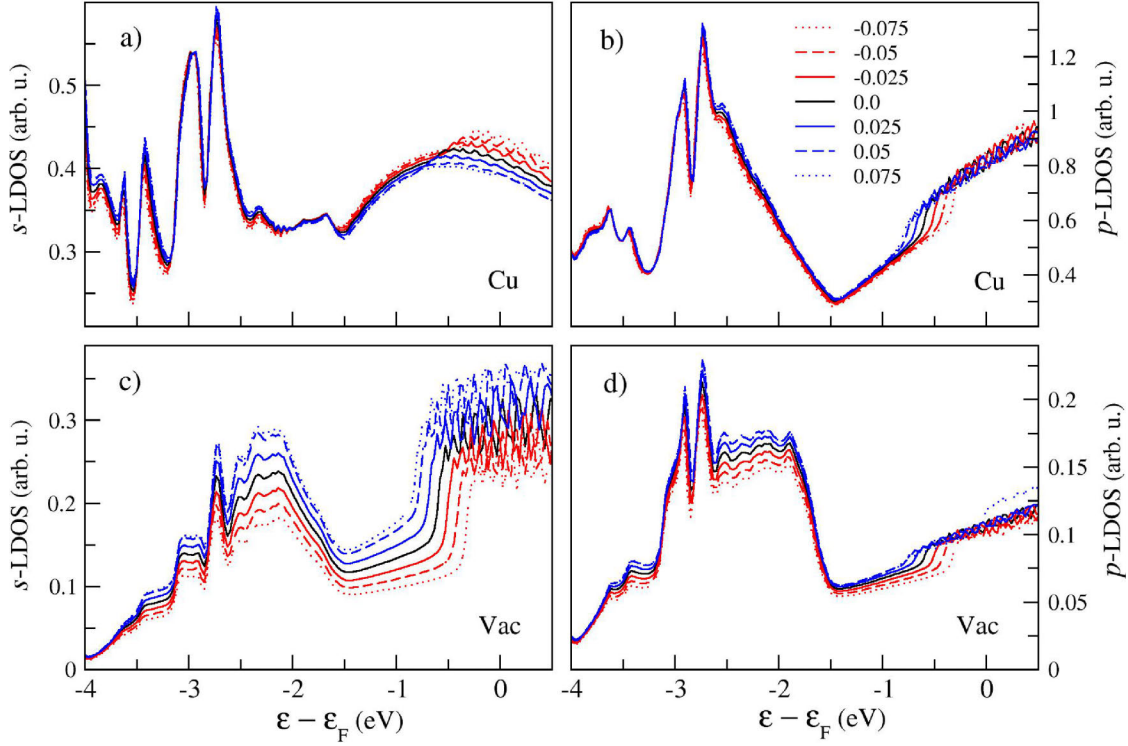


Figure 6.3: Local electronic density of s - (p -) states at the topmost Cu(111) crystal layer [(a)-(b)] and first vacuum layer above the surface [(c)-(d)]. Curves are shown for different strengths of external EF corresponding to the values of q given in the inset.

and (d)]. On the contrary, positive EFs shift the surface band towards lower energies slightly reducing its density at the topmost Cu layer and enhancing it at the vacuum above the surface. These changes in the electronic structure and density distribution are expected to affect the Fermi wavelength of the surface states, since they modify the energy of the bottom of the surface-state band and the effective mass of the surface electrons [138]. Consequently, the EF should affect the RKKY interactions responsible of the long-ranged magnetic exchange coupling between the magnetic clusters. In addition, the EF-induced modifications of the surface electronic structure could also affect the adsorption energy of the clusters.

6.2.2 Isolated Mn_2 on Cu(111)

As a next step, before discussing the interaction between deposited clusters, it is important to consider the case of an isolated Mn dimer and the effect of an external EF on its ground-state magnetic order. In the absence of EF, the AF configuration

is found as the most stable magnetic order. The FM state has a 30 meV higher energy. This result contrasts with the FM ground-state found by Negulyaev *et al.* for Mn₂ on Ag(001) [23]. The difference is remarkable but not quite surprising, since the behavior of magnetic impurities in metallic environments is known to depend critically on the properties of the host, particularly on the density of states at the Fermi energy and the strength of the 3*d*-metal hybridizations [166]. Additionally, the bond length plays an important role in the stability of the magnetic order of Mn₂. In the present calculations, the Mn atoms are located at perfect Cu-lattice positions (see Sec. 6.2.5). The bond length of the dimer corresponds therefore to the Cu NN distance $d = 2.55 \text{ \AA}$, which has been found to favor the stability of the AF state in other local environments [23, 170, 171, 177, 178, 180]. Considering the well known sensitivity of the internal magnetic order of Mn₂, it is important to take into account both FM and AF dimer configurations in order to assess how the magnetic interactions between dimers depend on their internal magnetic state.

Mn dimers deposited on Cu(111) show saturated local spin moments of about $4.1 \mu_B$, irrespectively of their internal magnetic configuration (FM or AF). Under the considered values of external EF ($|E| < 1.5 \text{ V/\AA}$) only slight enhancements of these local spin moments are induced ($|\delta\mu| < 0.1 \mu_B$). Interestingly, the local moments increase monotonously with an increasing EF for both inwards and outwards directions of the field. This enhancement is similar in both FM and AF states of the dimer [181].

In contrast, the effect of the external EF on the magnetic exchange energy is quite remarkable. Our results for E_x are shown in Fig. 6.4(a) as a function of q [181]. For the sake of comparison, note that $|q| = 0.05$ corresponds to an EF of about 1.0 V/\AA (see Fig. 6.1) [138]. The energy difference $E_x = E_{\text{FM}} - E_{\text{AF}}$ between the magnetic states of the dimer is strongly enhanced for positive q (i.e., inwards EF), while it decreases and eventually changes sign for a sufficiently strong negative q (i.e., outwards EF). For an inwards EF ($q > 0$), E_x grows up to 70 meV for $q = 0.05$. For outwards EF ($q < 0$), E_x decreases and changes sign for $q = -0.05$. This implies that the FM state becomes the ground-state configuration of the dimer. The relative stability with respect to the AF configuration remains at first rather weak: $E_x = -0.35 \text{ meV}$ for $q = -0.05$. However, stronger outwards EFs enhance the stability of the FM configuration up to $E_x = -13 \text{ meV}$ for $q = -0.1$ [see Fig. 6.4(a)] [181]. This trend is in agreement with the behavior found for Mn₂ on Ag(001) [23]. One concludes that external EFs are able to reverse magnetic exchange energy barriers of the order of 50 meV in TM nanoparticles.

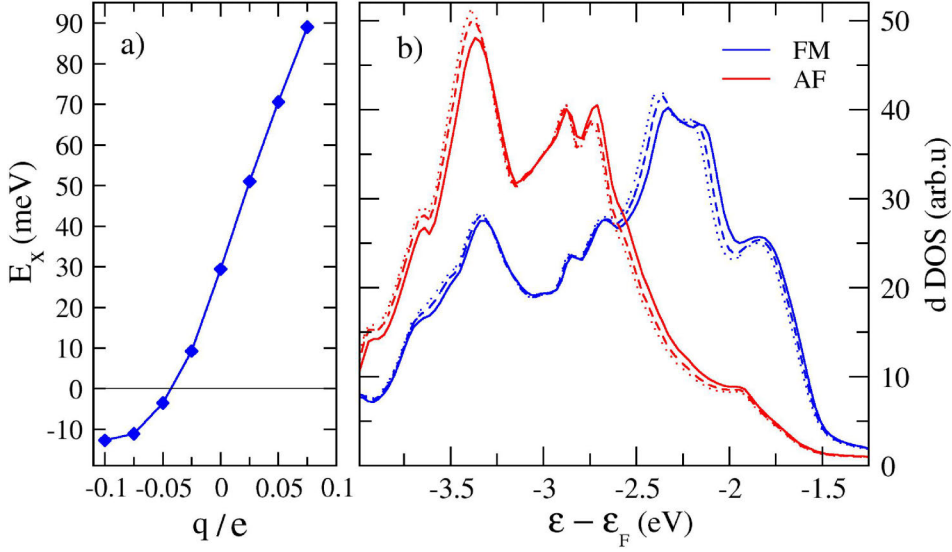


Figure 6.4: (a) Exchange energy difference $E_x = E_{\text{FM}} - E_{\text{AF}}$ between the FM and AF state of a Mn dimer as a function of the EF source charge q . Positive (negative) values of E_x correspond to an AF (FM) ground-state. (b) Local density of the majority-spin d -states at a Mn atom in FM (blue) and AF (red) Mn_2 . Full, dashed and dotted curves correspond to $q = +0.05, -0.05$ and 0.0 respectively [181].

For $-0.05 < q < 0.1$ an approximately linear behavior of E_x as a function of q is observed. However, after a rapid decrease in this range, E_x tends to level off for stronger negative q . The contrasting behavior for outwards and inwards field is probably a consequence of the different type of charge redistribution occurring at the metal surface and the deposited dimer. For outwards EFs the electronic density is shifted into the bulk tending to positively charge the deposited Mn_2 and eventually reducing to some extent the Mn d -orbital occupation. It is interesting to note that the enhancement of stability of FM order in Mn_2 with reduced electronic density is consistent with previous results obtained for Mn_2^+ in the gas phase, which was found to be FM [177]. In contrast, inward fields enhance the density of surface electrons around the dimer, which favors an AF order. In general, the precise asymmetric behavior of the EF response of the system arises from the electronic coupling with the surface and is therefore expected to be substrate dependent.

The effect of the EF on the magnetic state of the dimers can be understood from a local point of view by analyzing the changes in the electronic density of states. The saturated values of the local magnetic moments indicate that the minority-spin states of Mn atoms lie mostly above the Fermi energy ϵ_F . Therefore, their contribution to

the EF response is not expected to be significant. Fig. 6.4(b) shows the local density of majority-spin d -states (LDOS) at a Mn atom in the FM and AF configuration of the dimer [181]. One observes that the bandwidth of the FM state are broader than in the AF case, indicating that electrons in a FM state are less localized and extend farther into the vacuum [23]. Thus, one expects that the FM dimer to be more sensitive to the EF. An outgoing EF ($q < 0$) shifts the curves of both states to slightly lower energies. A somewhat larger shift is observed in the peak located at about -2.2 eV for the FM state of the dimer. The stabilization of the FM ground-state could be related to this small difference in the shifting [23].

6.2.3 Magnetic state and coupling between dimers at short distances

In order to quantify the magnetic interaction between a pair of dimers, we consider the magnetic arrangements shown in Fig. 6.2. For each magnetic state of the dimer (FM or AF), the parallel (P) or an antiparallel (AP) alignment of the magnetic moments of one dimer respect to the other is investigated. The energy difference between these two configurations $\Delta E = E_P - E_{AP}$ gives a measure of the dimer-dimer exchange coupling.

Fig. 6.5 shows the magnetic exchange energy ΔE between two FM (AF) Mn dimers on Cu(111) as a function of the interdimer distance r [181]. Notice that different scales are used for first NN dimer separation (left scale), and for second, third and fourth NN dimers separation (right scale). Positive (negative) values of ΔE correspond to an energetically favorable antiparallel (parallel) alignment between the magnetic moments of the two dimers. First of all, one observes that ΔE strongly depends on the internal magnetic state of the dimers. In fact, at several distances the sign of ΔE is different for FM and AF dimers, which implies a different relative alignment between the Mn_2 . See, for example, the case of dimers along the [112] direction for distances beyond NNs [Fig. 6.5 (right)]. For a pair of AF dimers (triangles), the positive values of ΔE correspond to a favorable antiparallel alignment, while the parallel alignment ($\Delta E < 0$) is preferred between FM dimers (circles). As it will be shown later, this result can be understood as a consequence of the different scattering of majority-spin and minority-spin electrons, which entails the magnetic nature of the interaction. In a similar way, the interference between scattered surface electrons is at the origin of the dependence of ΔE on the geometry and relative orientation of

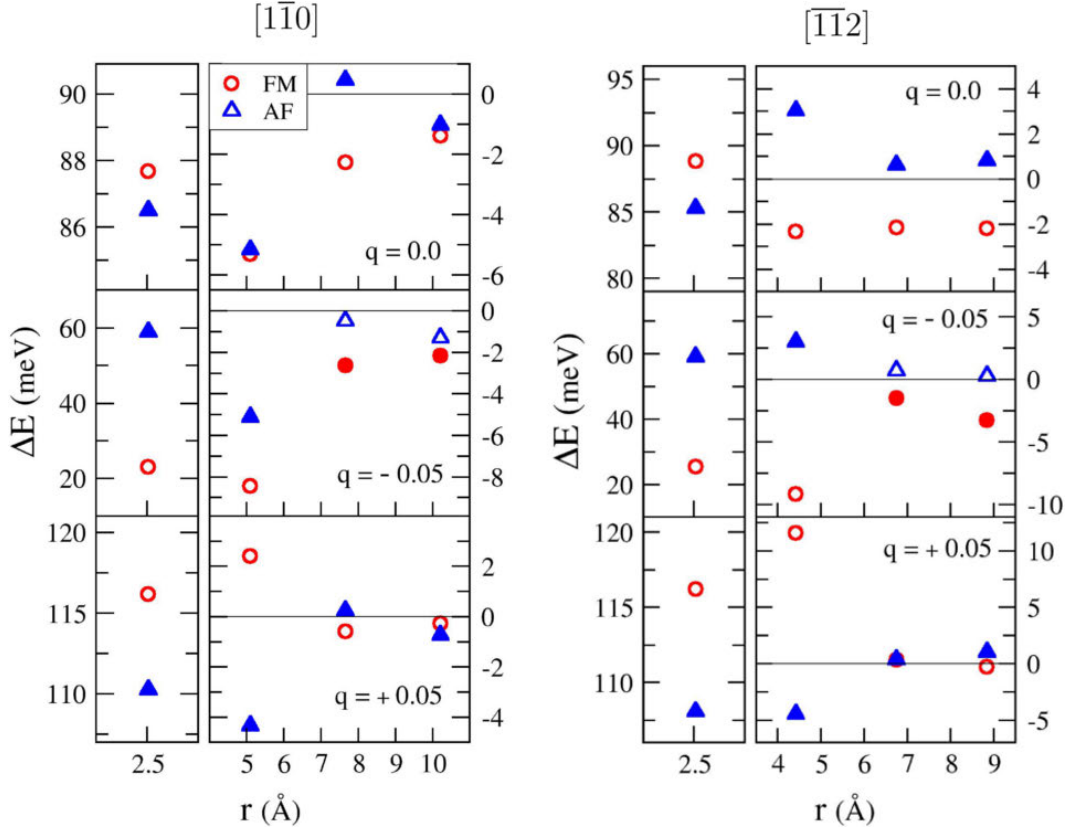


Figure 6.5: Exchange coupling energy $\Delta E = E_P - E_{AP}$ between two Mn dimers as a function of the interdimer distance r [181]. Both FM (circles) and AF (triangles) states of the dimers are considered [See Fig. 6.2]. Full symbols indicate the ground-state magnetic order within Mn_2 . Results are given for $q = 0$, $q = -0.05$ and $q = 0.05$. The left and right figures correspond to dimers along the $[1\bar{1}0]$ and $[\bar{1}\bar{1}2]$ directions of Cu(111).

the dimers [46, 48, 155]. These effects are revealed in Fig. 6.5, where the difference between the results for dimers along the $[\bar{1}\bar{1}2]$ and $[1\bar{1}0]$ directions are shown. The dependence of ΔE on the magnetic state and relative orientation between the dimers remains significant even at larger distances ($r > 10\text{\AA}$). It should be noted that these properties are specific to interacting clusters, in contrast to the case of single adatoms. They become essential for the analysis of the interparticle magnetic coupling and its response to an external EF.

Let us now analyze how the interparticle coupling and the EF affect the internal ground state magnetic order of Mn_2 . In the absence of external field ($q = 0$), the AF state remains the ground-state within Mn_2 for all interparticle distances r (full triangles in Fig. 6.5). In fact, for the first NN distance between the dimers—this cor-

responds to a diamond-shaped tetramer— the AF-AP configuration [see Fig. 6.2(d)] is nearly 0.2 eV more stable than the FM-P state [see Fig. 6.2(a)]. At such a short distance, both the interparticle exchange energy ΔE and the intra-particle exchange energy E_x are dominated by the direct electronic hybridization between Mn atoms. Therefore, a tendency to AP coupling is not surprising. The AF dimers with AP alignment show the largest number of antiparallel NN moments and are therefore energetically favored. In addition, the direct hybridization causes slight changes in the local magnetic moments μ_i of Mn. In the AF-AP configuration, the calculated local spin moments are $\mu_i = 4.0\mu_B$ and $-3.6\mu_B$, while in the FM-P case one finds $\mu_i = 3.9\mu_B$ and $3.7\mu_B$. In both configurations the largest moments correspond to the less coordinated atoms.

In the presence of an outgoing EF ($q = -0.05$), the FM order found to be the ground-state within an isolated dimer, does not hold for a pair of dimers at the shortest separation distances (see full symbols in Fig. 6.5). In contrast, the AF order within Mn_2 is the ground-state of a *pair of dimers* at first and second NNs distance. This holds for both considered directions on the Cu(111) surface. In order to discuss this result in further detail, we show in Fig. 6.6 the results for ΔE as a function of q for a pair Mn dimers along the $[1\bar{1}0]$ direction of Cu(111) [181]. Here one observes that the EF induced changes in ΔE also depend on the magnetic state of the dimers. In general, the EF effects are stronger for pairs of FM dimers. For dimers at NN positions [Fig. 6.6(a)] the changes in ΔE as a function of q are of the order of 0.1 eV. Positive values of ΔE correspond to an antiparallel alignment between the dimers. An inwards (outwards) EF causes an increase (decrease) of ΔE for both FM and AF pairs. The AF order within Mn_2 is found to be the ground-state magnetic order (full diamonds). This is true even for values of $q < 0$ for which the FM state yields the ground state of an isolated dimer. At this minimal distance ΔE involves an interplay between various NNs interactions, which are dominated by the direct electronic hybridizations. Thus, the strength of the interaction is about one order of magnitude larger than at any other interparticle distance r .

For dimers at the second NNs distance [Fig. 6.6(b)] the relative alignment between the dimers is in general parallel ($\Delta E < 0$). Here, the energy differences between the configurations considered in Fig. 6.2 can be regarded as the result of two NN and two second-NN interactions. For the largest considered negative value of $q/e = -0.075$ the overall ground-state configuration corresponds to a pair of FM dimers. This result is in agreement with the FM order found for the isolated dimer. However, notice that a different behavior is found for $q/e = -0.05$. Only for larger r the FM ground state

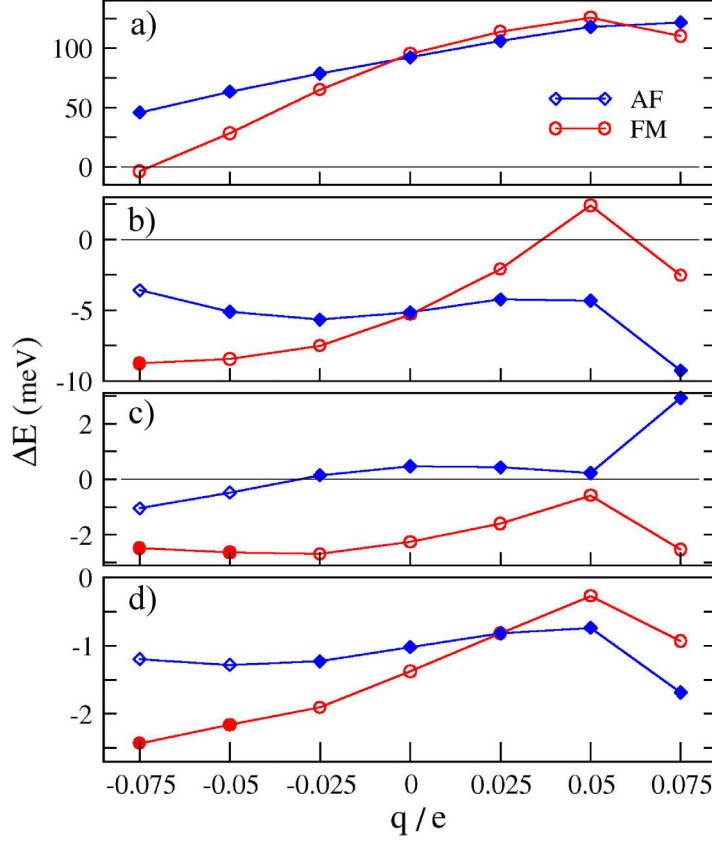


Figure 6.6: Interparticle exchange coupling energy ΔE between two FM (circles) and AF (diamonds) Mn dimers as a function of the EF source charge q [181]. Full symbols indicate the ground-state magnetic order within Mn_2 . Results are shown for dimers at the (a) first-, (b) second-, (c) third- and (d) fourth-NN distances along the $[1\bar{1}0]$ direction of the Cu(111) surface. Both FM (circles) and AF (diamonds) states of the dimers are considered.

within Mn_2 is recovered for both $q/e = -0.05$ and -0.075 [Fig. 6.6(c) and (d)]. A similar behavior is observed for a pair of dimers along the $[\bar{1}\bar{1}2]$ direction. However, in this case the FM order within Mn_2 is recovered only for r beyond second NN interdimer distances also for $q/e = -0.05$. These differences are a consequence of the different orientations of the dimers, as observed in the context of Fig. 6.5. The separation distance between clusters at second-NN positions is shorter along the $[\bar{1}\bar{1}2]$ direction than in the case of the $[1\bar{1}0]$ direction. Thus, a stronger difference in ΔE for FM and AF dimers is found along the former. Moreover, these results reveal a competition between the interdimer interactions and the EF effects, suggesting that at very short distances the dimer-dimer interactions are large enough to dominate over the charge redistributions induced by the EF. Beyond second NN distances, the

importance of the dimer-dimer interactions decreases and the FM state, which is the ground-state of the isolated Mn_2 , yields the ground-state of the ensemble.

6.2.4 Long range substrate-mediated magnetic interactions

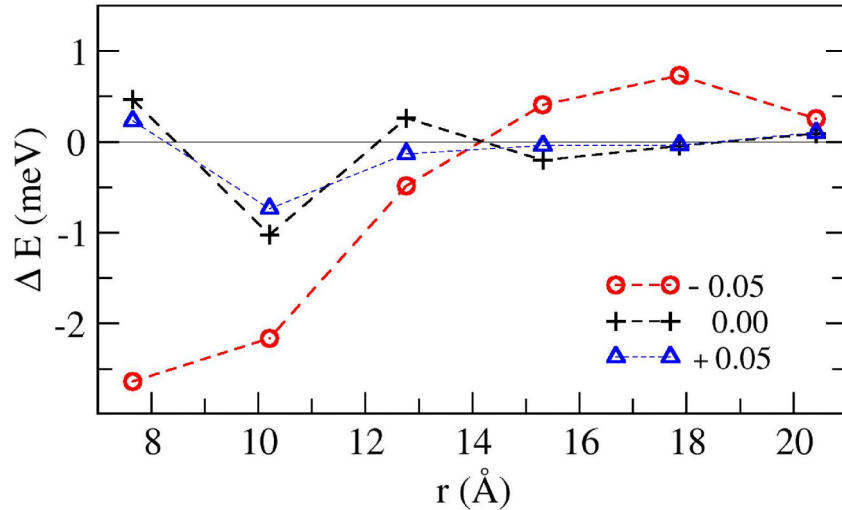


Figure 6.7: Interparticle exchange coupling energy $\Delta E = E_P - E_{AP}$ between two Mn dimers in the ground-state as a function of the interdimer distance r [181]. Results are given for the ground-state magnetic order within Mn_2 and for EF source charges $q/e = 0.0$ and $q/e = \pm 0.05$.

At relatively large distances ($r \gtrsim 7 \text{ \AA}$), the magnetic ground-state of the dimers is the same as for an single dimer (i.e., AF for $q/e > -0.05$ and FM for $q/e \leq -0.05$). The interaction between pairs of dimers is mediated by the surface electrons. Fig. 6.7 shows $\Delta E = E_P - E_{AP}$ for two Mn dimers in their ground state as a function of the interdimer distance r along the $[1\bar{1}0]$ direction of the Cu(111) surface [181]. Positive (negative) values of ΔE correspond thus to a favorable antiparallel (parallel) alignment between the magnetic moments of the two dimers. In the absence of external EF and for inward fields the dimers are AF. In these cases ΔE shows similar RKKY-like oscillations as a function of r (see Fig. 6.7 for $q = 0$ and $q = 0.05$). A similar oscillatory behavior is observed between dimer pairs along the $[\bar{1}\bar{1}2]$ direction of the surface. The oscillations differ from the typical substrate-mediated interaction between single adatoms due to the specific dimer geometry and orientation [48, 155]. Under outwards applied EF ($q/e = -0.05$) remarkable changes in the values and sign of ΔE are observed (see Fig. 6.7). This is a consequence of the change in the ground-

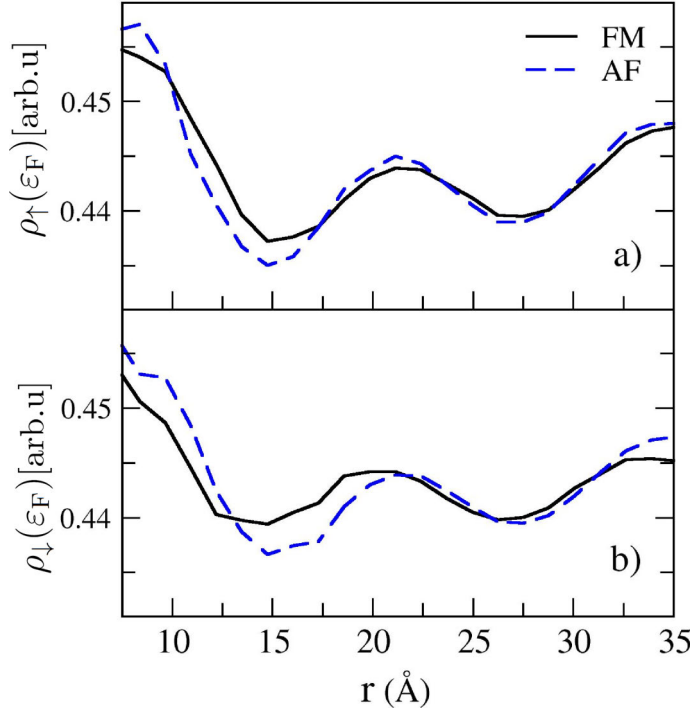


Figure 6.8: Spin-polarized local density of states $\rho_{\sigma}(\varepsilon_F)$ at the Fermi energy ε_F in the vicinity of a FM Mn_2 (solid curves) and an AF Mn_2 (dashed curves) on Cu(111). Results are given for points located at 2.1\AA above the surface as a function of the distance r to the Mn dimer. Subfigure (a) corresponds to majority-spin states and (b) to minority-spin states [181].

state magnetic order within Mn_2 , from AF for $q = 0.0$ to FM for $q = -0.05$, which directly affects the scattering of the spin-polarized electrons at the Cu surface and the resulting magnetic component of the RKKY interaction.

Furthermore, one finds that the effect of the EF is stronger for pairs of FM Mn_2 . For these dimers, the outwards EFs shift the curves of ΔE towards negative values for $r < 14\text{\AA}$, thus, stabilizing further the parallel alignment between them. On the contrary, inwards applied EF shifts ΔE towards the antiparallel configuration. At large distances ($r > 14\text{\AA}$), the dimer-dimer coupling is predominantly antiferromagnetic and the strength of ΔE is enhanced (decreased) for outwards (inwards) fields. In the case of AF dimers the interparticle interaction energy ΔE is much less affected by the EF. The curves obtained for other values of q follow the same trends. The stronger effect of the EF on the FM Mn_2 can be related with the higher degree of delocalization of electronic density in this configuration, which extends farther into the vacuum, as observed from the broader bandwidth in Fig. 6.4(b). Moreover, if

the EF points outside the surface, the spill-off of electronic density is reduced and a parallel alignment of the magnetic moments of the two Mn_2 is favored. In contrast, inwards EFs favor an antiparallel alignment. This demonstrates again the remarkable possibilities of using applied external EFs as a tool for the tuning of long-range exchange interactions between magnetic clusters on metal surfaces.

Further insight on the microscopic origin of the exchange couplings is obtained by analyzing the electronic structure from a local perspective. Fig. 6.8 shows the spin-polarized electronic density of states at the Fermi energy at the vacuum region 2.1 \AA above the surface as a function of the distance to a single Mn dimer. Results corresponding to both FM and AF orders within the dimer are shown [181]. The curves display oscillations with a period $\lambda_F/2 \approx 15 \text{ \AA}$ caused by the quantum interference of scattered surface electrons [33]. Moreover, one observes that for majority-(minority-) spin electrons the pattern of standing waves arising from the AF dimer is shifted towards shorter (larger) distances as compared to the FM case. This shift is responsible for the dependence of ΔE on the internal magnetic order of the dimers. The spin dependence of the surface-electron scattering is responsible for the magnetic coupling and for the dependence of ΔE on the magnetic state of the interacting dimers.

6.2.5 Structural relaxation effects

The substrate-mediated interaction is caused by the scattering of delocalized surface electrons. Thus, structural relaxations within and nearby the dimers are not expected to have a strong influence on the long-ranged coupling between them [182,183]. However, local relaxations can be important at very short separation distances, in particular for the internal ground-state magnetic order of the Mn dimers, which are known to present magnetic bistability [23,177,182]. The effects of structural relaxation on the magnetic properties of Mn_2 on Cu(111) have been studied using *VASP* (see Sec. 3.1). Self-consistent *ab-initio* calculations have been performed using a five-layer thick crystal slab defined in a supercell of dimension 6×4 surface atoms to model the Cu(111) surface. A cutoff energy of 450 eV has been used for the plane-wave expansion of the wavefunctions. A set of $3 \times 3 \times 1$ k -points was employed for the computation of all integrals in the BZ. This setup constitutes a good compromise between numerical accuracy and computational effort. The Mn dimers have been located symmetrically on both sides of the slab (see Fig. 6.9). Such an arrangement avoids spurious dipolar contributions to the energy resulting from the adcluster induced surface polarization

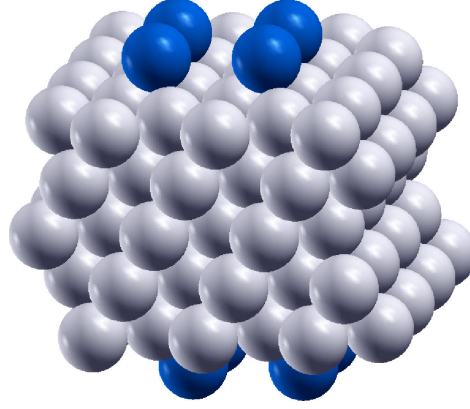


Figure 6.9: Illustration of the unit supercell used to model a pair of Mn_2 on $\text{Cu}(111)$. Mn atoms (dark spheres) are located on both sides of a five-layer thick $\text{Cu}(111)$ slab (light spheres) containing 6×4 atoms.

and the periodic boundary conditions. The calculations have been performed for the collinear magnetic states considered in Sec. 6.2.3 for a single Mn dimer and a pair of dimers at second NN positions along the $[\bar{1}\bar{1}2]$ direction (see Fig. 6.9). The atomic positions of the Mn atoms and the two topmost layers of the Cu surface have been relaxed self-consistently by using the conjugate-gradient algorithm until the forces exerted on each atom are smaller than $0.01 \text{ eV}/\text{\AA}$. Values for E_X and ΔE for the unrelaxed and optimized structures have been obtained. For the sake of comparison and in order to assess the role of exchange and correlation effects, the calculations have been performed within the LDA and the GGA approximations to density functional theory.

The results obtained within the GGA approach are summarized in Table. 6.I. For an ideal [i.e., non-relaxed (NR)] geometry, the AF ground-state of a single Mn dimer is found at an energy about 90 meV below the FM state. This is very good agreement with the 95 meV found within LDA approach. Moreover, both results are in qualitative agreement with the KKR result predicting an AF ground state, although the value of $E_X^{KKR} = 30 \text{ meV}$ is significantly smaller. The local magnetic moments $\mu_{\text{Mn}}^{\text{FM}} = 4.08\mu_B$ and $\mu_{\text{Mn}}^{\text{AF}} = 4.13\mu_B$ are in good agreement with the KKR result $\mu_{\text{Mn}} = 4.1\mu_B$ found in both configurations. After optimization of the atomic positions, the bond length in the FM dimer increases by approximately 0.2 \AA , while for the AF dimer the expansion is smaller (0.1 \AA). In addition, the distance between the dimer and the substrate is reduced by less than 0.1 \AA for both configurations. As a consequence of these relaxations, the exchange energy E_X between the FM and AF

Table 6.I: Calculated local magnetic moments μ_{Mn} , dimer bond length d_b , and magnetic exchange energies $E_X = E_{\text{FM}} - E_{\text{AF}}$ and $\Delta E = E_{\text{P}} - E_{\text{AP}}$. Results are shown for an isolated Mn_2 and pairs of Mn_2 along the $[\bar{1}\bar{1}2]$ direction of the $\text{Cu}(111)$ surface occupying ideal and optimized positions.

Single Mn_2	FM (NR/R)	AF (NR/R)	E_X (meV)
μ_{Mn} [μ_B]	4.08 / 4.13	4.13 / 4.14	93.5 / 52.0
d_b [\AA]	2.55 / 2.77	2.55 / 2.67	
FM Mn_2	P	AP	ΔE (meV)
μ_{Mn} [μ_B]	4.08 / 4.14	4.08 / 4.13	11.2 / 13.8
d_b [\AA]	2.55 / 2.77	2.55 / 2.75	
AF Mn_2	P	AP	ΔE (meV)
μ_{Mn} [μ_B]	4.13 / 4.13	4.13 / 4.13	11.0 / 9.3
d_b [\AA]	2.55 / 2.65	2.55 / 2.65	

states decreases to nearly half of its value, namely to $E_X \simeq 52$ meV. The local magnetic moments are not significantly modified by the structural changes. Similar results are obtained within the LDA approximation. However, in this case, shorter bond distances $d_b = 2.69 \text{\AA}$ ($d_b = 2.50 \text{\AA}$) are found for the FM (AF) dimer, accompanied by a smaller change of the exchange coupling: $E_X \simeq 95$ meV for the unrelaxed and $E_X \simeq 83$ meV for the relaxed geometries.

For a pair of FM dimers at unrelaxed positions, the calculated magnetic exchange energy $\Delta E \simeq -11$ meV favors their antiparallel alignment. A value of $\Delta E \simeq -7$ meV is obtained within the LDA. These values are larger than the KKR result $\Delta E \simeq -3$ meV. However, the discrepancy is acceptable considering the differences expected from the narrow slab thickness (5-layers) used to model the surface and the possible interactions between the dimers and their images. Taking this into account, we expect that the present calculations provide a most valuable insight on the effects of structural relaxation on the value of ΔE at this very short distances. Indeed, the results show that the presence of a neighboring dimer does not affect the optimized bond length $d_b^{\text{GGA}} \simeq 2.76 \text{\AA}$. Furthermore, the structural relaxation modifies the exchange interaction only slightly ($\Delta E \simeq -13$ meV). In contrast to this last result, the LDA predicts a significant change of ΔE after structural relaxation. In fact, the antiparallel alignment favored for dimers at unrelaxed positions ($\Delta E \simeq -7$ meV) becomes unstable for an optimized structure ($\Delta E \simeq 2$ meV). The dimer bond length is, as in the case of an isolated dimer, shorter than the one predicted by the GGA. Another important difference concerns the optimal position of the Mn atoms with respect to the Cu surface, which is calculated to be about 0.1\AA shorter by the LDA

approximation. Additionally, the distance between the surface layers is also reduced. These two factors may contribute to the discrepancy between LDA and GGA results.

For a pair of AF dimers the differences in ΔE between the GGA and the LDA results are expected to be larger, since the dimer bond lengths predicted by these approximations differ to a large extent ($d_b^{GGA} \simeq 2.67 \text{ \AA}$ and $d_b^{LDA} \simeq 2.5 \text{ \AA}$). For an unrelaxed geometry, the calculated magnetic exchange $\Delta E \simeq 11 \text{ meV}$ predicts a parallel coupling between the two dimers, which is in agreement with the result obtained using the KKR method ($\Delta E \simeq 4 \text{ meV}$). This configuration is also found to be the ground-state of the ensemble. For the optimized structure $d_b \simeq 2.65 \text{ \AA}$ is slightly shorter than for isolated dimers. The magnetic exchange energy $\Delta E \simeq 9.3 \text{ meV}$ is very close to the the result found for unrelaxed structure.

From the later results, one concludes that structural optimizations within the dimer are important for the internal magnetic exchange energy E_X . In particular, the relaxed dimer bond length is shorter for an AF than for a FM alignment between Mn moments. As a consequence of this structural optimization the exchange energy $E_X = E_{FM} - E_{AF}$ is reduced. The AF configuration remains being the ground-state. Furthermore, structural relaxations have little effect on the magnetic coupling between a pair of dimers at second nearest neighbor positions. Thus, important modifications of the RKKY interaction at larger distances are not expected. Moreover, LDA and GGA approximations give quantitatively similar results of the magnetic exchange energies of systems having ideal structure. In this case, the results are comparable with those obtained by the KKR method. However, LDA predicts overall shorter interatomic distances which lead to meaningful differences in E_X and ΔE with respect to the GGA.

6.3 Conclusions

The magnetic exchange within and between Mn dimers on top of Cu(111) under the effect of an external electric field has been studied by a first-principles technique. The results show that EF can modify the exchange energy E_X within a single Mn_2 and eventually cause the reversal of the ground-state internal magnetic order from AF to FM state. Furthermore, the exchange interaction ΔE between pair of dimers shows RKKY-like oscillations as a function of r which differ from the single-atom behavior. In particular, the exchange magnetic coupling differs for pairs of dimers deposited

along the $[1\bar{1}0]$ and $[\bar{1}\bar{1}2]$ directions. This result implies a dependence of the exchange magnetic coupling on the position and orientation of the dimers on the surface.

Moreover, ΔE has been also found to depend on the magnetic order within the dimers. This behavior is a result of the difference in the scattering of majority-spin and minority-spin surface electrons which mediate the effective interaction between the clusters. Due to a higher delocalization of the dimer orbitals, the effect of an applied EF is in general stronger for FM than for AF dimers. EFs pointing out of the surface induce a decrease of spilled surface electronic density which favors a parallel alignment of the magnetic moments of the two Mn_2 . EFs pointing inwards favor their parallel alignment. However, an interplay between the magnetic exchange coupling and the effect of the external field is observed at short interdimer distances. In particular, an AF state within dimers at NN and second NN distances is preserved in the presence of outgoing EFs. This result suggests that for such distances the dimer-dimer interaction is stronger than the magnetic exchange coupling within the Mn_2 . Still, the substrate mediated magnetic exchange interaction is sensitive to the magnetic order within the clusters.

CHAPTER 7

Summary and outlook

The study of low-dimensional systems composed by magnetic atoms, nanoparticles and wires, and the research of methods to control their magnetic properties are of primary importance from a theoretical perspective, as well as for future technological applications. The fundamental understanding of magnetic interactions and their interplay with other properties is of particular relevance in this context. This work intends to address two particular problems concerning magnetic interactions between $3d$ -TM impurities and clusters in low-dimensional nonmagnetic hosts. For this purpose, *ab-initio* electronic calculations have been performed using two particularly suitable computational implementations of the DFT.

In the first part of this thesis, the problem of temperature induced superparamagnetic behavior is addressed from the perspective of an enhanced magnetic anisotropy energy of the particles. Chapter 4 studies the interrelation between magnetic coupling and magnetic anisotropy in $3d$ - $5d$ low-dimensional systems. In particular, the case of $3d$ -Pt nanowires is investigated focusing on the dependence of the magnetic order and MAE on the composition. Our results show a complex interrelation between composition, magnetic order and MAE. Oscillations of the MAE and easy-axis of magnetization are found by varying the $3d$ element. In addition, a switching of the relative alignment between the induced Pt moments and those of the $3d$ element is

observed. The behavior of the MAE is explained qualitatively in terms of the local SO couplings. It is shown that the largest MAEs are developed when the SO contributions of the Pt atoms and the $3d$ element have the same sign and favor a particular axis. The easy axis corresponds generally to the direction yielding the largest spin and orbital polarizations of the $5d$ -host. Furthermore, FePt_n wires have been analyzed in terms of the interplay between Fe concentration and magnetic order. A strong tendency to AF configurations is observed at all studied Fe concentrations (FePt_n with $n = 1 - 4$). Important spin and orbital moments are induced at the Pt sites showing relative alignments that change periodically as a function of their distance to the Fe atom. Such oscillations of the magnetic order result in corresponding changes of the total magnetization and MAE of the wires as a function of the composition. Finally, a violation of the 3rd Hund's rule at the Fe atomic sites is found for an in-line orientation of the magnetization, which suggests complex hybridization effects and a competition between inter-atomic and intra-atomic SO interactions.

The second part of this manuscript consists of two complementary studies on the effect of external electric fields on the magnetic exchange coupling between TM impurities and small clusters at Cu surfaces. The modification of the interactions as a result of the metallic screening and charge rearrangements have been determined self-consistently. In Chapter 5, the magnetic interactions between pairs of substitutional Co and Fe impurities at the Cu(111) surface have been determined in the presence of an external accumulation of electric charge above the surface as a function of the inter-impurity distance r . It is shown that the EF generated by an overlayer of charges at the surface modifies the local magnetic properties and interactions of the impurities in a significant way. These effects depend strongly on the polarity of the overlayer charge. Indeed, the repulsive potential resulting from an accumulation of negative charge causes a displacement of electronic density, which concerns mainly to minority-spin electrons at the impurity site. As a result of this rearrangement, the local magnetic moment of the impurities is modified. In particular, the reduction of minority-spin electronic charge leads to a monotonous enhancement of the local magnetic moment as the external charge per surface atom $|q|$ increases ($q < 0$). In contrast, the spill-off of the surface electronic density caused by an accumulation of positive charge screens to a large extent the external EF. In this case, the amount of electronic density at the topmost metal layer remains essentially independent of q ($q > 0$).

Our study also shows that surface charging affects the magnetic exchange energy ΔE between atomic impurities through three different microscopic mechanism: For

nearest-neighbor (NN) impurities, the charge-induced reduction of electronic density modifies the direct electronic hybridization, which determines the relative magnetic coupling. For impurities at second and third NN positions, the modification of this coupling is rather driven by the changes in the local electronic density at the Cu atoms located between them. At these short distances, large variations of ΔE , including switching between a FM and an AF alignment, can be induced by external surface charging. For larger inter-impurity distances, the changes in ΔE are caused by modifications of the delocalized electronic density of the Cu surface. The tuning of ΔE is achieved by the modification of the substrate-mediated RKKY-type exchange interaction, which controls the coupling between impurities.

The results obtained in Chapter 5 motivate the further study of the the effect of electric fields on the magnetic exchange within and between clusters at surfaces. The case of Mn dimers on top of a Cu(111) surface is addressed in Chapter 6. It is shown that the internal magnetic state of a Mn dimer can be controlled by means of an external EF. The exchange magnetic coupling ΔE between a pair of dimers shows RKKY-like oscillations as a function of the inter-particle distance r , which differ from the typical adatom-adatom behavior. A dependence of ΔE on the position and orientation of the dimers on the surface is observed from dimer pairs deposited along different orientations on the surface. Moreover, ΔE is found to depend sensitively on the magnetic order within the dimers. This is explained in terms of the difference in the scattering of majority-spin and minority-spin surface electrons, which mediate the effective interaction between the dimers. Furthermore, the EF-induced modifications of ΔE are different for inward and outward directions of the applied field with respect to the surface, particularly for pairs of FM dimers. Finally, a competition between the effect of the external EF and the magnetic exchange coupling within and between the dimers is observed at short interdimer distances.

In conclusion, the last two studies show that the use of applied EFs is an innovative and promising possibility for tuning the magnetic interactions within and between clusters on metal surfaces. The possibility of controlling the interactions among surface supported TM nanoparticles and their coupling with the environment would represent a significant progress in the design of nanostructured materials. Furthermore, new perspectives appear in the context of this approach for the external manipulation of other important properties. For instance, we have shown that EFs induce changes in the binding energies of the surface impurities. This result has appealing perspectives of application in the growth of surface nanostructures and in controlling self-assembly processes, surface growth and alloying. Another interesting

potential use of EFs is the tuning of the internal magnetic state on a variety of supported nanoparticles. The present study shows that EF-induced changes in the local electronic density can have a strong impact on the magnetic properties of nanostructures. Moreover, it is expected that external EFs will allow the manipulation of other electronic properties, which are strongly dependent on the electronic occupation at the Fermi level. In this context, the effect of EFs on the magnetic anisotropy energy is of considerable interest for future applications. Finally, it would be interesting to investigate magnetic clusters on highly polarizable substrates (e.g., Pd or Pt) where the magnetic interactions have a different nature, since the EF is expected to strongly affect the magnetic behavior of the substrate.

List of Figures

4.1	Calculated MAE $\Delta E = E_x - E_z$ of 3d-Pt wires at their equilibrium interatomic distance	46
4.2	Local density of d -states at the Fe and Pt sites of FePt and FePt ₂ wires	53
4.3	Local density of d -states at the Fe and Pt sites of a FePt ₃ wire	54
4.4	Illustration of the internal magnetic order and local spin moments in μ_B of ordered FePt ₁₆ , FePt ₁₄ and FePt ₁₂ wires	55
4.5	Local density of d -states at the Pt sites of an FePt ₁₆ wire	57
4.6	Illustration of the hcp and fcc adsorption sites of a Pt(111) surface . . .	64
5.1	Schematic diagram of substitutional impurities in a charged Cu(111) surface	73
5.2	Local density of s and p states at the topmost layer of the Cu(111) surface for increasing values of external charge	75
5.3	Calculated local magnetic moments at a single substitutional impurity as a function of overlayer charge q	76

5.4	Local density of d -states at a surface substitutional Co impurity in Cu(111)	77
5.5	Exchange interaction energy $\Delta E = E_{\text{FM}} - E_{\text{AF}}$ between two Co impurities at the Cu(111) surface as a function of the Co-Co distance r	79
5.6	Exchange interaction energy $\Delta E = E_{\text{FM}} - E_{\text{AF}}$ between two Fe impurities at the Cu(111) surface as a function of the Fe-Fe distance r	80
5.7	Exchange interaction energy $\Delta E = E_{\text{FM}} - E_{\text{AF}}$ of Co and Fe substitutional impurities at the Cu(111) surface as a function of the surface charge per atom q	82
5.8	Interaction energy E_{int} between Co NN impurities as a function of overlayer charge q	84
5.9	Local Co d -electron DOS of a FM dimer	85
5.10	Local s - and p -electron density of states at the Cu atom located between two Co impurities at third NN positions	87
6.1	Effective EF strength as a function of the generating point charges q	94
6.2	Illustration of the magnetic arrangements of a pair of dimers at the (111) fcc surface	95
6.3	Local electronic density of s - (p -) states at the topmost Cu(111) crystal layer and first vacuum layer above the surface	96
6.4	Exchange energy difference $E_{\text{x}} = E_{\text{FM}} - E_{\text{AF}}$ between the FM and AF state of a Mn dimer as a function of the EF source charge q	98
6.5	Exchange coupling energy $\Delta E = E_{\text{P}} - E_{\text{AP}}$ between two Mn dimers as a function of the interdimer distance r	100
6.6	Interparticle exchange coupling energy ΔE between two Mn dimers as a function of the EF source charge q	102
6.7	Interparticle exchange coupling energy $\Delta E = E_{\text{P}} - E_{\text{AP}}$ between two Mn dimers in the ground-state as a function of the interdimer distance r	103

-
- 6.8 Spin-polarized local density of states $\rho_\sigma(\varepsilon_F)$ at the Fermi energy ε_F in the vicinity of a FM Mn_2 and an AF Mn_2 on Cu(111) 104
- 6.9 Illustration of the unit supercell used to model a pair of Mn_2 on Cu(111) 106

List of Tables

4.I	Local spin and orbital moments in $3d$ -Pt wires at their equilibrium interatomic distances	47
4.II	Calculated total magnetic moment per atom and local spin moments in ordered FePt_n wires having a fixed interatomic distance of 2.4 \AA . . .	50
4.III	Calculated local spin and orbital moments and total magnetic moment per atom in ordered FePt_n wires having a fixed interatomic distance of 2.4 \AA	58
4.IV	Calculated local spin and orbital moments and total magnetic moment per atom in ordered FePt_n wires at the equilibrium interatomic positions	61
4.V	Magnetic moments and MAE of Co/Pt(111) for a surface coverage $1/8$	66
4.VI	Magnetic moments and MAE of Co/Pt(111) for a surface coverage $1/6$	66
4.VII	Magnetic moments and MAE of Co/Pt(111) for a surface coverage $1/4$	67
6.I	Calculated local magnetic moments μ_{Mn} , dimer bond length d_b , and magnetic exchange energies $E_X = E_{\text{FM}} - E_{\text{AF}}$ and $\Delta E = E_{\text{P}} - E_{\text{AP}}$. . .	107

Bibliography

- [1] E. Stoner, *Collective electron ferromagnetism*, Proc. R. Soc. A **165** 372 (1938).
- [2] G. M. Pastor, J. Dorantes-Dávila, and K. H. Bennemann, *Size and structural dependence of the magnetic properties of small 3d-transition-metal clusters*, Phys. Rev. B **40**, 7642 (1989).
- [3] J. Bansmann, S. H. Baker, C. Binns, J.A. Blackman, J.-P. Bucher, J. Dorantes-Dávila, V. Dupuis, L. Favre, D. Kechrakos, A. Kleibert, K.-H. Meiwes-Broer, G. M. Pastor, A. Perez, O. Toulemonde, K. N. Trohidou, J. Tuailleon, Y. Xie, *Magnetic and structural properties of isolated and assembled clusters*, Surface Science Reports **56**, 189 (2005).
- [4] N. Blanc, L. E. Díaz-Sánchez, A. Y. Ramos, F. Tournus, H. C. N. Tolentino, M. De Santis, O. Proux, A. Tamion, J. Tuailleon-Combes, L. Bardotti, O. Boisron, G. M. Pastor, and V. Dupuis, *Element-specific quantitative determination of the local atomic order in CoPt alloy nanoparticles: Experiment and theory*, Phys. Rev. B **87**, 155412 (2013).
- [5] L. E. Díaz-Sánchez, J. Dorantes-Dávila, and G. M. Pastor, *Local and chemical environment dependence of the magnetic properties of CoRh core-shell nanoparticles*, Phys. Rev. B **88**, 134423 (2013).

- [6] J. H. Morkkath and G. M. Pastor, *First-principles study of structural, magnetic, and electronic properties of small Fe-Rh alloy clusters*, Phys. Rev. B **85**, 054407 (2012).
- [7] P. Ruiz-Díaz, J. L. Ricardo-Chávez, J. Dorantes-Dávila, and G. M. Pastor, *Magnetism of small Cr clusters: Interplay between structure, magnetic order, and electron correlations*, Phys. Rev. B **81**, 224431 (2010).
- [8] C. Carbone, S. Gardonio, P. Moras, S. Lounis, M. Heide, G. Bihlmayer, N. Atodiresei, P. H. Dederichs, S. Blügel, S. Vlaic, A. Lehnert, S. Ouazi, S. Rusponi, H. Brune, J. Honolka, A. Enders, K. Kern, S. Stepanow, C. Krull, T. Balashov, A. Mugarza, and P. Gambardella *Self-Assembled Nanometer-Scale Magnetic Networks on Surfaces: Fundamental Interactions and Functional Properties*, Adv. Funct. Mater. **21**, 1212 (2011).
- [9] J. V. Barth, G. Costantini and K. Kern, *Engineering atomic and molecular nanostructures at surfaces*, Nature **437**, 671 (2005).
- [10] R. Otero, F. Rosei, and F. Besenbacher, *Scanning Tunneling Microscopy manipulation of complex organic molecules on solid surfaces*, Annual Review of Physical Chemistry **57**, 497 (2006).
- [11] D. Serrate, P. Ferriani, Y. Yoshida, Saw-Wai Hla, M. Menzel, K. von Bergmann, S. Heinze, A. Kubetzka and R. Wiesendanger, *Imaging and manipulating the spin direction of individual atoms*, Nature Nanotechnology **5**, 350 (2010).
- [12] M. Ternes, C. P. Lutz, C. F. Hirjibehedin, F. J. Giessibl, and A. J. Heinrich *The Force Needed to Move an Atom on a Surface*, Science **319**, 1066 (2008).
- [13] R. Wiesendanger, *Spin mapping at the nanoscale and atomic scale*, Rev. Mod. Phys. **81**, 1495 (2009).
- [14] L. Zhou, F. Meier, J. Wiebe, and R. Wiesendanger, *Inversion of spin polarization above individual magnetic adatoms*, Phys. Rev. B **82**, 012409 (2010).
- [15] Y. Yayon, V. W. Brar, L. Senapati, S. C. Erwin, and M. F. Crommie, *Observing Spin Polarization of Individual Magnetic Adatoms*, Phys. Rev. Lett. **99**, 067202 (2007).
- [16] A. Khajetoorians, J. Wiebe, B. Chilian, S. Lounis, S. Blügel, and R. Wiesendanger, *Atom-by-atom engineering and magnetometry of tailored nanomagnets*, Nature Physics **8** 497 (2012).

- [17] A. Khajetoorians, J. Wiebe, B. Chilian, and R. Wiesendanger, *Realizing All-Spin-ÅBased Logic Operations Atom by Atom*, *Science* **332**, 1062 (2011).
- [18] P. Gambardella, A. Dallmeyer, K. Maiti, M. C. Malagoli, W. Eberhardt, K. Kern, and C. Carbone, *Ferromagnetism in one-dimensional monatomic metal chains*, *Nature* **416**, 301 (2002).
- [19] P. Błoński, A. Lehnert, S. Dennler, S. Rusponi, M. Etzkorn, G. Moulas, P. Benckok, P. Gambardella, H. Brune, and J. Hafner, *Magnetocrystalline anisotropy energy of Co and Fe adatoms on the (111) surfaces of Pd and Rh*, *Phys. Rev. B* **81**, 104426 (2010).
- [20] P. Gambardella, S. Rasponi, M. Veronese, S.S. Deshi, C. Grazioli, A. Dallmeyer, I. Cabria, R. Zeller, P. H. Dederichs, K. Kern, C. Carbone, and H. Brune, *Giant Magnetic Anisotropy of Single Cobalt Atoms and Nanoparticles*, *Science* **300**, 1130 (2003).
- [21] P. Ruiz-Díaz, R. Garibay-Alonso, J. Dorantes-Dávila, and G. M. Pastor, *Non-collinear magnetism in transition metal nanostructures: Exchange interaction and local environment effects in free and deposited clusters*, *Phys. Rev. B* **84**, 024431 (2011).
- [22] S. Lounis, Ph. Mavropoulos, P. H. Dederichs, and S. Blügel, *Noncollinear Korringa-Kohn-Rostoker Green function method: Application to 3d nanostructures on Ni(001)*, *Phys. Rev. B* **72**, 224437 (2005).
- [23] N. N. Negulyaev, V. S. Stepanyuk, W. Hergert, and J. Kirchner, *Electric Field as a Switching Tool for Magnetic States in Atomic-Scale Nanostructures*, *Phys. Rev. Lett.* **106**, 037202 (2011).
- [24] A. Enders, R. Skomski, and J. Honolka, *Magnetic surface nanostructures*, *J. Phys.: Condens. Matter* **22**, 433001 (2010).
- [25] P. Wahl, P. Simon, L. Diekhöner, V. S. Stepanyuk, P. Bruno, M. A. Schneider, and K. Kern, *Exchange Interaction between Single Magnetic Adatoms*, *Phys. Rev. Lett.* **98**, 056601 (2007).
- [26] X. P. Zhang, B. F. Miao, L. Sun, C. L. Gao, A. Hu, H. F. Ding, and J. Kirschner, *Atomic superlattice formation mechanism revealed by scanning tunneling microscopy and kinetic Monte Carlo simulations*, *Phys. Rev. B.* **81**, 125438 (2010).

- [27] V. S. Stepanyuk, L. Niebergall, R. C. Longo, W. Hergert, and P. Bruno, *Magnetic nanostructures stabilized by surface-state electrons*, Phys. Rev. B **70**, 075414 (2004).
- [28] J. Hafner and D. Spišák, *Morphology and magnetism of Fe_n clusters (n=1-9) supported on a Pd(001) substrate*, Phys. Rev. B **76**, 094420 (2007).
- [29] M. A. Rudderman and C. Kittel, *Indirect Exchange Coupling of Nuclear Magnetic Moments by Conduction Electrons*, Phys. Rev. **96**, 99 (1954).
- [30] T. Kasuya, *A Theory of Metallic Ferro- and Antiferromagnetism on Zener's Model*, Prog. Theor. Phys. **16**, 45 (1956).
- [31] K. Yosida, *Magnetic Properties of Cu-Mn Alloys*, Phys. Rev. **106**, 893 (1957).
- [32] E. Simon, B. Újfalussy, B. Lazarovits, A. Szilva, L. Szunyogh, and G. M. Stocks, *Exchange interaction between magnetic adatoms on surfaces of noble metals*, Phys. Rev. B **83**, 224416 (2011).
- [33] V. S. Stepanyuk, A. N. Baranov, D. V. Tsvilin, W. Hergert, P. Bruno, N. Knorr, M. A. Schneider, and K. Kern, *Quantum interference and long-range adsorbate-adsorbate interactions*, Phys. Rev. B **68**, 205410 (2003).
- [34] N. Néel, R. Bernt, J. Kröger, T. O. Wehling, A. I. Lichtenstein, and M. I. Katsnelson, *Two-Site Kondo Effect in Atomic Chains*, Phys. Rev. Lett. **107**, 106804 (2011).
- [35] W. Shockley, *On the Surface States Associated with a Periodic Potential*, Physical Review, **56** 317 (1939).
- [36] M. F. Crommie, C. P. Lutz, and D. M. Eigler, *Imaging standing waves in a two-dimensional electron gas*, Nature **363** 524 (1993).
- [37] H. Bentmann, A. Buchter, and F. Reinert, *Interplay of electronic structure and atomic ordering on surfaces: Momentum-resolved measurements of Cs atoms adsorbed on a Ag(111) substrate*, Phys. Rev. B **85**, 121412 (2012)
- [38] R. Skomski, J. Zhang, V. Sessi, J. Honolka, K. Kern and A. Enders, *Substrate-controlled growth and magnetism of nanosize Fe clusters on Pt*, Journal of Applied Physics **103**, 07D519 (2008).
- [39] J. M. Rogowska, *Dilute nanostructures built of dimers: Kinetic Monte Carlo study of Co on Cu(111)*, Phys. Rev. B **82**, 035444 (2010).

- [40] J. Hu, B. Teng, F. Wu, and Y. Fang, *Fe nanostructures stabilized by long-range interactions on Cu(111): kinetic Monte Carlo simulations*, New Journal of Physics **10**, 023033 (2008).
- [41] M. N. Baibich, J. M. Broto, A. Fert, F. Nguyen Van Dau, F. Petroff, P. Etienne, G. Creuzet, A. Friederich, and J. Chazelas, *Giant Magnetoresistance of (001)Fe/(001)Cr Magnetic Superlattices*, Phys. Rev. Lett **61**, 2472 (1988); G. Binasch, P. Grünberg, F. Saurenbach, and W. Zinn, *Enhanced magnetoresistance in layered magnetic structures with antiferromagnetic interlayer exchange*, Phys. Rev. B **39**, 4828 (1989).
- [42] O. O. Brovko, P. A. Ignatiev, V. S. Stepanyuk, and P. Bruno, *Tailoring Exchange Interactions in Engineered Nanostructures: An Ab Initio Study*, Phys. Rev. Lett. **101**, 036809 (2008).
- [43] H. Oka, P. A. Ignatiev, S. Wedekind, G. Rodary, L. Bergall, V. S. Stepanyuk, D. Sander, and J. Kirschner, *Spin-Dependent Quantum Interference Within a Single Magnetic Nanostructure*, Science **12**, 843 (2010).
- [44] P. Hyldgaard and M. Persson, *Long-ranged adsorbate-adsorbate interactions mediated by a surface-state band*, J. Phys.: Condens. Matter **12**, L13 (2000).
- [45] P. A. Ignatiev, N. N. Negulyaev, L. Niebergall, H. Hashemi, W. Hegert, and V. S. Stepanyuk, *Electronic structure and magnetism of monatomic one-dimensional metal nanostructures on metal surfaces*, Phys. Status Solidi B **247**, 2537 (2010).
- [46] P. A. Ignatiev, N. N. Negulyaev, A. S. Smirnov, L. Niebergall, A. M. Saletsky, and V. S. Stepanyuk, *Magnetic ordering of nanocluster ensembles promoted by electronic substrate-mediated interaction: Ab initio and kinetic Monte Carlo studies*, Phys. Rev. B **80**, 165408 (2009).
- [47] L. Zohu, J. Wiebe, S. Lounis, E. Vedemenko, F. Meier, S. Blügel, P. H. Dederichs, and R. Wiesendanger, *Strength and directionality of surface Ruderman-Kittel-Kasuya-Yosida interaction mapped on the atomic scale*, Nature Physics **6**, 187 (2010).
- [48] F. Meier, L. Zhou, J. Wiebe, and R. Wiesendanger, *Revealing Magnetic Interactions from Single-Atom Magnetization Curves*, Science **320**, 82 (2008).
- [49] Z. Mao and X. Chen, *Magnetic phase diagram of interacting nanoparticle systems under the mean-field model*, J. Phys.: Condens. Matter **23**, 226005 (2011).

- [50] G. M. Pastor and P. J. Jensen, *Elementary transitions and magnetic correlations in two-dimensional disordered nanoparticle ensembles*, Phys. Rev. B **78**, 134419 (2008).
- [51] L. Néel, Ann. Geophys **5**, 99 (1949).
- [52] W. F. Brown, Phys. Rev **130**, 1677 (1963).
- [53] D. Weller, A. Moser, *Thermal effect limits in ultrahigh-density magnetic recording*, IEEE Transactions on Magnetics **35**, 4423 (1999).
- [54] G. Nicolas, J. Dorantes-Dávila, and G. M. Pastor, *Orbital polarization effects on the magnetic anisotropy and orbital magnetism of clusters, films, and surfaces: A comparative study within tight-binding theory*, Phys. Rev. B **74**, 014415 (2006).
- [55] M. Sargolzaei and S. S. Ataee, *First principles study on spin and orbital magnetism of 3d transition metal monatomic nanowires (Mn, Fe and Co)*, J. Phys. Condens. Matter **23**, 125301 (2011).
- [56] S. M. Valvidares, J. Dorantes-Dávila, H. Isern, S. Ferrer, and G. M. Pastor, *Interface-driven manipulation of the magnetic anisotropy of ultrathin Co films on Pt(111): Substrate deposition of hydrogen and model calculations*, Phys. Rev. B **81**, 024415 (2010).
- [57] N. N. Negulyaev, J. Dorantes-Dávila, L. Niebergall, L. Juárez-Reyes, G. M. Pastor, and V. S. Stepanyuk, *Alloying route to tailor giant magnetic anisotropy in transition-metal nanowires*, Phys. Rev. B **87**, 054425 (2013).
- [58] T. Burkert, O. Eriksson, S. I. Simak, A. V. Ruban, B. Sanyal, L. Nordström, and J. M. Wills, *Magnetic anisotropy of L10 FePt and Fe_{1-x}Mn_xPt*, Phys. Rev. B **71**, 134411 (2005).
- [59] V. S. Stepanyuk, W. Hergert, K. Wildberger, R. Zeller, P. H. Dederichs, *Magnetism of 3d, 4d, and 5d transition-metal impurities on Pd(001) and Pt(001) surfaces*, Phys. Rev. B **53**, 2121 (1996).
- [60] F. Meier, S. Lounis, J. Wiebe, L. Zhou, S. Heers, P. Mavropoulos, P. H. Dederichs, S. Blügel and R. Wiesendanger, *Spin polarization of platinum (111) induced by the proximity to cobalt nanostripes*, Phys. Rev. B **83**, 075407 (2011).
- [61] T. Balashov, T. Schuh, A. F. Takács, A. Ernst, S. Ostanin, J. Henk, I. Mertig, P. Bruno, T. Miyamachi, S. Suga, and W. Wulfhekel, *Magnetic Anisotropy and*

- Magnetization Dynamics of Individual Atoms and Clusters of Fe and Co on Pt(111)*, Phys. Rev. Lett **102**, 257203 (2009).
- [62] J. Honolka, T. Y. Lee, K. Kuhnke, D. Repetto, V. Sessi, P. Wahl, A. Buchsbaum, P. Varga, S. Gardonio, C. Carbone, S. R. Krishnakumar, P. Gambardella, M. Komelj, R. Singer, M. Fähnle, K. Fauth, G. Schütz, A. Enders, and K. Kern, *Complex magnetic phase in submonolayer Fe stripes on Pt(997)*, Phys. Rev. B **79**, 104430 (2009).
- [63] V. Dupuis, N. Blanc, L. E. Díaz-Sánchez, A. Hillion, A. Tamion, F. Tourmus, G. M. Pastor, *Specific local relaxation and magnetism in mass-selected CoPt nanoparticles*, Eur. Phys. J. B **86**, 83 (2013).
- [64] J. Dorantes-Dávila and G. M. Pastor, *Magnetic anisotropy of one-dimensional nanostructures of transition metals*, Phys. Rev. Lett. **81**, 208 (1998).
- [65] Y. Mokrousov, G. Bihlmayer, S. Blügel, and S. Heinze, *Magnetic order and exchange interactions in monoatomic 3d transition-metal chains*, Phys. Rev. B **75**, 104413 (2007).
- [66] M. M. Bezerra-Neto, M. S. Ribeiro, B. Sanyal, A. Bergman, R. B. Muniz, O. Eriksson, and A. Klautau, *Complex magnetic structure of clusters and chains of Ni and Fe on Pt(111)*, Scientific Reports **3**, 3054 (2013).
- [67] M. Saubanère, J. L. Ricardo-Chávez, and G. M. Pastor *Electronic and magnetic properties of Co and Ni impurities in Cu wires: First-principles investigation of local moment formation in one dimension*, Phys. Rev. B **82**, 054436 (2010).
- [68] M. Saubanère, M. Tanveer, P. Ruiz-Díaz and G. M. Pastor, *First principles theoretical study of complex magnetic order in transition-metal nanowires*, Phys. Status Solidi **247**, 2610 (2010).
- [69] M. Tanveer, P. Ruiz-Díaz, and G. M. Pastor, *Environment-dependent non-collinear magnetic orders and spin-wave spectra of Fe chains and stripes*, Phys. Rev. B **87**, 075426 (2013).
- [70] P. J. Feibelman, *Surface-diffusion mechanism versus electric field Pt/Pt(001)*, Phys. Rev. B **64** 125403 (2001).
- [71] S. Caravati and M. I. Trioni, *Structural and electronic properties of Na/Cu(111) at different coverages by first principles*, The European Physical Journal B **75**, 101 (2010).

- [72] Eberhard Engel and Reiner M. Dreizler, *Density Functional Theory: An advanced Course*, Springer Series in Theoretical and Mathematical Physics, Vol. 1 (Springer-Verlag Berlin Heidelberg 2011).
- [73] J. S. Slater, *A Simplification of the Hartree-Fock Method*, Phys. Rev. **81**, 385 (1951).
- [74] Richard M. Martin, *Electronic Structure: Basic Theory and Practical Methods*, Cambridge University Press, (New York, 2004).
- [75] R. M. Dreizler and E. K. U. Gross, *Density Functional Theory: An approach to the Quantum Many-Body Problem* (Springer-Verlag Berlin Heidelberg 1990).
- [76] P. Hohenberg and W. Kohn, *Inhomogeneous Electron Gas*, Phys. Rev. **136**, B864 (1964).
- [77] W. Kohn and L. J. Sham, *Self-Consistent Equations Including Exchange and Correlation Effects*, Phys. Rev. **140**, A1133 (1965).
- [78] W. Kohn, *v -Representability and Density Functional Theory*, Phys. Rev. Lett. **51**, 1596 (1983).
- [79] M. Levy, Phys. Rev. A **26**, 1200 (1982); M. Levy, Proc. Natl. Acad. Sci. **76**, 60 (1979); E. H. Lieb, Int. J. Quantum. Chem. **24**, 243 (1983).
- [80] T. L. Gilbert, *Hohenberg-Kohn theorem for nonlocal external potentials*, Phys. Rev. B **12**, 2111 (1975).
- [81] W. Kohn, A. D. Becke, and R. G. Parr, *Density Functional Theory of Electronic Structure*, J. Phys. Chem. **100** 12974 (1996).
- [82] J. P. Perdew and A. Zunger, *Self-interaction correction to density-functional approximations for many-electron systems*, Phys. Rev. B **23**, 5048 (1981).
- [83] Jan K. Labanowski, and Jan W. Andzelm *Density Functional Methods in Chemistry*, Springer-Verlag (New York, 1991).
- [84] S. Vosko, L. Wilk, and N. Nusair, Can. J. Phys. **58**, 1200 (1980).
- [85] J. P. Perdew, J. A. Chevary, S. H. Vosko, K. A. Jackson, M. R. Pederson, D. J. Singh, and C. Fiolhais, Phys. Rev. B **46**, 6671 (1992); J. P. Perdew, K. Burke, and Y. Wang, Phys. Rev. B. **54**, 16533 (1996).

- [86] P. W. Anderson, *Antiferromagnetism. Theory of Superexchange Interaction*, Physical Review **79**, 350 (1950).
- [87] P. W. Anderson, *New Approach to the Theory of Superexchange Interactions*, Physical Review **115**, 2 (1956).
- [88] G. Grosso and G. P. Parravicini, *Solid State Physics*, Elsevier Academic Press (London, 2004).
- [89] J. Kübler, K. H. Höck, J. Sticht and A. R. Williams, J. Phys. F: Met. Phys. **18** 469 (1988).
- [90] Paul Strange, *Relativistic Quantum Mechanics: With Applications in Condensed Matter and Atomic Physics*, Cambridge University Press, (1998).
- [91] R. P. Feynman, *Forces in Molecules*, Phys. Rev. **56**, 340 (1939).
- [92] G. Kresse and J. Furthmüller, *Efficient iterative schemes for ab initio total-energy calculations using a plane-wave basis set*, Phys. Rev. B **54** 11169 (1996); G. Kresse and J. Furthmüller, *Efficiency of ab-initio total energy calculations for metals and semiconductors using a plane-wave basis set*, Comput. Mat. Sci., **6** 15 (1996).
- [93] G. Kresse and J. Hafner, *Ab initio molecular dynamics for liquid metals*, Phys. Rev. B **47**, 558 (1993). G. Kresse and J. Hafner, *Ab initio molecular-dynamics simulation of the liquid-metal-amorphous-semiconductor transition in germanium*, Phys. Rev. B, **49**, 14251 (1994).
- [94] M. C. Payne, M. P. Teter and D. C. Allan, T. A. Arias and J. D. Joannopoulos, *Iterative minimization techniques for ab initio total-energy calculations: molecular dynamics and conjugate gradients*, Rev. Mod. Phys. **64**, 1045 (1992).
- [95] D. Hobbs, G. Kresse, and J. Hafner, *Fully unconstrained noncollinear magnetism within the projector augmented-wave method*, Phys. Rev. B **62**, 11556 (2001).
- [96] P. E. Blöchl, *Projector augmented-wave method*, Phys. Rev. B **50**, 17953 (1994).
- [97] G. Kresse and D. Joubert, *From ultrasoft pseudopotentials to the projector augmented-wave method*, Phys. Rev. **59**, 1758 (1999).
- [98] P. E. Blöchl, J. Kästner, and C. J. Först, *Electronic Structure Methods: Augmented Waves, Pseudopotentials and The Projector Augmented Wave Method*, Handbook of Materials Modeling (Springer Netherlands 2005).

- [99] J. Koringa, *Physica* **13**, 392 (1947); W. Kohn, and N. Rostoker, *Solution of the Schrödinger Equation in Periodic Lattices with an Application to Metallic Lithium*, *Phys. Rev.* **94**, 1111 (1954).
- [100] H. Ebert, D. Ködderitzsch, and J. Minár, *Calculating condensed matter properties using the KKR-Green's function method: recent developments and applications*, *Rep. Prog. Phys.* **74**, 096501 (2011).
- [101] J. Zabloudil, R. Hammerling, L. Szunyogh, and P. Weinberger, *Electron Scattering in Solid Matter: A Theoretical and Computational Treatise*, Springer Series in Solid-State Sciences, Vol. 147 (Springer-Verlag, Berlin, 2005).
- [102] H. Ebert, S. Bornemann, J. Braun, D. Ködderitzsch, S. Lowitzer, S. Mankovskyy, J. Minár, M. Offenberger, S. Polesya, and V. Popescu, *Recent Developments in KKR Theory*, *Psi-k Network Newsletter* **97**, 79 (2010).
- [103] R. Zeller, P. H. Dederichs, B. Újfalussy, L. Szunyogh, P. Weinberger, *Theory and convergence properties of the screened Korringa-Kohn-Rostoker method*, *Phys. Rev. B* **52**, 8807 (1995).
- [104] L. Szunyogh, B. Újfalussy, P. Weinberger, and J. Kollár, *Self-consistent localized KKR scheme for surfaces and interfaces*, *Phys. Rev. B* **49**, 2721 (1994).
- [105] N. Papanikolaou, R. Zeller, and P. H. Dederichs, *Conceptual improvements of the KKR method*, *J. Phys.: Condens. Matter* **14**, 2799 (2002).
- [106] P. Mavropoulos and N. Papanikolaou, *The Korringa-Kohn-Rostoker (KKR) Green Function Method I. Electronic Structure of Periodic Systems*, *Computational Nanoscience* **31**, 131 (2006).
- [107] P. H. Dederichs, S. Lounis, and R. Zeller, *The Korringa-Kohn-Rostoker (KKR) Green Function Method II. Impurities and Clusters in the Bulk and on Surfaces*, *Computational Nanoscience* **31**, 279 (2006).
- [108] P. Lloyd, *Wave propagation through an assembly of spheres: II. The density of single-particle eigenstates*, *Proc. Phys. Soc. Lond.* **90**, 207 (1967); P. Lloyd, and P. V. Smith, *Multiple scattering theory in condensed materials*, *Adv. Phys.* **21** 69 (1967); R. Zeller, *An elementary derivation of Lloyd's formula valid for full-potential multiple-scattering theory*, *J. Phys.: Condens. Matter* **16** 6453 (2004).

- [109] B. Lazarovits, L. Szunyogh, and P. Weinberger, *Magnetic properties of iron adatoms and small iron clusters on Ag(100)*, Journal of Magnetism and Magnetic Materials **240**, 331 (2002).
- [110] B. Lazarovits, L. Szunyogh, and P. Weinberger, *Fully relativistic calculation of magnetic properties of Fe, Co, and Ni adclusters on Ag(100)*, Phys. Rev. B **65** 104441 (2002).
- [111] B. Drittler, M. Weinert, R. Zeller, and P. H. Dederichs, *First-principles calculation of impurity-solution energies in Cu and Ni*, Phys. Rev. B **39**,930 (1989).
- [112] U. Klemradt, B. Drittler, R. Zeller, and P. H. Dederichs, *Interaction energies of impurities in Cu and Ni*, Phys. Rev. Lett. **64**, 2803 (1990).
- [113] J. J. Wang, T. Sakurai, K. Oikawa, K. Ishida, N. Kikuchi, S. Okamoto, H. Sato, T. Shimatsu, and O. Kitakami, *Magnetic anisotropy of epitaxially grown Co and its alloy thin films*, J. Phys.: Condens. Matter **21**, 185008 (2009).
- [114] M. Tsujikawa, A. Hosokawa and T. Oda, *Magnetic anisotropies of iron on the Pt(111) surface*, J. Phys.: Condens. Matter **19**, 365208 (2007).
- [115] F. Tournus, N. Blanc, A. Tamion, M. Hillenkamp, and V. Dupuis, *Dispersion of magnetic anisotropy in size-selected CoPt clusters*, Phys. Rev. B **81**, 220405 (2010).
- [116] G. Brown, B. Kraccek, A. Janotti, T. C. Schulthess, G. M. Stocks, and D. D. Johnson, *Competition between ferromagnetism and antiferromagnetism in FePt*, Phys. Rev. B **68**, 052405 (2003).
- [117] L. Gerhard, T. K. Yamada, T. Balashov, A. F. Takács, R. J. H. Wesselink, M. Däne, M. Fechner, S. Ostanin, A. Ernst, I. Mertig, and W. Wulfhekel, *Magneto-electric coupling at metal surfaces*, Nature Nanotechnology **5**, 792 (2010).
- [118] P. Gambardella, A. Dallmeyer, K. Maiti, M. C. Malagoli, W. Eberhardt, K. Kern and C. Carbone, *Ferromagnetism in one-dimensional monatomic metal chains*, Nature **416**, 301 (2002).
- [119] N. N. Negulyaev, V. S. Stepanyuk, L. Niebergall, P. Bruno, W. Hergert, J. Repp, K.-H. Rieder, and G. Meyer, *Direct evidence for the effect of quantum confinement of surface-state electrons on atomic diffusion*, Phys. Rev. Lett. **101**, 226601 (2008).

- [120] A. Smogunov, A. Dal Corso, A. Delin, R. Weht and, E. Tosatti, *Colossal magnetic anisotropy of monatomic free and deposited platinum nanowires*, Nature Nanotechnology **3**, 22 (2008).
- [121] J. Wang, C. Jo, and R. Wu, *Magnetic properties of Fe-5d (Os, Ir, and Pt) nanowires encapsulated in carbon nanotubes*, Appl. Phys. Lett. **92**, 032507 (2008).
- [122] F. Wilhelm, P. Pouloupoulos, H. Wende, A. Scherz, K. Baberschke, M. Angelakeris, N. K. Flevaris, and A. Rogalev, *Systematics of the induced magnetic moments in 5d Layers and the violation of the third Hund's rule*, Phys. Rev. Lett. **87**, (2001).
- [123] V. Kapaklis, P. T. Korelis, B. Hjörvarsson, A. Vlachos, I. Galanakis, P. Pouloupoulos, K. Özdoğan, M. Angelakeris, F. Wilhelm, and A. Rogalev, *Violation of Hund's third rule in structurally disordered ferromagnets*, Phys. Rev. B **84**, (2011).
- [124] F. Meier, K. von Bergmann, P. Ferriani, J. Wiebe, M. Bode, K. Hashimoto, S. Heinze, and R. Wiesendanger, *Spin-dependent electronic and magnetic properties of Co nanostructures on Pt(111) studied by spin-resolved scanning tunneling spectroscopy*, Phys. Rev. B **74**, 195411 (2006).
- [125] C. Etz, J. Zabloudil, P. Weinberger, and E. Y. Vedmedenko, *Magnetic properties of single atoms of Fe and Co on Ir(111) and Pt(111)*, Phys. Rev. B **77**, 184425 (2008).
- [126] J. Minár, S. Bornemann, O. Šipr, S. Polesya and H. Ebert, *Magnetic properties of Co clusters deposited on Pt(111)*, Appl. Phys. A **82**, 139 (2006).
- [127] J. Wiebe, F. Meier, K. Hashimoto, G. Bihlmayer, S. Blügel, P. Ferriani, S. Heinze and R. Wiesendanger, *Unoccupied surface state on Pt(111) revealed by scanning tunneling spectroscopy*, Phys. Rev. B **72**, 193406 (2005).
- [128] A. I. Liechtenstein, M. I. Katsnelson, V. P. Antropov and V. A. Gubanov, *Local Spin Density Functional approach to the theory of exchange interactions in ferromagnetic metals and alloys*, J. Mag. Magn. Mat. **67**, 65 (1987).
- [129] H. Ohno, *A window on the future of spintronics*, Nature Materials **9**, 952 (2010).
- [130] E. Y. Tsymbal, *Spintronics: Electric toggling of magnets*, Nature Materials **11**, 12 (2012).

- [131] D. Chiba, M. Sawiki, Y. Nishitani, Y. Nakatani, F. Matsukura, and H. Ohno, *Magnetization vector manipulation by electric fields*, Nature **455** 515 (2008).
- [132] S. J. Gamble, M. H. Burkhardt, A. Kashuba, R. Allenspach, S. S. P. Parkin, H. C. Siegmann, and J. Stöhr, *Electric Field Induced Magnetic Anisotropy in a Ferromagnet*, Phys. Rev. Lett. **102**, 217201 (2009).
- [133] H. Ohno, D. Chiba, F. Matsukura, T. Omlia, E. Abe, T. Dietl, T. Ohno, and K. Ohtanl, *Electric-field control of ferromagnetism*, Nature **408** 944 (2000).
- [134] S. Loth, S. Baumann, C. P. Lutz, D. M. Eigler, and A. J. Heinrich, *Bistability in Atomic-Scale Antiferromagnets*, Science **335**, 196 (2012).
- [135] T. Maruyama, Y. Shiota, T. Nozaki, K. Ohnta, N. Toda, M. Mizuguchi, A. A. Tulapurkar, T. Shinjo, M. Shiraishi, S. Mizukami, Y. Ando, and Y. Suzuki, *Large voltage-induced magnetic anisotropy change in a few atomic layers of iron*, Nature Nanotechnology **4**, 158 (2009).
- [136] M. Weisheit, S. Fähler, A. Marty, Y. Souche, C. Poinsignon, and D. Givord, *Electric Field-Induced Modification of Magnetism in Thin-Film Ferromagnets*, Science **315**, 349 (2007).
- [137] K. Shimamura, D. Chiba, S. Ono, S. Fukami, N. Ishiwata, M. Kawaguchi, K. Kobayashi, and T. Ono, *Electrical control of Curie temperature in cobalt using an ionic liquid film*, Appl. Phys. Lett. **100**, 122402 (2012).
- [138] P. A. Ignatiev and V. S. Stepanyuk, *Effect of the external electric field on surface states: An ab initio study*, Phys. Rev. B **84**, 075421 (2011).
- [139] K. Berland, T. L. Einstein, and P. Hyldgaard, *Response of the Shockley surface state to an external electrical field: A density-functional theory study of Cu(111)*, Phys. Rev. B **85**, 035427 (2012).
- [140] P. A. Ignatiev, O. O. Brovko, and V. S. Stepanyuk, *Local tunneling magnetoresistance control with surface-state confinement and external electric field*, Phys. Rev. B **86**, 045409 (2012).
- [141] S. Zahng, *Spin-Dependent Surface Screening in Ferromagnets and Magnetic Tunnel Junctions*, Phys. Rev. Lett. **83**, 640 (1999).

- [142] K. Nakamura, R. Shimabukuro, Y. Fujiwara, T. Akiyama, T. Ito, and A. J. Freeman, *Giant Modification of the Magnetocrystalline Anisotropy in Transition-Metal Monolayers by an External Electric Field*, Phys. Rev. Lett. **102**, 187201 (2009).
- [143] C. Duan, J. P. Velev, R. F. Sabirianov, Z. Zhu, J. Chu, S. S. Jaswal, and E. .Y Tsymlal, *Surface Magnetoelectric Effect in Ferromagnetic Metal Films*, Phys. Rev. Lett. **101**, 137201 (2008).
- [144] M. Tsujikawa and T. Oda, *Finite Electric Field Effects in the Large Perpendicular Magnetic Anisotropy Surface Pt/Fe/Pt(001): A First-Principles Study*, Phys. Rev. Lett. **102**, 247203 (2009).
- [145] P. Ruiz-Díaz, T. R. Dasa, and V. S. Stepanyuk, *Tuning Magnetic Anisotropy in Metallic Multilayers by Surface Charging: An Ab-Initio Study*, Phys. Rev. Lett. **110**, 267203 (2013).
- [146] L. Juárez-Reyes, G. M. Pastor, and V. S. Stepanyuk, *Tuning substrate-mediated magnetic interactions by external surface charging: Co and Fe impurities on Cu(111)*, Phys. Rev. B **86**, 235436 (2012).
- [147] S. L. Gong, C. Duan, Z. Zhu, and J. Chu, *Manipulation of magnetic anisotropy of Fe/graphene by charge injection*, Appl. Phys. Lett. **100** 122410 (2012).
- [148] J. Hu and R. Wu, *Control of the Magnetism and Magnetic Anisotropy of a Single-Molecule Magnet with an Electric Field*, Phys. Rev. Lett. **110**, 097202 (2013).
- [149] Yun-Hao Lu, Lei Shi, Chun Zhang, and Yuan-Ping Feng, *Electric-field control of magnetic states, charge transfer, and patterning of adatoms on graphene: First-principles density functional theory calculations*, Phys. Rev. B **80**, 233410 (2009).
- [150] B. Yoon and U. Landman, *Electric Field Control of Structure, Dimensionality, and Reactivity of Gold Nanoclusters on Metal-Supported MgO Films*, Phys. Rev. Lett. **100**, 056102 (2008).
- [151] M. Fechner, P. Zahn, S. Ostanin, M. Bibes, and I. Mertig, *Switching Magnetization by 180 with an Electric Field*, Phys. Rev. Lett. **108** 197206 (2012).
- [152] O. O. Brovko, V. S. Stepanyuk, and P. Bruno, *Effect of exchange interaction on the spin-polarized bound states on metal surfaces: Ab initio study*, Phys. Rev. B **78**, 165413 (2008).

- [153] O. O. Brovko and V. S. Stepanyuk, *Probing the magnetism of nanostructures buried in metallic surfaces and their possible utilization*, Phys. Status Solidi B **247**, 1161 (2010).
- [154] E. Simon, B. Ujfalussy, A. Szilva, and L. Szunyogh, *Anisotropy of exchange interactions between impurities on Cu(110) surface*, J. Phys.: Conf. Ser. **200** 032067 (2010).
- [155] P. N. Patrone, and T. L. Einstein, *Anisotropic surface-state-mediated RKKY interaction between adatoms*, Phys. Rev. B **85**, 045429 (2012).
- [156] N. Knorr, H. Brune, M. Epple, A. Hirstein, M. A. Schneider, and K. Kern, *Long-range adsorbate interactions mediated by a two-dimensional electron gas*, Phys. Rev. B **65** 115420 (2002).
- [157] V. S. Stepanyuk, L. Niebergall, A. N. Baranov, W. Hegert, and P. Bruno, *Long-range electronic interactions between adatoms on transition metal surfaces*, Comp. Mat. Sci. **35**, 272 (2006).
- [158] S. Schnur and A. Gross, *Challenges in the first-principles description of reactions in electrocatalysis*, Catalysis Today **165**, 129 (2011).
- [159] K. P. Bohnen and D. M. Kolb, *Charge- versus adsorbate-induced lifting of the Au(100)-(hex) reconstruction in an electrochemical environment*, Surf. Sci. **407**, L629 (1998).
- [160] Y. J. Feng, K. P. Bohnen, and C. T. Chan, *First-principles studies of Au(100)-hex reconstruction in an electrochemical environment*, Phys. Rev. B **72**, 125401 (2005).
- [161] C. L. Fu and K. M. Ho, *External-charge-induced surface reconstruction on Ag(110)*, Phys. Rev. Lett. **63**, 1617 (1989).
- [162] A. Y. Lozovoi and A. Alavi, *Reconstruction of charged surfaces: General trends and a case study of Pt(110) and Au(110)*, Phys. Rev. B **68**, 245416 (2003).
- [163] O. O. Brovko, P. Ruiz-Díaz, T. R. Dasa, and V. S. Stepanyuk, *Controlling magnetism on metal surfaces with non-magnetic means: electric fields and surface charging*, J. Phys.: Condens. Matter **26**, 093001 (2014).

- [164] P. Wahl, A. P. Seitsonen, L. Diekhöner, M. A. Schneider, and K. Kern, *Kondo-effect of substitutional cobalt impurities at copper surfaces*, New. J. Phys. **11**, 113015 (2009).
- [165] K. Wildberger, V. S. Stepanyuk, P. Lang, R. Zeller, and P. H. Dederichs, *Magnetic Nanostructures: 4 d Clusters on Ag(001)*, Phys. Rev. Lett. **75**, 509 (1995).
- [166] S. Alexander and P. W. Anderson, *Interaction Between Localized States in Metals*, Phys. Rev. **133**, A1594 (1964).
- [167] N. Baadji, M. Piacenza, T. Tugusuz, F. Della Sala, G. Maruccio, and S. Sanvito, *Electrostatic spin crossover effect in polar magnetic molecules*, Nature Materials **8**, 813 (2009).
- [168] C. F. Hirjibehedin, C. P. Lutz, and A. J. Heinrich, *Spin Coupling in Engineered Atomic Structures*, Science **312**, 1021 (2006).
- [169] M. C. Tropicovsky, K. Zhao, D. Xiao, Z. Zhang, and A. G. Eguiluz, *Tuning the Electronic Coupling and Magnetic Moment of a Metal Nanoparticle Dimer in the Nonlinear Dielectric-Response Regime*, Nano Lett., **9**, 4452 (2009).
- [170] V. S. Stepanyuk, A. N. Baranov, W. Hergert, and P. Bruno, *Ab initio study of interaction between magnetic adatoms on metal surfaces*, Phys. Rev. B **68**, 205422 (2003).
- [171] F. Muñoz, A. H. Romero, J. Mejía-López, and J. L. Morán-López, *First-principles theoretical investigation of monoatomic and dimer Mn adsorption on noble metal (111) surfaces*, Phys. Rev. B **85**, 115417 (2012).
- [172] J. Friedel, *Metallic alloys*, Nuovo Cimento, Suppl. **7**, 287 (1958).
- [173] N. D. Lang and W. Kohn, *Theory of Metal Surfaces: Charge Density and Surface Energy*, Phys. Rev. B **1**, 4555 (1970).
- [174] K. H. Lau and W. Kohn, *Indirect long-range oscillatory interaction between adsorbed atoms*, Surf. Sci. **75**, 69 (1978).
- [175] T. L. Einstein and J. R. Schrieffer, *Indirect Interaction between Adatoms on a Tight-Binding Solid*, Phys. Rev. B **7**, 3629 (1973).
- [176] Chiung-Yuan Lin, Jheng-Lian Li, Yao-Hsien Hsieh, Keng-Liang Ou, and B. A. Jones, *Magnetic Interaction between Surface-Engineered Rare-Earth Atomic Spins*, Phys. Rev. X **2**, 021012 (2012).

- [177] S. K. Nayak and P. Jena, *Anomalous magnetism in small Mn clusters*, Chem. Phys. Lett. **289**, 473 (1998).
- [178] M. R. Pederson, F. Reuse, and S. N. Khanna, *Magnetic transition in Mn_n ($n=2-8$) clusters*, Phys. Rev. B. **58**, 5632 (1998).
- [179] V. A. Rigo, R. H. Miwa, A. J. R. da Silva, and A. Fazzio, *Mn dimers on graphene nanoribbons: An ab initio study*, J. Appl. Phys. **109**, 053715 (2011).
- [180] B. Wang and Z. Chen, *Magnetic coupling interaction under different spin multiplets in neutral manganese dimer: CASPT2 theoretical investigation*, Chem. Phys. Lett. **387**, 395 (2004).
- [181] L. Juárez-Reyes, V. S. Stepanyuk and G. M. Pastor, *Electric-field-modulated exchange coupling within and between magnetic clusters on metal surfaces: Mn dimers on Cu(111)*, J. Phys.: Condens. Matter **26**, 176003 (2014).
- [182] N. N. Negulyaev, V. S. Stepanyuk, L. Niebergall, P. Bruno, W. Auwärter, Y. Pennec, G. Jahnz, and J. V. Barth, *Effect of strain relaxations on heteroepitaxial metal-on-metal island nucleation and superlattice formation: Fe on Cu(111)*, Phys. Rev. B **79**, 195411 (2009).
- [183] R. Brako and D. Šokčević, *Adsorbate-induced substrate relaxation and the adsorbate-adsorbate interaction*, Surface Science **469**, 185 (2000).
- [184] H. Zhang, M. Richter, K. Koepf, I. Opahle, F. Tasnádi, and H. Eschring, *Electric-field control of surface magnetic anisotropy: a density functional approach*, New. J. Phys. **11**, 043007 (2009).